

Copyright  
by  
John Kuck David  
2011

**The Dissertation Committee for John Kuck David Certifies that this is the approved  
version of the following dissertation:**

**Semiclassical and Path-Sum Monte Carlo Analysis  
of Electron Device Physics**

**Committee:**

---

Sanjay K. Banerjee, Supervisor

---

Leonard F. Register, Co-Supervisor

---

Seth Bank

---

Graeme Henkelman

---

Emanuel Tutuc

**Semiclassical and Path-Sum Monte Carlo Analysis  
of Electron Device Physics**

**by**

**John Kuck David, BSEE, MS**

**DISSERTATION**

Presented to the Faculty of the Graduate School of

The University of Texas at Austin

in Partial Fulfillment

of the Requirements

for the Degree of

**DOCTOR OF PHILOSOPHY**

**The University of Texas at Austin**

**December 2011**

## **Dedication**

Dedicated to my family.

## Acknowledgements

The first persons I would like to thank are my advisors, Prof. Sanjay Banerjee and Prof. Frank Register. Their world-class research, physical insight, and attention to detail has inspired and guided me throughout my academic career at The University of Texas at Austin. They have offered me their unwavering support, encouragement and freedom to direct my own research interests for which I am eternally grateful. I have enjoyed working with both of them and will look on my time at The University of Texas at Austin with fondness. I am confident that my new-found work ethic and research method I have gained under their tutelage will stay with me throughout my career.

I would like to thank my committee members, Prof. Seth Bank, Prof. Graeme Henkelman, and Prof. Emanuel Tutuc for their support and knowledge base that has helped me continue and refine my research program. In addition, I wish to thank our former post-doc Prof. Matthew Gilbert, who first recruited me to the University of Texas. With his initial guidance in investigating Path Integral Monte Carlo methods, I gained the inspiration to develop my own algorithm.

I also wish to thank each of the group members, past and present, for their help in my PhD studies. Their ability to ask and answer questions helped me to think more critically about my research. I wish to thank the administration and staff of the Electrical Engineering department and Graduate School for their assistance. A special thank you to Jean Toll, whose smiling face, open ear, and capable skills have been a persistent path maker for myself and others.

Finally, I wish to thank my entire family for giving me the needed encouragement, guidance, and opportunity throughout my academic career. I wish to

thank especially my wife Julianne; without her love, support and encouragement I would not be where I am today.

John K. David

*The University of Texas at Austin*

*July 2011*

# **Semiclassical and Path-Sum Monte Carlo Analysis of Electron Device Physics**

John Kuck David, PhD

The University of Texas at Austin, 2011

Supervisors: Sanjay K. Banerjee and Leonard F. Register

The physics of electron devices is investigated within the framework of Semiclassical Monte Carlo and Path-Sum Monte Carlo analysis. Analyses of short-channel III-V trigate nanowire and planar graphene FETs using a Semiclassical Monte Carlo algorithm are provided. In the case of the nanowire FETs, the bandstructure and scattering effects of a survey of materials on the drain current and carrier concentration are investigated in comparison with Si FETs of the same geometry. It is shown that for short channels, the drain current is predominantly determined by associated change in carrier velocity, as opposed to changes in the carrier concentration within the channel. For the graphene FETs, we demonstrate the effects of Zener tunneling and remote charged impurities on the device performance. It is shown that, commensurate with experimental evidence, the devices have great difficulty turning off as a result of the Zener tunneling, and have a conductivity minimum which is affected by remote impurities inducing charge puddling. Each material modeled is matched with experimental data by calibrating the scattering rates with velocity-field curves. Material and geometry specific parameters, models, and methods are described, while discussion of the basic semiclassical Monte Carlo method is left to the extensive volume of publications on the subject. Finally, a novel quantum Path-Sum Monte Carlo algorithm

is described and applied to a test case of two layered 6 atom rings (to mimic graphene), to demonstrate the effectiveness of the algorithm in reproducing phase transitions in collective phenomena critical to possible beyond-CMOS devices. First, the method and its implementation are detailed showing its advantages over conventional Path Integral Monte Carlo and other Quantum Monte Carlo approaches. An exact solution of the system within the framework of the algorithm is provided. A Fixed Node derivative of the Path Sum Monte Carlo method is described as a work-around of the infamous Fermion sign problem. Finally, the Fixed Node Path-Sum Monte Carlo algorithm is implemented to a set of points showing the accuracy of the method and the ability to give upper and lower bounds to the phase transition points.

## Table of Contents

List of Tables .....	xi
List of Figures .....	xii
Chapter 1. Introduction .....	1
Chapter 2. 3D-Monte Carlo Study of Short Channel Trigate Nanowire MOSFETs	5
Introduction .....	5
Simulation Methodology .....	7
Results and Analysis .....	13
Conclusion .....	20
Chapter 3. Semi-Classical Monte Carlo Analysis of Graphene FETs .....	21
Introduction .....	21
Model Calibration and “Bulk” Transport .....	23
Band-structure .....	23
Scattering Mechanisms .....	24
E-v Matching .....	26
Zener Tunneling .....	30
Device Simulation .....	32
Device Geometry .....	32
Band-to-Band Tunneling and Lack of Saturation .....	33
Transport and Remote Impurities .....	35
Conclusion .....	39
Chapter 4. A Path-Sum Monte Carlo Approach for Many-Electron Systems Within a Tight-Binding Basis .....	40
Introduction .....	40
Path Sum Monte Carlo .....	41
General formulation .....	41
Fixed node approximation(s) .....	46
Trial System and Exact Behavior .....	48

Comparison of exact and FN-PSMC results .....	59
Conclusion .....	62
Chapter 5. Conclusion.....	63
Comments .....	63
Future Research .....	65
SCMC Improvements .....	65
PSMC Improvements.....	67
Appendices.....	71
Appendix A: Fixed Node Path Sum Monte Carlo Algorithm .....	71
Program Flow .....	71
Initiating the Effective Hamiltonian and the Density Matrix .....	72
Initiating and Choosing a New Path .....	77
Measure Observable .....	80
Appendix B: Sample Path Sum Monte Carlo MATLAB Script I .....	82
Appendix C: Sample Path Sum Monte Carlo MATLAB Script II .....	87
References.....	93
Vita	97

## List of Tables

Table 1:	Physical parameters used in simulation of materials. $E_g$ : bandgap. $m^*/m_0$ : effective mass ratio. $\epsilon_r$ : relative permittivity. $\epsilon_\infty$ : relative permittivity high frequency. $E_{\text{valley}}-E_c$ : valley offset. $a$ : lattice spacing. $\alpha$ : nonparabolicity factor. $\rho$ : atomic density. $v_s$ : sound velocity .....9
Table 2:	Scattering parameters for the materials. In all materials, acoustic scattering was included. In Si, f and g type intervalley scattering are also included. For the III-V materials, inter/intravalley scattering was taken into account, using the standard deformation potential field used in the references along with polar optical phonon scattering. Because the X valley in InSb is so far above the conduction band minimum, it was ignored in these calculations.....10
Table 3:	Exact and FN-PSMC calculation of the average energy of the system, with the exact evaluations of the FN approximations shown for reference in parentheses.....61
Table 4:	Exact and FN-PSMC calculation of expected interlayer matrix elements, with the exact evaluations of the FN approximations shown for reference in parentheses.....61

## List of Figures

- Figure 1: Scatter of conduction band effective density of states and electron mobilities for different semiconductors. From the plot it can be seen that there is a trade-off between the density-of-states and the mobility of the electron in materials, suggesting that there could be an optimal channel material choice for MOS devices.....6
- Figure 2: Schematic of nanowire MOSFET geometry with side, top, and cross-sectional view of the device. The channel length of all devices was kept constant at 10 nm with a source and drain contact length of 10 nm. The wire was a 3x3 nm square cross section with a 1 nm thick oxide barrier wrapped around three facets of the channel region. The base of the device was assumed to have a constant zero field in terms of the boundary condition. ....8
- Figure 3: Calculated average velocity vs. electric field curves for the five materials surveyed using the material parameters quoted in Tables 1 and 2. ..12
- Figure 4:  $I_{ds}$ - $V_G$  curve at  $V_d=0.8V$  for Si, InP, GaAs, InAs, and InSb Tri-gate nanowire transistors. Curves were obtained from a 3D Semiclassical Monte Carlo Simulator with scattering and with a Schrödinger-type correction to the electrostatic potential to account for quantum confinement effects. The results exhibit a grouping according to effective mass, with InAs and InSb performing the best, followed by InP and GaAs, and finally Si. ....13

Figure 5:  $I_{ds}$ - $V_{ds}$  curves for each material with the Schrodinger correction and scattering turned on in the simulator. The gate bias was set to 0.25 V above threshold. Although noisy, the purpose of these plots is only to illustrate device saturation at the 0.8V drain-to-source bias used in each of the materials.....14

Figure 6:  $I_{ds}$ - $V_G$  curves for the five materials without considering scattering. As compared to the results of Figure 3, there is limited increase in the currents in the III-V devices, but about a 20% boost in the current in Si FETs. As scattering plays little role in the III-V materials in these simulations, the differences in currents among the III-V materials appears to be due primarily to only band structure differences among the materials. However, scattering, or rather the lack of significant scattering in III-V materials, does further distinguish the III-V MOSFET performance from that of Si MOSFETs. ....15

Figure 7: Time-averaged integrated channel carrier concentration of materials calculated over the volume of the channel region. The capacitances of the devices are nearly identical suggesting that the current is determined by the average velocities of the carriers.....16

Figure 8: Time-averaged integrated channel carrier concentrations calculated over the volume of the channel without any quantum. The charge densities are nearly identical for each of the materials, suggesting that that oxide capacitance in this tri-gate structure, by comparison to Figure 7, dominate both the capacitances related to quantum confinement and the density-of-states. ....17

Figure 9:  $I_d$ - $V_g$  curves for FETs without any quantum correction. The currents are higher for all materials as a result of the higher carrier concentrations, as shown in Figure 8. ....18

Figure 10:  $I_d$ - $V_g$  curves for devices with effective potential correction, instead of the Schrödinger-based correction used for the other calculations in this paper. Current is overestimated due to artificial reductions in the channel potential resulting from leakage of the "wave-packet" through the oxide and into the gates. The wavepacket breadths were as follows [nm]: Si: 0.87, InP: 1.73, GaAs: 1.91, InAs: 3.34, InSb: 4.19.....19

Figure 11. Velocity Field curve for graphene in vacuum matching mobility and saturation values published in literature. In comparison with Fig. 2 the low-field mobility is much higher as a result of the absence of any impurity scattering and is dominated by acoustic phonon scattering at low fields.....27

Fig. 12. Velocity field curve for graphene on SiO<sub>2</sub> bottom and HfO<sub>2</sub> bottom matching published data for the mobility and saturation velocity. The drift velocity at low fields is dominated by scattering from remote impurities in the silicon and saturates at very high fields from optical phonons.....28

Fig. 13. Percent scattering events as function of field. At low fields acoustic scattering mechanisms dominate followed by optical phonon scattering at higher fields causing the velocity to saturate.....29

Figure 14. Percent scattering events as function of field on SiO<sub>2</sub> bottom and HfO<sub>2</sub> top. Remote impurity and remote optical phonon scattering are majority processes suppressing the low-field mobility and drift velocity.....30

- Figure 15. Comparison of currents from devices with and without the Klein tunneling. As seen, the effect of Klein tunneling on the current is very strong and causes the device to have difficulty saturating even at very high drain biases. Without the tunneling, the device acts like a conventional MOSFET. The top gate bias was set to 100 mV and the bottom gate was grounded. ....34
- Figure 16. Drain current from device with oxide impurity concentration of  $5 \times 10^{11}/\text{cm}^2$  at fixed drain voltage of  $-50\text{mV}$ . Plot shows expected qualitative behavior as the Fermi level passes through the Dirac point, broadening both by temperature and perhaps charge puddling. ....35
- Figure 17. Comparison of currents for fixed drain bias with phonon scattering and impurities (squares), phonon scattering only (diamonds) and impurities only (circles). There is clearly an increase in the current with phonon scattering turned off, but less change with impurities removed from the oxide layers. However, using a parabolic fit to the minimum of the curves shows a small shift in the position of the minimum current and a slight broadening of the I-V characteristic as a result of the impurity-altered electrostatics.....36
- Figure. 18: Comparison of currents for fixed drain bias with high and low impurity concentrations in the oxide layers above and below the graphene layer. There is a clear shift in the current minimum voltage and broadening as a result of impurity-adjusted electrostatics. In addition, there is an increase in the current minimum as a result of impurity-induced fluctuations in the potential profile in the channel and associated charge puddling. ....37

- Figure 19: (a) Time averaged 1D plots of the electron concentration on top and the potential profile on bottom. There is a clear peak in the concentration above a trough in the potential where impurities are placed. The dark vertical line show the alignment of electron concentration peak and that the peak and potential trough. (b) Fixed impurity placement within the oxides along the channel. The dark horizontal line indicates the graphene layer. The dots scattered on either side are the fixed charged impurities in the oxide layers. In the same region around the peak in concentration in (a) there are several impurities within a nanometer of the graphene layer. Note that the impurity locations vary in three dimensions, while only two are shown here. ....38
- Figure 20: The trial system used for this study is comprised of two 6 atom single orbital rings layered with direct stacking of the atoms on opposite rings. The differing colors are used to enhance which is the top and which is bottom layer. ....48
- Figure 21: Expected total energy for two 6 (carbon) atom rings separated by distance  $d$  at a temperature,  $T$ . The drop in energy at high temperatures from large to small interlayer separation corresponds to the formation of excitons. At lower temperatures the excitons are formed at even great separation distances, though not necessarily correlated. ....51
- Figure 22: Top-down view of the total energy of system. The black solid line maps the maximum of the average energy noting a transition where excitons begin to form. Noted in the plot are points A', B' and C' noting the positions where the density-density correlation function was measured. ....52

- Figure 23: Density-density correlation function of electrons in same and opposite layers of the bilayer system. At high temperature large separation Point B' (middle) there is little correlation in electron positions among the sites within the same layer and limited correlation between layers. But as the separation between layers is decreased to Point A' (left), the (anti-) correlation between electron position between layers increases substantially, indicating the formation of an exciton. At point C' with the same interlayer separation as in A' but lower temperature, still stronger interlayer correlation and now strong intralayer correlation is observed. ....53
- Figure 24: Magnitude of the energy difference between the semi-isolated system and the exact system at a range of interlayer distances and temperatures. The sharp increase in difference between the expected energies is a representation of the effect of interlayer exchange-correlation energies within the system. ....54
- Figure 25: Average interlayer hopping energy matrix element difference between systems with and without interlayer Coulomb interactions. At higher temperatures or large distances, the interlayer coherence of the wavefunctions is reduced and interlayer Coulomb interactions have little effect on the interlayer hopping potential matrix elements. However, at optimally intermediate temperatures and small interlayer distance, there is a substantial growth in the interlayer hopping potential matrix element. These results provides a measure of the coherence between the layers and evidence for a condensate in this trial system. ....56

- Figure 26: Average hopping energy matrix element between top and bottom layers for the system with 4 electrons. With 4 electrons populating the two rings, the Fermi energy is set between the symmetric and anti-symmetric states that result from interlayer coupling of otherwise degenerate states. This produces an overall enhanced exchange interaction by comparison to the results of Figure 6, and one peaking at zero temperature. ....57
- Figure 27: Error in average energy for both fixed node approximations at various temperatures. Open symbols represent the ceiling fixed node and the filled symbols the floor fixed node. The type of shape represents the temperature. The floor fixed node shows an energy minimum, whereas the ceiling represents a maximum to the average energy of the system. ....58
- Figure 28: Density density correlation functions for point A' in the interlayer distance-temperature phase space comparing the PSMC implementations of the two FN approximations, FNC and FNF with the exact calculation. Both fixed node approximations provide reasonable accuracy for estimating the correlation between the layers.....60
- Figure 29: In the Poisson solver, the contact is copied onto many grid points which are connected to grid points in the device as in the left. However, as the potential on these points is constant and never changes, the contact may be condensed into a single node, as on the right, from which the relevant points may be connected.....66
- Figure 30: The canonical partition function used in the construction of the Path Sum in Chapter 4, can be pictured as a system S1 weakly coupled to a heat bath S2 with a constant number of particles in the system. ....69

Figure 31: The grand canonical partition function can be pictured as a system S1 weakly coupled to a heat bath S2 and allowing particle exchange between the reservoirs. ....69

Figure 32: For a Quantum Point Contact QPC, two contact regions S1 and S2 are weakly connected to each other and also to two heat bath reservoirs H1 and H2 with different chemical potentials. In this way, transport measurements may be performed. ....70

Figure 33: General flow of PSMC algorithm. The “Choose New Path” and “Measure Observable” steps are repeated ‘N’ times or until convergence of observable is reached.....71

Figure 34: Graphs for populating a 4-site model with a: 1 electron and b: 2 electrons. The nodes on the graphs are indexed by the integer value of the binary translation of the Fock state. i.e. 1=0001, 2=0010, 3=0011,4=0100,5=0101, etc. The solid edges represent the hopping elements with negative energies, while the dashed lines represent positive energy hops as a result of exchange.....73

Figure 35: Operations on the graphs for representing the 2-particle Hamiltonian for a 4-site square model. Starting from the exact graph at the top, the dashed lines, representing sign flips in the transition between Fock states, are cut as in the second graph down. Finally, the dangling edges are wrapped onto the connected sites representing diagonal elements in effective Hamiltonian. ....75

Figure 36: Graph of the FNC density matrix for a 2-electron system on a 4-site ring with a path of 4 steps shown in green.....77

Figure 37: The RPG rules for selecting a new path. From left to right: The input for the RPG is a path. Select a bead that will be the moving bead. Identify the reference beads. Find the mid-states and assign weights, here illustrated by the thickness of the large arrows, with which to randomly choose the new path.....79

Figure 38: Steps for constructing observable weight from given path. From left to right, given the Path identify two consecutive states. For the two reference states identify the states which can be reached from the two reference states in a single step for the two graphs. Then sum over the two weights and normalize by  $P_{norm}$ .....81

## Chapter 1. Introduction

In the history of semiconductor device development, there has been a constant desire for robust predictors of the performance of the next generation technology. Such simulators save time and money for the researcher and the manufacturer, by helping to direct the technology vector to the path with the greatest probability of success.

The early semiconductor devices such as the BJT and the first MOSFETs could be adequately modeled using the Drift Diffusion (DD) method. The devices had dimensions on the order of microns and operated largely in the diffusive limit. However, as the overall device technology has progressed, consideration of energy transport was added to DD producing Hydrodynamic simulators capable of modeling, for example, velocity overshoot within limits. As devices continue to shrink in size, however, such methods also lose validity as predictive techniques. To remove many of the approximations required to derive transport equations on which the DD and hydrodynamic simulators are based, and to bring back the predictive nature of computational electronics, we have turned to the Semiclassical Monte Carlo (SCMC) method. The SCMC method provides a solution to the Boltzmann transport equation (BTE) that is beyond the zero- and first-order solutions provided by the DD and hydrodynamic methods, and is therefore more accurate. However, it must be acknowledged that what advantage the SCMC gains in physical accuracy is offset by its disadvantage in computational time.

In general, the SCMC method simulates a device by following a population of electrons through a device governed by the BTE, the Poisson equation, and material specific scattering rates and energy vs. wave-vector dispersion relations. This coupled set

of equations is solved stochastically at fixed time steps, and although there are several methods to solve the Poisson equation very quickly, doing so many (e.g.,100,000) times<sup>1</sup> for very large systems costs a great amount of time. Fortunately, as the devices get smaller, this problem is minimized. However, as the device size shrinks to within the quantum limit, the fundamental, and largely classical, assumptions of the BTE are challenged, and additional corrections for quantum effects must be included. These corrections further add to the time and complexity of computing a solution. In addition, just as with the DD and hydrodynamic methods, there is a limit to the predictive abilities of methods whose assumptions do not apply to the system. As a result, it is then important to look for still more accurate physical models for nanoscale devices.

The class of methods which accurately use Quantum Mechanics to describe a physical system is very broad, but includes none that carries with it all the benefits that the class of semiclassical methods have – the class to which the DD and hydrodynamic and SCMC methods belong. Seemingly the most promising of them is the non-equilibrium Green function (NEGF) method, which solves for the quantum mechanical propagator of the system using a tight-binding formalism, and potential reservoirs for the contacts. The method has been used with success, for example in predicting the single particle dynamics for nanoscale transistors in the ballistic limit. However, although there has been some success in adding scattering to the NEGF method, again with a considerable increase in computational cost, the SCMC method still has the advantage with the number of mechanisms that can be easily included, particularly with regard to carrier-carrier scattering which can be treated through molecular dynamics methods in SCMC, but escapes NEGF simulation. In addition, although the NEGF method can be

---

<sup>1</sup> The number of steps needed for statistical accuracy depends upon the specific code, the device, and the number of particles in the simulation.

constructed within the framework of mean-field theory, including the approximation of exchange effects via the Fock potential with yet another increase in computational cost, it remains ultimately a single particle picture. Both SCMC and NEGF fail to address the complete amount of exchange-correlation energy information within many particle systems. For devices that rely upon the collective effects of populations of particles, classical or quantum, both approaches have significant limitations.

A quantum method that has had success in accurately describing many-body quantum behavior is the Path Integral Monte Carlo (PIMC) method. The PIMC method is a particle-based quantum Monte Carlo method with roots in the Feynman path integral approach to quantum mechanics. Unlike the NEGF approach, it finds expected values of observable quantities for a system of many particles propagating through the system. However, since the model calculates the averages by following each of the particles separately through the system, a rigorous application of the PIMC method is immediately limited to systems with a relatively small of particle numbers and geometries, even with fixed node approximations to address the Fermion sign problem.

With the current device technology edging nearer to ‘the end of the road map,’ the current simulators need to account for the physics of the next generation of devices. For my thesis work, I have built on the SCMC and PIMC simulation approaches to that end. In Chapters 2 and 3, I describe extensions of the SCMC simulation to address 3D transport in the unconventional MOSFET material systems including III-Vs and graphene, respectively. In Chapter 2, the SCMC method is applied to a survey of III-V materials to investigate the advantage such materials have over Si in nanoscale devices. In Chapter 3, an adaptation of the SCMC method to address ambipolar transport (including Klein tunneling) in graphene MOSFETs is presented and used to demonstrate the essential transport physics of these devices. In Chapter 4, a novel tight-binding

derivative of the PIMC method, the Path Sum Monte Carlo (PSMC) method is presented and applied to a small system of two 6 atom rings, demonstrating the accuracy of the results and the possibility of generating a phase diagrams for this system and for much larger systems of graphene bilayers. In principal, the PSMC method does not suffer from same limitations of the number of particles or geometry of the system. Unlike the continuous space basis used in the PIMC, the PSMC utilizes a discrete basis set. The discrete basis set allows for the particles tracked within the simulation to reach convergence faster for a similarly sized volume, and it saves physical memory on the computer as a single integer or Boolean value must be remembered as opposed to a double precision number. Such a method could be used to calculate average observable quantities for an n-particle system that requires greater knowledge of the exchange-correlation and particle interactions than a mean-field theory can supply. In Chapter 5, a brief discussion of these results is presented and possible future work is outlined.

Finally, in Appendix A, a brief overview of the PSMC method is given followed by a small MATLAB toy model for a PSMC calculation of the average energy for a 4 site ring in Appendix B, and then a layered 6 atom ring system (as modeled in Chapter 4) in Appendix C.

## **Chapter 2. 3D-Monte Carlo Study of Short Channel Trigate Nanowire MOSFETs**

### **INTRODUCTION**

For decades, silicon has dominated the market for Complementary Metal Oxide Semiconductor (CMOS)-technology. For an equally long period, III-V compounds have been a tempting choice to overthrow Si because of their lighter electron effective masses and higher electron mobilities. The saying that “III-V will always be the material of the future” has been a prophesy fulfilled by technological advances in fabrication and device design providing faster Si-based logic. However, the recent plateau in processor speeds has necessitated a change in conventional device design to satisfy the demand for faster logic processes. Some recent progress has occurred in developing different device geometries while keeping the Si-based MOS-technology, while others have again stepped away from conventional Si-based technology toward III-V material systems.

As the gate length gets shorter, the benefit of a higher channel mobility is put into question as the devices approach the ballistic limit which does not depend on scattering within the channel. The lower electron effective mass along with a reduction in number of equivalent valleys also unfortunately leads to a reduced density of states and quantum capacitance in the channel, and, thus lower net gate capacitance and channel charge. This trade-off between density of states and bulk mobility is shown in Figure 1. In the short-channel MOSFETs of interest here, the reduction in charge carriers opposes the effective-mass-related increase in injection velocity. In addition, with reduced masses, quantum confinement effects push the charge distributions further from the oxide interface, again reducing the net capacitance and, thus, charge densities.

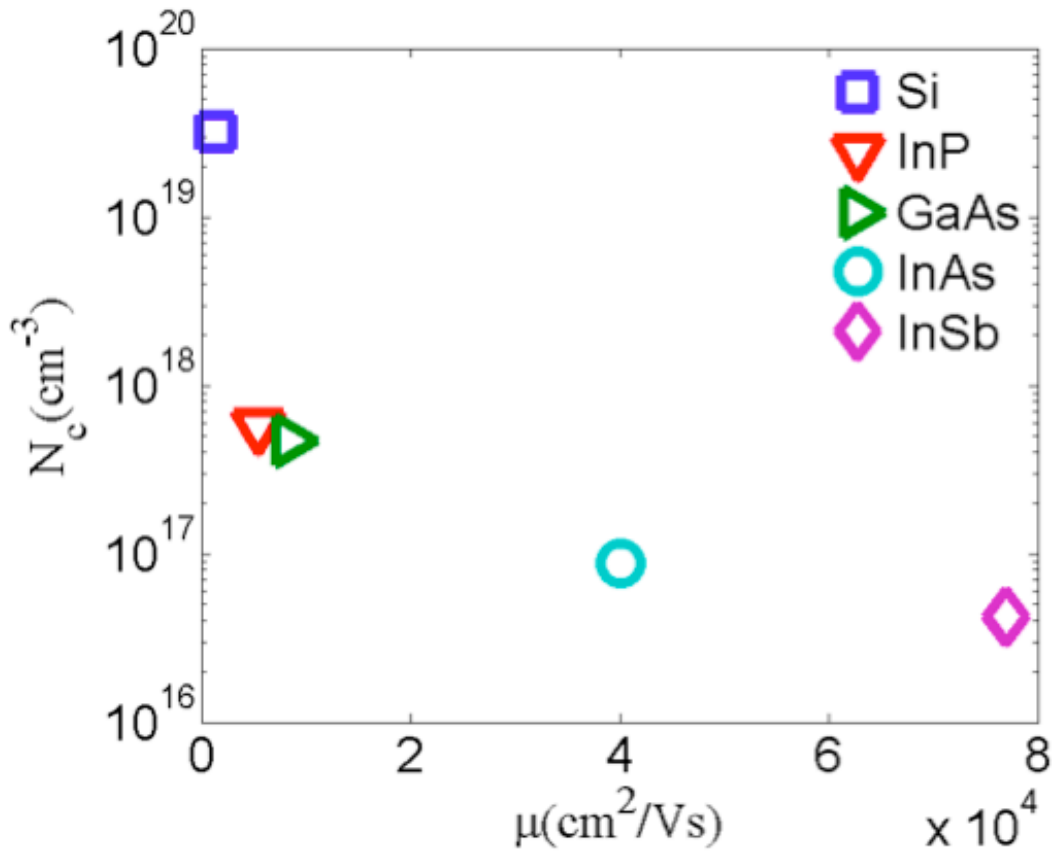


Figure 1: Scatter of conduction band effective density of states and electron mobilities for different semiconductors. From the plot it can be seen that there is a trade-off between the density-of-states and the mobility of the electron in materials, suggesting that there could be an optimal channel material choice for MOS devices.

There have been various Non-Equilibrium Green's Function (NEGF) computational studies which show that there is an optimal effective mass to be used in the ternary alloy, InGaAs, that provides the best performance [1,2]. These NEGF studies, however, assume ballistic transport. However, semi-classical and quantum transport simulations suggest that at these gate lengths, scattering is still an important factor [3],

although not in ways that can be fully characterized in terms of mobility. In addition, there is experimental evidence which shows superior performance in an InSb device structure [4]. To reconcile these discrepancies and to further understand the physics of these devices at short channel lengths, a 3D semiclassical Monte Carlo survey of a range of materials in a tri-gate nanowire structure was performed. The tri-gate structure was chosen to exploit the benefits of improved electrostatic gate control for short channel devices.

In this chapter we present the results of this study and show that, for short channel tri-gate nanowire MOSFETs ( $L_{\text{ch}} \sim 10\text{nm}$ ), InSb and InAs show superior performance to the lower mobility materials considered, as a result of the lower effective mass leading to a higher channel conductivity. First, details of the simulation methodology including material parameters are given, followed by results and analysis.

## **SIMULATION METHODOLOGY**

The materials used for this study, Si, InP, GaAs, InAs, and InSb, were chosen based on the effective mass and bulk mobility of electrons in these materials. A tri-gate nanowire MOSFET with a channel length of 10 nm and a narrow 3 nm x 3 nm square cross-section was chosen, guided by ITRS projections of device scaling [5]. The source and drain regions were each 10 nm in length and were doped n-type to  $10^{19}\text{ cm}^{-3}$  in each material as a control, while the channels were left undoped. The gate oxide was 1 nm thick. A schematic of this device is shown in Figure 2.

The simulation tool used in this survey was a 3D semiclassical Monte Carlo algorithm with a Schrödinger quantum correction to the electrostatic potential [6]. The quantum correction is obtained by solving, at each time step, the 2D Schrödinger

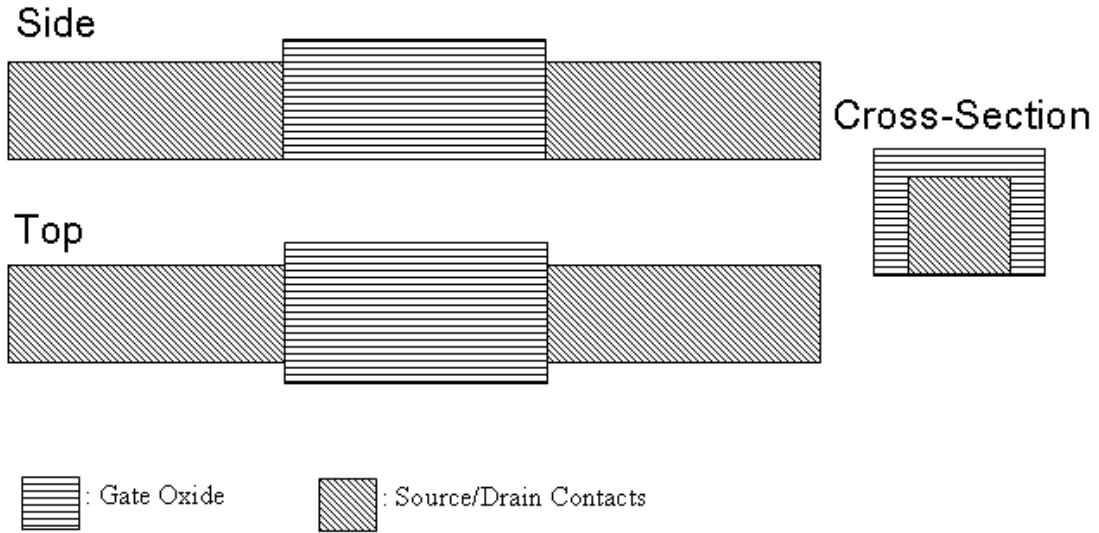


Figure 2: Schematic of nanowire MOSFET geometry with side, top, and cross-sectional view of the device. The channel length of all devices was kept constant at 10 nm with a source and drain contact length of 10 nm. The wire was a 3x3 nm square cross section with a 1 nm thick oxide barrier wrapped around three facets of the channel region. The base of the device was assumed to have a constant zero field in terms of the boundary condition.

equation across slices of the electrostatic potential obtained from the Poisson equation. Given the energy eigenvalues and corresponding state eigenvectors, a probability density is obtained for an approximate electron concentration in the slice by adding the weighted values of the point-wise magnitude squared values of the eigenvectors. The weight for each eigenvector is chosen according to the Boltzmann distribution. The potential correction to the point is then obtained by finding the equilibrium band offset as a function of position to match the density just calculated. The simulation parameters for the materials were chosen from literature [7,8] and are shown here for convenience in Table 1. The scattering mechanism parameters and types for the materials are listed in Table 2. For all materials, a non-parabolic band approximation was used. The L valley in InSb was left out of the simulation because it is much higher than the  $\Gamma$  valley. All of

		Si	InP	GaAs	InAs	InSb
$E_g(\text{eV})$		1.12	1.34	1.42	0.35	0.17
$m^*/m_0$	$\Gamma$	N.A.	0.082	0.067	0.022	0.014
	X	N.A.	0.25	l: 0.98 t: 0.19	0.64	N.A.
	L	N.A.	0.32	l: 0.98 t: 0.19	0.286	0.222
	$\Delta$	l:0.98 t:0.19	N.A.	N.A.	N.A.	N.A.
$\epsilon_r$		11.7	12.5	12.9	15.15	18.7
$\epsilon_\infty$		N.A.	9.61	10.92	12.3	16.0
$E_{\text{valley}}-E_c(\text{eV})$	$\Gamma$	N.A.	0.00	0.00	0.00	0.00
	X	N.A.	1.65	0.52	0.73	N.A.
	L	N.A.	0.83	0.33	1.02	0.45
	$\Delta$	0.00	N.A.	N. .	N.A.	N.A.
$a(\text{\AA})$		5.431	5.8687	5.6532 5	6.0583	6.479
$\alpha(\text{eV}^{-1})$	$\Gamma$	N.A.	0.83	0.61	1.39	5.719
	X	N.A.	0.23	0.204	0.90	N.A.
	L	N.A.	0.38	0.461	0.54	0.976
	$\Delta$	0.366	N.A.	N.A.	N.A.	N.A.
$\rho(\text{kg/m}^3)$		2328	4810	5360	4280	5790
$v_s(\text{m/s})$		9040	5130	5240	5670	3700

Table 1: Physical parameters used in simulation of materials.  $E_g$ : bandgap.  $m^*/m_0$ : effective mass ratio.  $\epsilon_r$ : relative permittivity.  $\epsilon_\infty$ : relative permittivity high frequency.  $E_{\text{valley}}-E_c$ : valley offset.  $a$ : lattice spacing.  $\alpha$ : nonparabolicity factor.  $\rho$ : atomic density.  $v_s$ : sound velocity

the appropriate phonon scattering processes were considered in the simulations: acoustic, inter/intravalley optical, and in the case of the III-V materials, polar optical phonon scattering. Velocity-field curves for each of the materials are shown in Figure 3. One limitation of the simulations is that surface-roughness scattering was not considered, in

large part because it is unknown for III-V materials and evolving with the technology.

However, recent Monte Carlo simulations do suggest a perhaps diminishing role of

IV	Si	III-V	InP	GaAs	InAs	InSb	
$E_{ac}(eV)$	3	$E_{ac}(eV)$ $\Gamma$ $X$ $L$	5.0 5.0 5.0 0	7.0 9.0 7.0 9.0 2	5.8 5.8 5.8	7.0 N.A. 10.0	
$D_{0th}(eV/m)$	f: $8 \times 10^{10}$ g: $8 \times 10^{10}$	$DK_{av}$ ( $10^{10}$ eV/m)	$\Gamma \leftrightarrow X$ $\Gamma \leftrightarrow L$ $X \leftrightarrow X$ $X \leftrightarrow L$ $L \leftrightarrow L$	5.0 5.0 5.0 5.0 3.0	10.0 10.0 7.0 5.0 10.0	10.0 10.0 9.0 9.0 10.0	N.A. 5.0 N.A. N.A. 0.0
$E_{1st}(eV)$	f: $8 \times 10^{10}$ g: $8 \times 10^{10}$	$\omega_{av}(meV)$	$\Gamma \leftrightarrow X$ $\Gamma \leftrightarrow L$ $X \leftrightarrow X$ $X \leftrightarrow L$ $L \leftrightarrow L$	21.9 22.2 25.7 20.9 24.3	29.9 27.8 29.9 29.3 29.0	29.9 27.8 29.9 29.3 29.0	N.A. 12.7 N.A. N.A. N.A.
$\omega_{0th}(meV)$	f: $8 \times 10^{10}$ g: $8 \times 10^{10}$	$\omega_{po}(meV)$	42	36	30	25	
$\omega_{1st}(meV)$	f: $8 \times 10^{10}$ g: $8 \times 10^{10}$	$DK_{svd}$ ( $10^{10}$ eV/m)	2	3	2	N.A.	

Table 2: Scattering parameters for the materials. In all materials, acoustic scattering was included. In Si, f and g type intervalley scattering are also included. For the III-V materials, inter/intravalley scattering was taken into account, using the standard deformation potential field used in the references along with polar optical phonon scattering. Because the X valley in InSb is so far above the conduction band minimum, it was ignored in these calculations.

surface scattering in short channel devices.[3] Another limitation to the simulation is the neglect of source to drain tunneling particularly in the lower effective mass materials.

This would increase the leakage current and degrade the off-current performance in these materials. As a result, we focus on the relative on current performance of these materials and use it as a comparison. Each device was run over a 0.5 V  $I_d$ - $V_g$  sweep in 50 mV increments past saturation with each data point run for 50,000 time steps past a 1,000 time step warm up at 0.2 fs per time step. In addition, the devices were simulated in an  $I_d$ - $V_d$  sweep to obtain output characteristics for each gate bias.

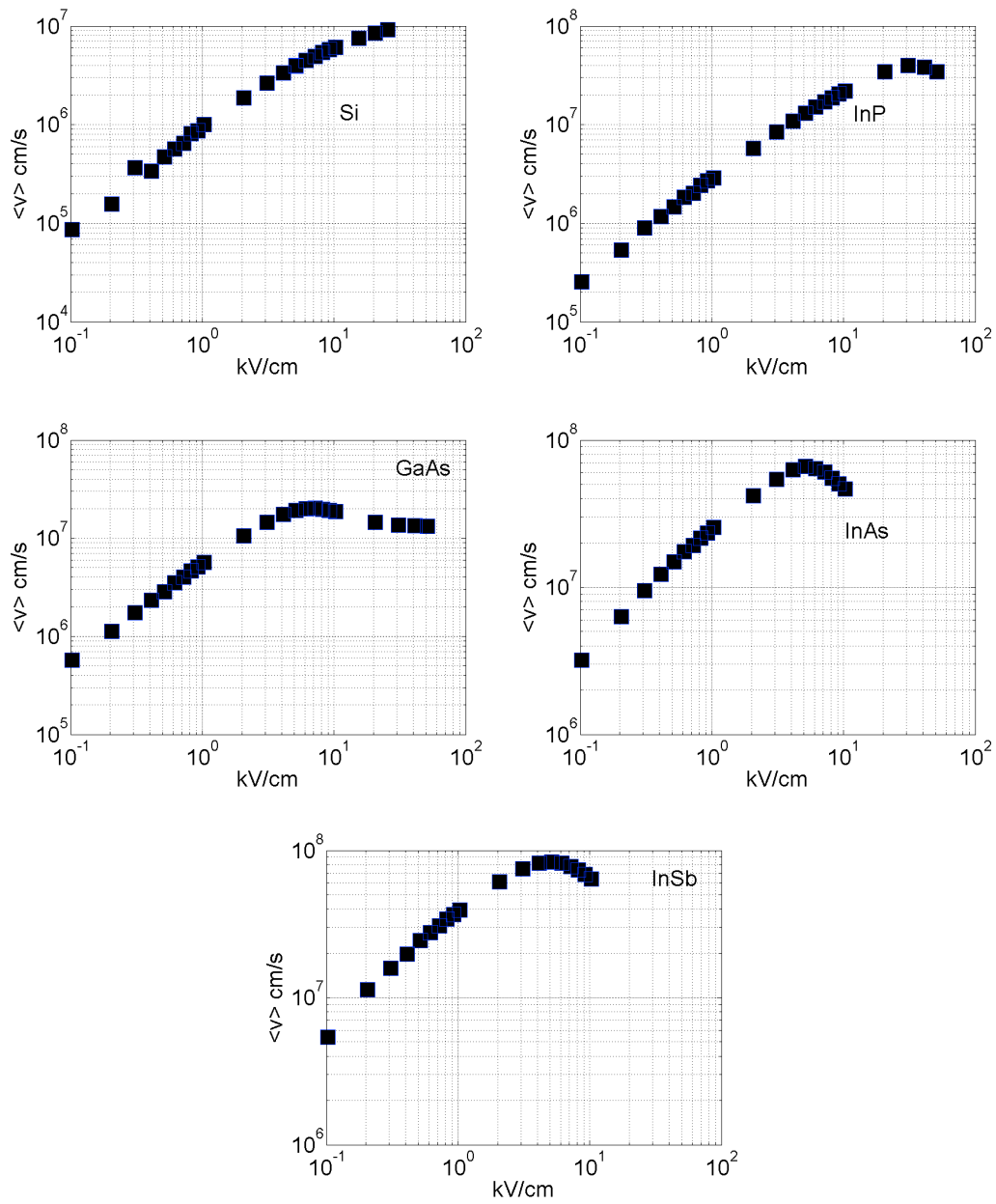


Figure 3: Calculated average velocity vs. electric field curves for the five materials surveyed using the material parameters quoted in Tables 1 and 2.

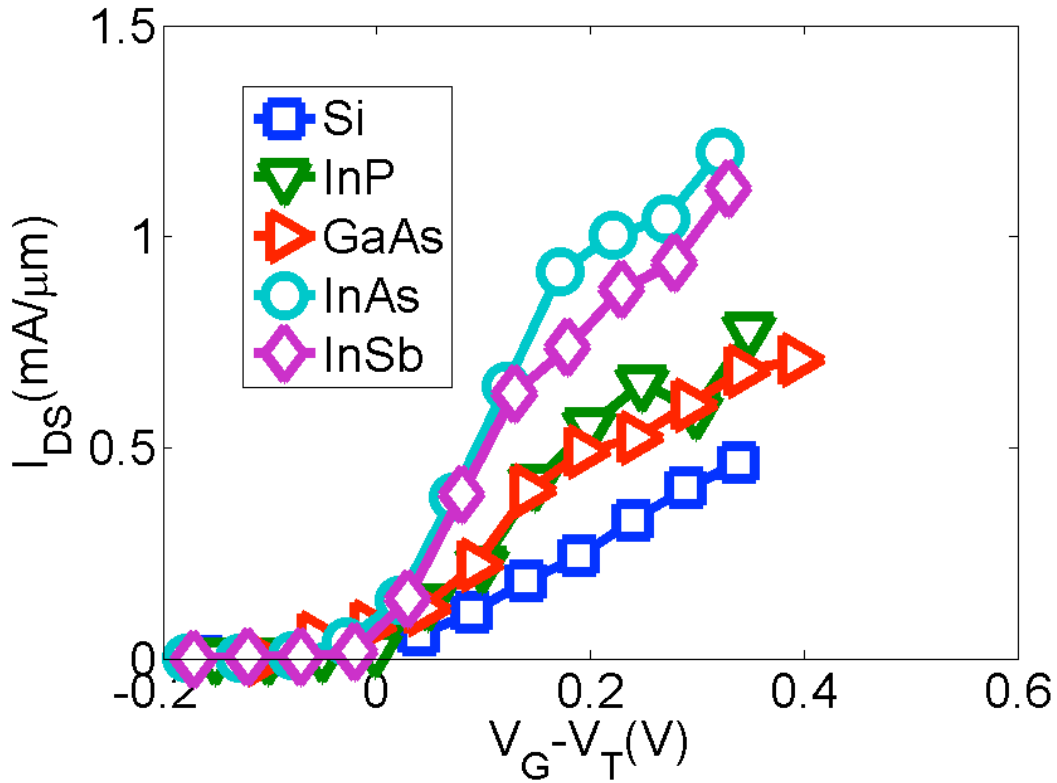


Figure 4:  $I_{ds}$ - $V_G$  curve at  $V_d=0.8V$  for Si, InP, GaAs, InAs, and InSb Tri-gate nanowire transistors. Curves were obtained from a 3D Semiclassical Monte Carlo Simulator with scattering and with a Schrödinger-type correction to the electrostatic potential to account for quantum confinement effects. The results exhibit a grouping according to effective mass, with InAs and InSb performing the best, followed by InP and GaAs, and finally Si.

## RESULTS AND ANALYSIS

Figure 4 shows the 10 nm  $I_d$ - $V_g$  transfer characteristics for each of the materials with a source drain bias of 0.8 V. InSb and InAs clearly show superior performance to the other materials. It is also apparent that the transfer curves are ordered in terms of increasing mobility, suggesting, perhaps, that significant scattering perhaps persists at shorter channel lengths for the low mobility materials. Performing the same study under

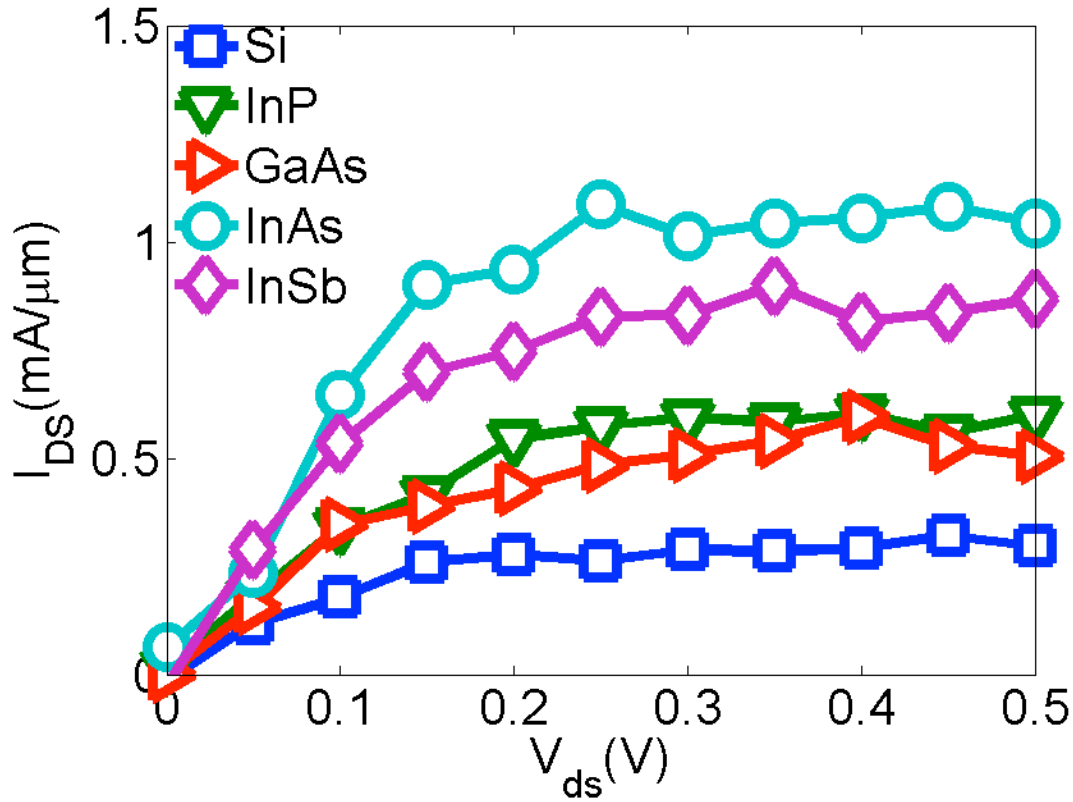


Figure 5:  $I_{ds}$ - $V_{ds}$  curves for each material with the Schrodinger correction and scattering turned on in the simulator. The gate bias was set to 0.25 V above threshold. Although noisy, the purpose of these plots is only to illustrate device saturation at the 0.8V drain-to-source bias used in each of the materials.

ballistic conditions by switching off the scattering mechanisms included in the full simulation environment, however, shows that scattering has a limited effect on III-V MOSFET performance in these simulations. Silicon, on the other hand, exhibits a  $\sim 20\%$  boost in the current in the ballistic case, as shown in Figure 6. These results imply that scattering plays a minor role in distinguishing the performance among the III-V FETs, and the utility of a ballistic-type model in comparing them is confirmed. However, to

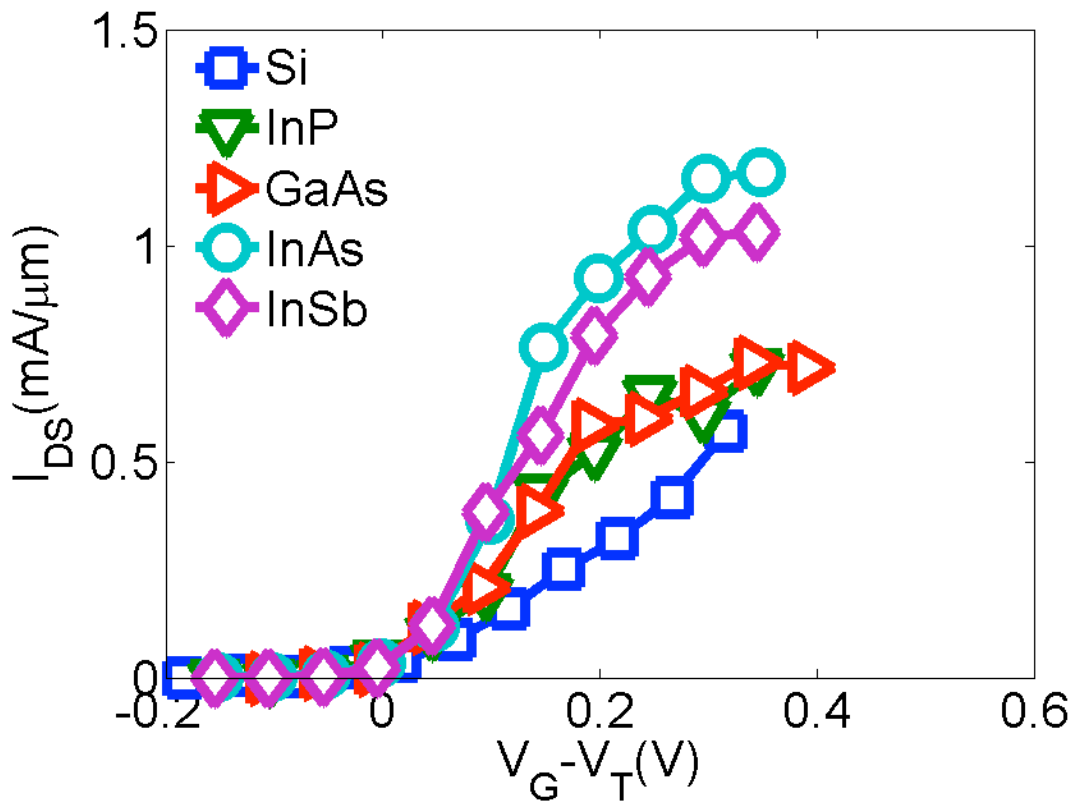


Figure 6:  $I_{ds}$ - $V_G$  curves for the five materials without considering scattering. As compared to the results of Figure 3, there is limited increase in the currents in the III-V devices, but about a 20% boost in the current in Si FETs. As scattering plays little role in the III-V materials in these simulations, the differences in currents among the III-V materials appears to be due primarily to only band structure differences among the materials. However, scattering, or rather the lack of significant scattering in III-V materials, does further distinguish the III-V MOSFET performance from that of Si MOSFETs.

recognize the full benefits of III-Vs MOSFETs as compared to Si MOSFETs in simulation still requires consideration of scattering, at least in the latter.

As mentioned earlier, absent scattering, the current is determined by the population of carriers and the velocities of the injected carriers in the channel near the

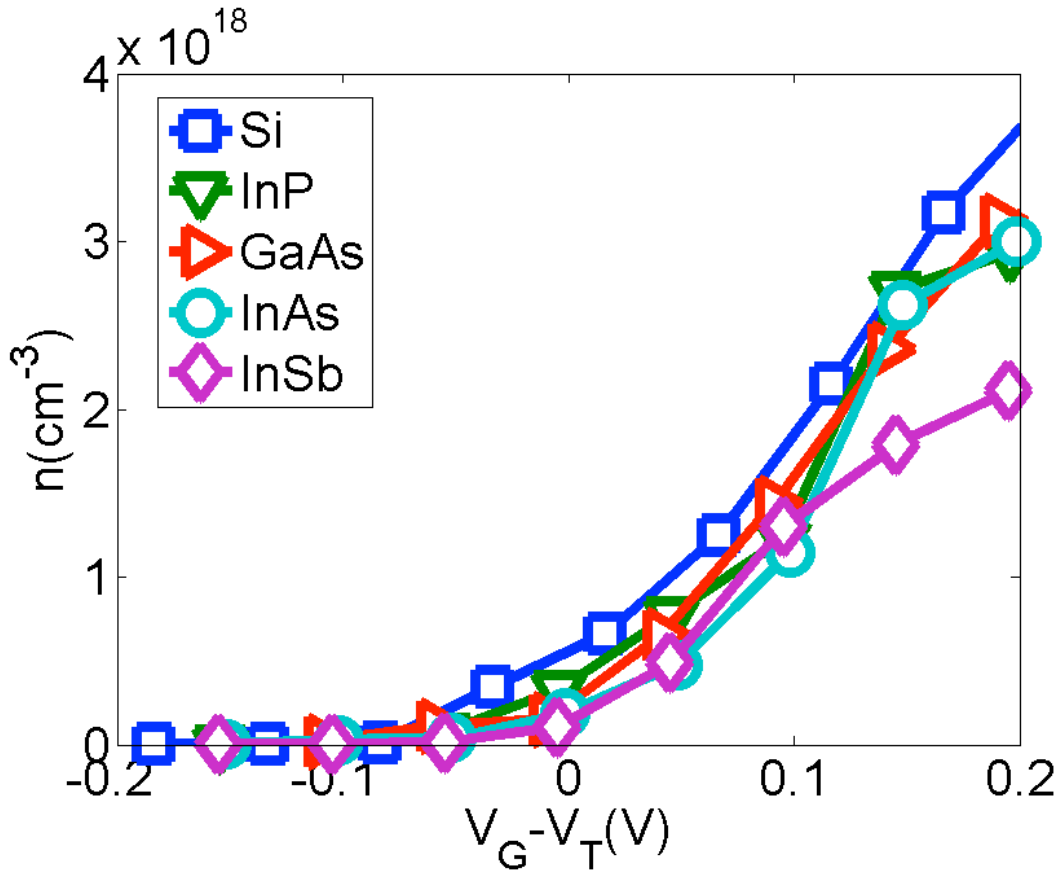


Figure 7: Time-averaged integrated channel carrier concentration of materials calculated over the volume of the channel region. The capacitances of the devices are nearly identical suggesting that the current is determined by the average velocities of the carriers.

source-channel junction. The reduced effective mass for III-V semiconductors has the opposing effects of increasing injection velocity and, as shown in Figure 7, decreasing carrier population within the channel. However, the primary source of the differences among charge densities appears to be altered effects on quantum confinement and not altered density-of-states capacitances. Figure 8 provides calculated channel charge densities absent the quantum correction but still subject to differing densities of states, yet

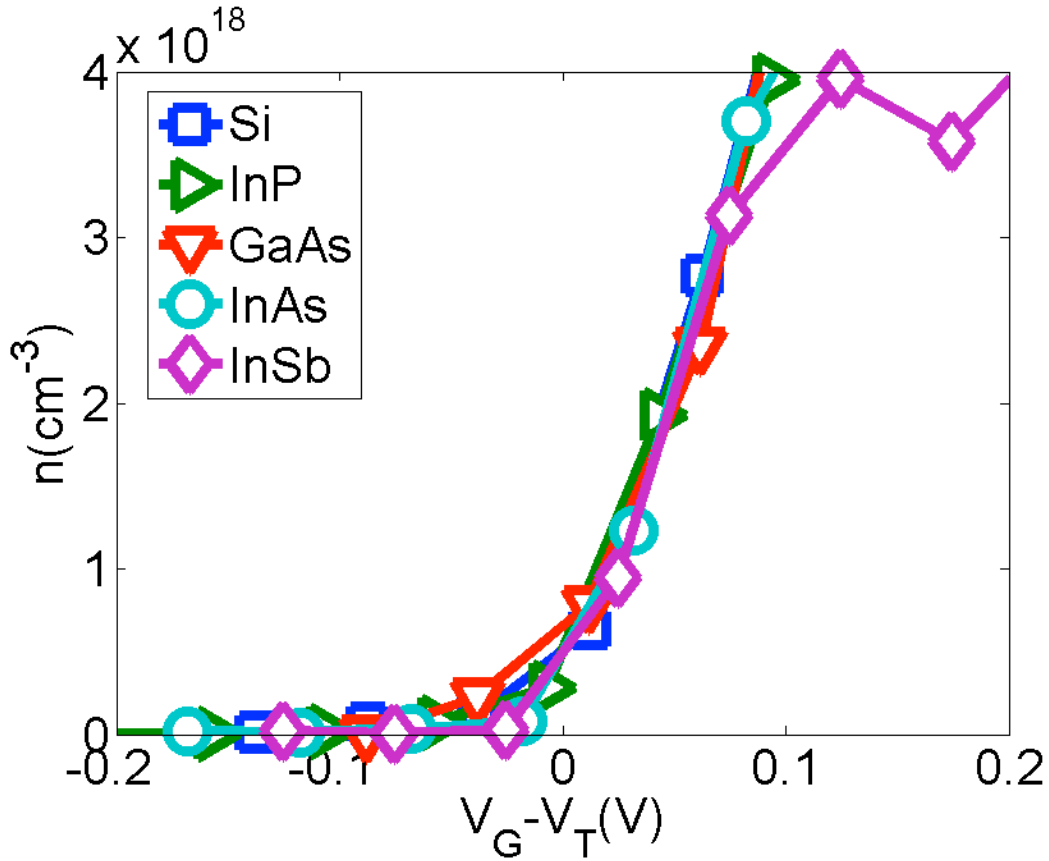


Figure 8: Time-averaged integrated channel carrier concentrations calculated over the volume of the channel without any quantum. The charge densities are nearly identical for each of the materials, suggesting that that oxide capacitance in this tri-gate structure, by comparison to Figure 7, dominate both the capacitances related to quantum confinement and the density-of-states.

exhibits little of the differences among materials exhibited in Figure 7. At least in this tri-gate structure, the capacitance appears to be dominated by the geometry-related series combination of gate-oxide and quantum-confinement capacitances. Accordingly, with the quantum correction removed from the simulation, the advantage in drive current for the lower carrier effective mass materials increases further, as shown in Figure 9.

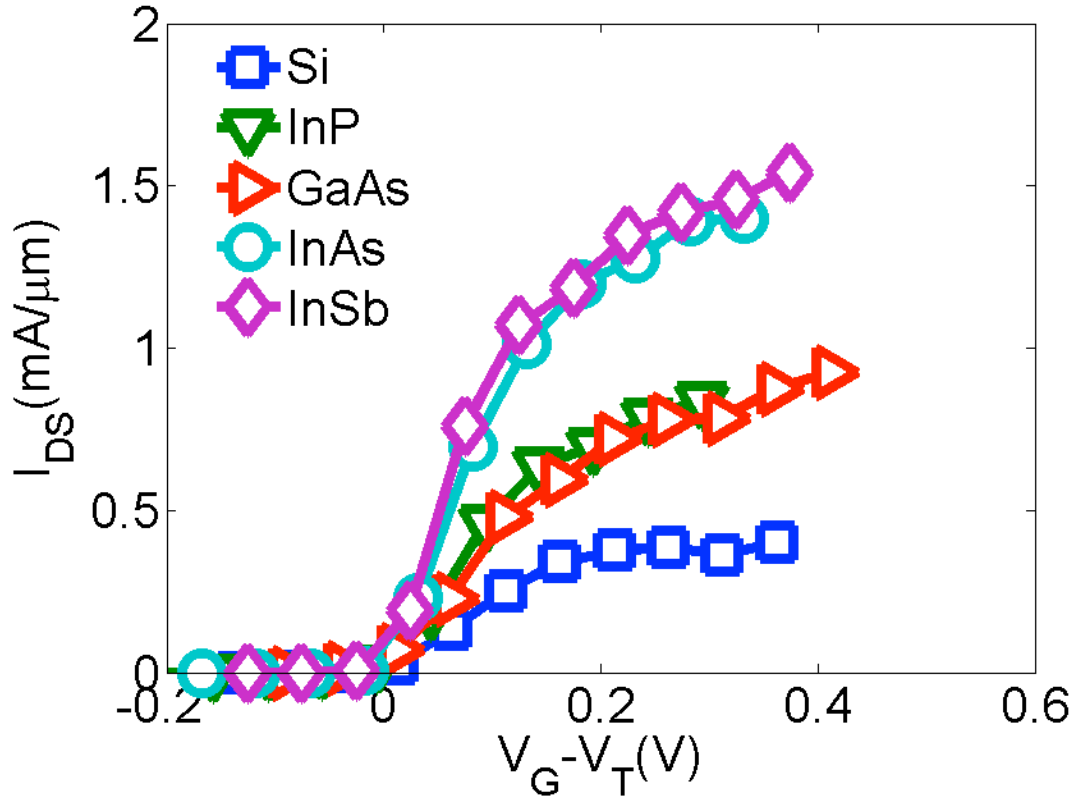


Figure 9:  $I_d$ - $V_g$  curves for FETs without any quantum correction. The currents are higher for all materials as a result of the higher carrier concentrations, as shown in Figure 8.

Finally, we note that an alternative to the Schrödinger-type correction discussed above is the "effective potential" type quantum correction. This correction address non-local features by assuming a typically Gaussian wave-packet shape for the electron and convolving this function with the electrostatic potential obtained from the Poisson equation at each time step [9]. With appropriate adjustments to the wavepacket dimensions, this method has been shown to accurately calculate inversion charge densities for 2D devices. And the correction is also less computationally demanding, particularly for 2D confinement, making it a tempting choice. However, for wave-

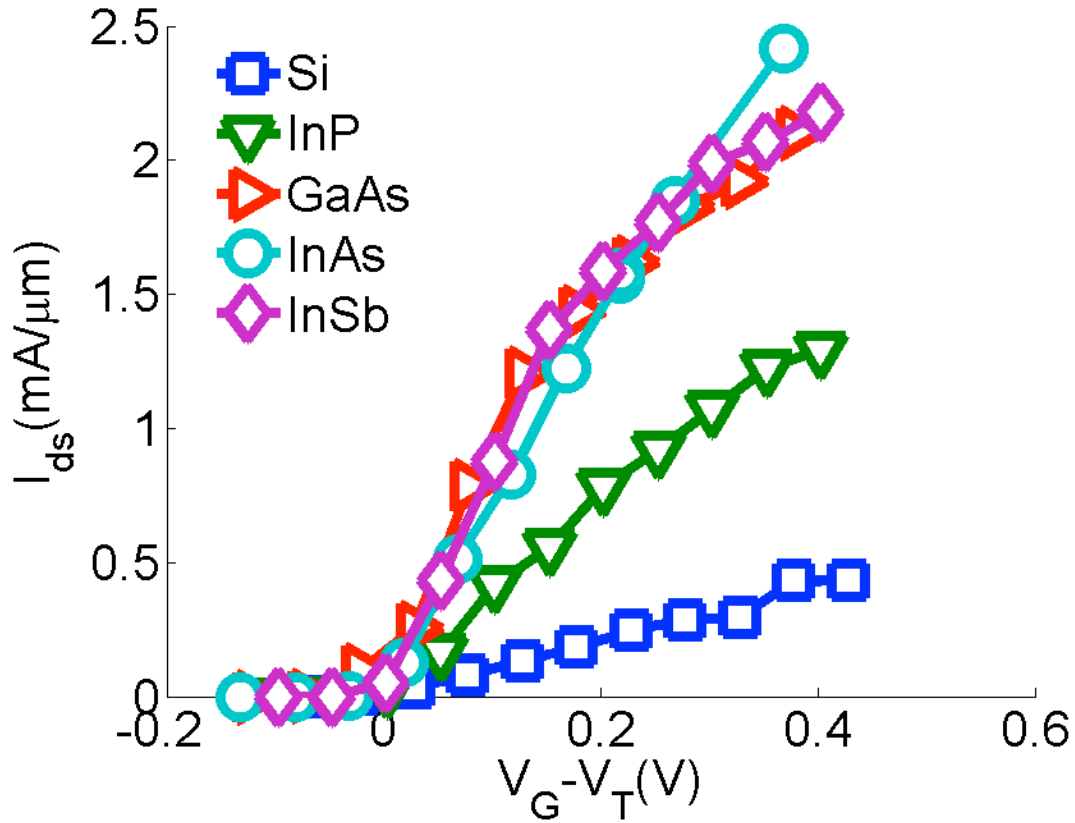


Figure 10:  $I_d$ - $V_g$  curves for devices with effective potential correction, instead of the Schrödinger-based correction used for the other calculations in this paper. Current is overestimated due to artificial reductions in the channel potential resulting from leakage of the "wave-packet" through the oxide and into the gates. The wavepacket breadths were as follows [nm]: Si: 0.87, InP: 1.73, GaAs: 1.91, InAs: 3.34, InSb: 4.19.

packets large enough to otherwise model the strong quantum confinement effects on the charge distributions in the III-V channels, we found that penetration of the wave-packet through the thin oxides and into the gate artificially lowered the channel potential, the more so for larger gate voltages. The results, as shown in Figure 10, were exaggerated

benefits for III-V materials and "quantum corrected" drive currents actually larger than those with no correction.

## CONCLUSION

Previous results comparing III-V materials for MOS devices have suggested that low effective mass materials might hamper device performance as a result of low effective density-of-states and, thus, low carrier concentrations in the channel. In this work we performed a comparison of III-V materials with Si for tri-gate nanowire MOSFETs using a 3D semiclassical Monte Carlo simulator with a Schrödinger-based correction to the electrostatic potential. It was shown that III-V materials, InAs and InSb in particular, could have a significant advantage over Si devices. Furthermore, it was shown that the higher density of states capacitances in the lower mass III-Vs did little to reduce the apparent benefits of using III-V materials in the tri-gate structures. However, benefits, though still substantial, were reduced as compared to what would be otherwise expected by increased quantum confinement effects. Finally, during our analysis, we also found that for modeling thin gate oxides and the particularly strong quantum confinement effects for III-V channels, though computationally less demanding, the use of an "effective potential" to model these effects can produce qualitatively unphysical results.

## Chapter 3. Semi-Classical Monte Carlo Analysis of Graphene FETs

### INTRODUCTION

Recent excitement over graphene has led to a flurry of research into its unique physical properties particularly surrounding its electrical characteristics [12-14]. Citing the material's reported very high mobility ( $\mu > 100,000 \text{ cm}^2/\text{Vs}$  for suspended graphene) and very high velocity saturation [15], several groups have speculated that a graphene FET may be a plausible replacement for Si technology [16]. Experimental studies have shown the effects of impurity scattering at low fields and remote optical phonons at high fields on drift velocity [15,17-19]. In conjunction with several theoretical studies [20-22], there has been some understanding of the intrinsic scattering effects in graphene in the two limits. In a recent experimental study, the two limits were joined to provide an example of the intrinsic velocity field characteristics of graphene at room temperature, providing insight into the relevant scattering processes [23].

For future device design, a reliable three-dimensional (3D) semi-Classical Monte Carlo (SCMC) simulation and understanding of the electrical performance of graphene over a range of fields is essential. Semiclassical Monte Carlo simulation provides includes more physics than drift diffusion simulators, while being simpler than Non-equilibrium Green's Function (NEGF) simulation. And despite a loss of rigor with respect to ballistic transport as compared to NEGF simulation, ensemble semiclassical Monte Carlo simulations can more easily address scattering and time-dependent transport. In order to provide such software, a reliable materials module must be produced that recreates the physical results seen in past experimental studies and allows that physics to be extrapolated to short channel devices.

Relatively few groups have attempted to simulate a graphene FET using Semi-Classical Monte Carlo. Those that have, have treated remote impurity scattering via a separate scattering rate in the form of a random phase approximation [20-22], instead of via localized point charges which affect the self-consistent potential as done here in device simulations. In this study we include a broad range of scattering mechanisms from acoustic phonons, optical phonons, and remote point impurities. This software also has a molecular dynamics capability which provides an electron-electron and, perhaps more importantly in gapless graphene in regions of low carrier concentration, electron-hole Coulomb interaction which are particularly problematic for NEGF simulation, but that capability was not used for these initial findings. In addition to the scattering mechanisms, included in this analysis is Klein tunneling. In graphene monolayers near the K points, there is a strong chance under even under small biases for electrons to tunnel from one band to another and is included in the analysis of the devices [24].

Split into two parts, this paper first discusses the transport characteristics of the bulk graphene material and associated model calibration, followed by a demonstration of a nanometer scale MOSFET simulation. We discuss the material system and the relevant scattering mechanisms both in vacuum and on a substrate. We then show calculated velocity-field curves matching past experimental results, providing discussion of the velocity saturation and low field mobility preceded by a brief discussion of the simulator and its features. A sample device is then tested in a full 3D SCMC device simulator with and without randomly placed impurities in the oxides.

## MODEL CALIBRATION AND “BULK” TRANSPORT

To accurately simulate the electronic transport in a material using a 3DSCMC algorithm, the material band-structure and the scattering mechanisms must be understood.

### Band-structure

Graphene’s band-structure is well understood with the most attention focused at the points  $K_1$  and  $K_2$  of the dispersion relation. At these locations the two bands (upper and lower) touch at a point. The  $E$ - $\mathbf{k}$  relation at these critical points is approximated by the equation,

$$E_{\mathbf{k}}^{1(2)} = \hbar v_f |\vec{\mathbf{k}}|, \quad (1)$$

where  $v_f = 10^8$  cm/s is the Fermi velocity and  $|\mathbf{k}|$  is the magnitude of the 2D wavevector relative to the point  $K_1(K_2)$  in  $k$ -space. At a temperature  $T$  of 0K, The sheet density  $n_s$  of electrons in the upper/conduction band for each valley is given by,

$$n_s = \frac{E_f^2}{\pi \hbar^2 v_f^2} \Theta(E_f), \quad (2)$$

where  $E_f$  is the Fermi energy and  $\Theta(E_f)$  is the Heaviside step function forcing the concentration to zero when the Fermi energy falls below the Dirac point. A similar equation is used when considering the number of holes within lower/valence band valleys.

## Scattering Mechanisms

Given the honeycomb packing of the carbon atoms in graphene, there are three acoustic (ac): TA, LA, and ZA, and three optical (op): TO, LO, and ZO phonon modes. However, the effects of the flexural modes ZA and ZO are ignored given the low coupling. According to several studies, the low field mobility in suspended graphene is determined by acoustic phonon branches and the high field limit by the optical branches [6-8].

In semiclassical Monte Carlo studies, it is convenient to use the deformation potential approximation in estimating the scattering rates of various mechanisms. The acoustic phonon scattering rate is calculated by the following equation:

$$S_{ac} = \frac{E_D^2 k_B T}{4\hbar^3 v_f^2 v_s^2 \rho_s} E. \quad (3)$$

A density  $\rho_s = 7.6 \times 10^{-8} \text{ g/cm}^2$  and the sound velocity value  $v_s = 2 \times 10^6 \text{ cm/s}$  are used in this study. The deformation potential,  $E_D$ , has a range of reported values between 4.7-30eV [17-19]. This range of values is a result of the experimental uncertainty in the purity of the graphene sample; at low fields, charged impurities greatly affect the mobility of the sample. In this study, we use the results of a recent experimental report claiming intrinsic velocity field characteristics that reports a value of 4.7 eV [24].

As several reports show results with charged impurities, for matching the velocity-field characteristics impurity scattering can also be added via the rate equation in (4) [18,29], as we do for mobility calculations where distributing dopants stochastically is impractical:

$$S_{imp} = \frac{hV_f^2 n_{imp}}{20E}. \quad (4)$$

Here we have modeled the impurities as being distributed homogeneously throughout the oxide with a fixed concentration,  $n_{imp}$ .

The optical phonon scattering rate is modeled by:

$$S_{op} = \frac{D_f^2}{\hbar^2 \rho_s \omega_{op} V_f^2} \times \left[ (E - \hbar\omega_{op})(N_{\hbar\omega_{op}} + 1)\Theta(E - \hbar\omega_{op}) + (E + \hbar\omega_{op})N_{\hbar\omega_{op}} \right], \quad (5)$$

with an optical phonon energy  $\omega_{op} = 164$  meV and a deformation field  $D_f = 10^9$  eV/cm, the optical phonon scattering rate exceeds the contribution from the acoustic modes at the temperatures and concentrations considered here. However, like the impurity charge scattering, remote optical phonons from oxides layered beneath or above the graphene sheet also contribute to the overall scattering rate with, and with energies typically  $< 50$ meV, the rates may dwarf any effects from the intrinsic optical phonons. These scattering mechanisms are modeled using (5) and, like the impurity scattering, are included to match experimental velocity-field curves.

For modeling the intrinsic performance limit of graphene, inter-valley acoustic scattering events must also be considered. The energies of these phonons,  $\omega_{ac}=124$ meV, and couplings  $D_f = 3.5 \times 10^8$  eV/cm are comparable to the optical modes and thus contribute a similar scattering rate. Commensurate with the Deformation Field Approximation (DFA) these scattering events are also modeled using (5).

## E-v Matching

The general SCMC scheme is described extensively in the literature [14-16]; therefore, we will only provide specific attributes to our software. The bandstructure of graphene is approximated by two identical conic valleys with the linear dispersion relation in (1). The intrinsic acoustic and optical scattering mechanisms are added as above. The impurity and remote phonon scattering mechanisms can be added and adjusted depending on the oxide and the level of charged impurity density.

Pauli exclusion is taken into account through a rejection routine checked after a scattering event nominally takes place [28]. Following a scattering mechanism, the new state is accepted or rejected with a probability according to the Fermi distribution with a forward (+) or backward (-) particle temperature  $T_e^{+,-}$  and forward or backward moving particle pseudo-Fermi energy  $\phi_e^{+,-}$

$$f(E) = \frac{1}{1 + \exp\left(\frac{(E - \phi_e^{+,-})}{k_B T_e^{+,-}}\right)}. \quad (6)$$

The electron temperature and pseudo-Fermi energies are calculated for the forward and backward moving electrons and holes separately throughout the simulation region. They are obtained locally by calculating the average directional carrier concentrations and kinetic energies and solving the resulting two equations with two unknowns for the two desired parameters.

In Figure 11 and Figure 12, we show velocity field curves for graphene in vacuum and on SiO<sub>2</sub> bottom and HfO<sub>2</sub> top respectively matching experimental values of  $\mu_0$  and  $v_{sat}$  to show accuracy of the models used. The carrier concentration and temperature were set to match the individual experimental environments given in the literature and the

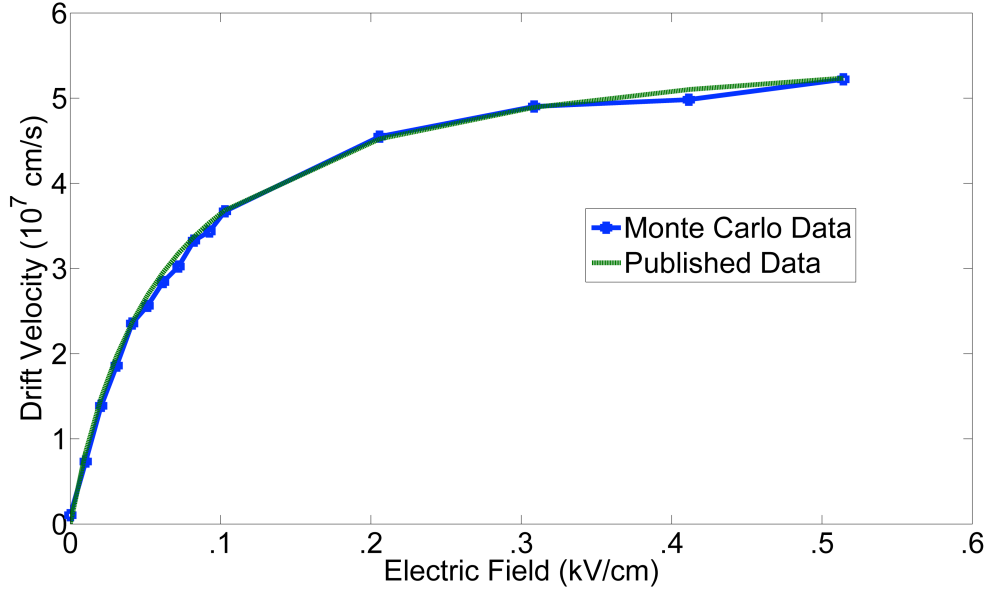


Figure 11. Velocity Field curve for graphene in vacuum matching mobility and saturation values published in literature. In comparison with Fig. 2 the low-field mobility is much higher as a result of the absence of any impurity scattering and is dominated by acoustic phonon scattering at low fields.

phonon deformation potentials then were adjusted to match the experimental data. After a sufficient number of time steps, the simulator outputs an average drift velocity of the carrier population in the graphene for a range of fields. This scatter of data points is then used to match the low-field mobility  $\mu_0$  and the saturation velocity  $v_{sat}$  to the approximate drift velocity equation (7),

$$v_d = \frac{\mu_0 |\mathbf{E}|}{1 + \frac{\mu_0 |\mathbf{E}|}{v_{sat}}}. \quad (7)$$

At low fields,  $\mu_0 \mathbf{E} \ll v_{sat}$ , the velocity field curve is approximately linear with the slope  $\mu_0$ . Like other material systems such as Si, GaAs, etc. the low field regime is

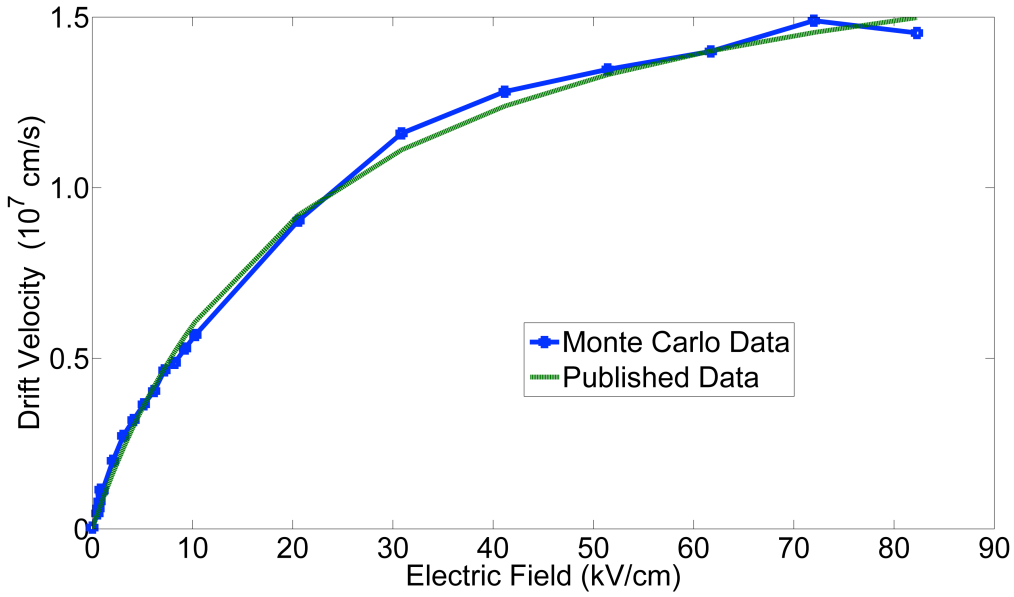


Fig. 12. Velocity field curve for graphene on SiO<sub>2</sub> bottom and HfO<sub>2</sub> bottom matching published data for the mobility and saturation velocity. The drift velocity at low fields is dominated by scattering from remote impurities in the silicon and saturates at very high fields from optical phonons.

dominated by acoustic phonon scattering processes with some optical phonon absorption. A deformation potential  $E_D=4.7\text{eV}$ , deformation field for optical phonons  $D_f = 10^9\text{eV/cm}$ , and intervalley acoustic phonons  $D_f = 3.5 \times 10^8 \text{ eV/cm}$  were found to give the best fit. Figure 13 exhibits the scattering events in the simulation for a given applied field in vacuum: we show the average occurrence of acoustic and optical scattering events as a percentage of the total scattering events. Acoustic phonon scattering is most significant at low-fields for intrinsic graphene. However, at higher fields, the optical phonon emission begins to dominate as it fights the rising average energy of the carriers and causes the average velocity to saturate.

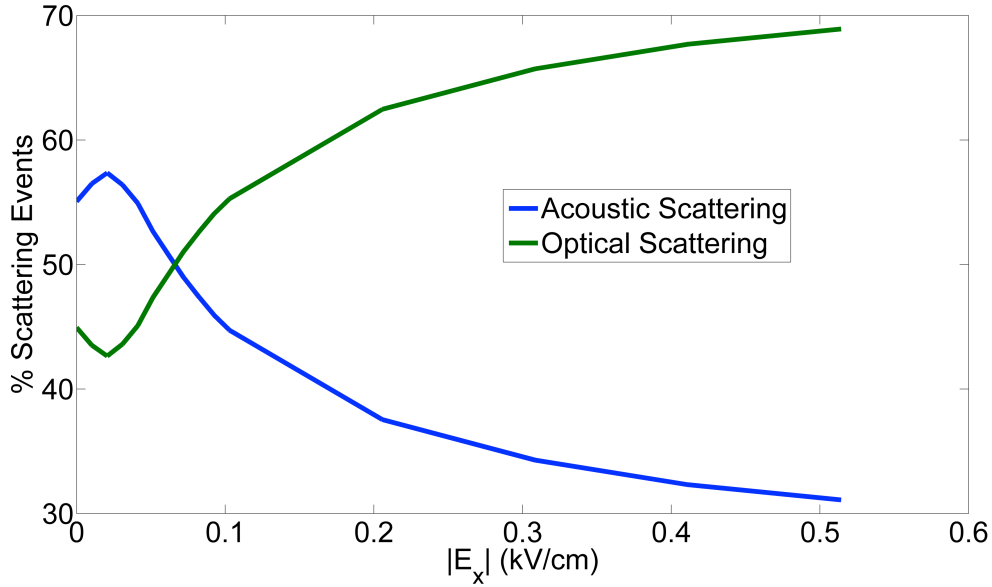


Fig. 13. Percent scattering events as function of field. At low fields acoustic scattering mechanisms dominate followed by optical phonon scattering at higher fields causing the velocity to saturate.

However, in most experiments so far, the electronic transport at low and high fields is most strongly affected by charged impurities and optical phonon modes, respectively, in a neighboring oxide layer [18]. Our results for percentage of total scattering with these latter mechanisms included are exhibited in Figure 14. In this case, an  $\text{SiO}_2$  substrate and a  $\text{HfO}_2$  gate oxide, were used. The impurity scattering rate is well understood from empirical evidence showing the direct relationship between conductance and impurity sheet density.  $\text{SiO}_2$  and  $\text{HfO}_2$  have optical phonon energies of 55 meV and 12.4 meV [32], respectively, which are much less than the 164 meV and 124 meV for the inter-valley scattering mechanisms intrinsic to graphene. As a result impurity scattering dominates at low fields where the the calculated low-field mobility drops from  $\sim 100,000$

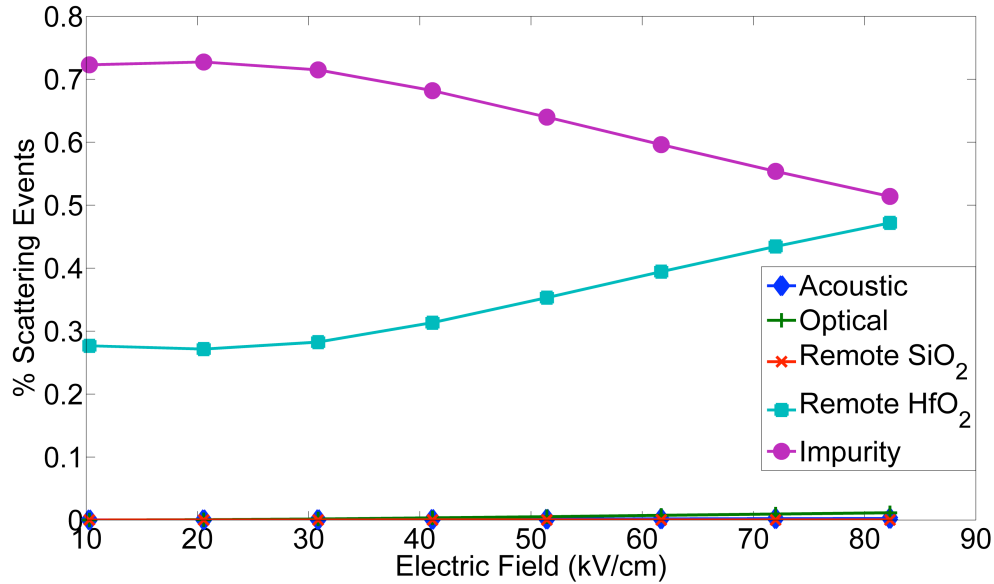


Figure 14. Percent scattering events as function of field on SiO<sub>2</sub> bottom and HfO<sub>2</sub> top. Remote impurity and remote optical phonon scattering are majority processes suppressing the low-field mobility and drift velocity.

cm<sup>2</sup>/Vs to ~500 cm<sup>2</sup>/Vs with an impurity concentration of 5x10<sup>12</sup> cm<sup>-2</sup>, and remote optical phonon scattering dominates at high fields.

### Zener Tunneling

As a result of the zero band-gap in graphene monolayers, electrons from the lower band may easily tunnel into the upper band and vice versa. This tunneling current will contribute to the observed transport, resulting in a failure to saturate near pinch-off as reported in all but one experimental study of graphene FETs. (We further note that, although not switched on in this work, the molecular dynamics treatment of carrier-

carrier scattering will provide increase opportunity for interband tunneling via local fluctuations in potential).

The tunneling current density  $J$  and resultant injected carrier distribution  $n$  is given by:

$$|\bar{J}_e| = \frac{e}{\pi^2} \int \partial^2 k v_g(k_x) (1 - f_{left}) T(k_y) f_{right} \quad (8)$$

and,

$$n(k_x, k_y) = \frac{1}{\pi^2} \int_{k_y} \int_{k_x} \partial^2 k' (1 - f_{left}) T(k'_y) f_{right} \cdot \quad (9)$$

The transmission probability  $T(k_y)$  is obtained through WKB analysis [24].

$$T(k_y) = \exp\left(-\frac{\pi |k_y|^2 v_f \hbar}{4eF}\right) \quad (10)$$

To translate these formulae into a working simulator of discrete electrons and holes for the our 3D SCMC, we define  $N_*$  as the number of particles passing through a cell in a discrete grid of graphene of width  $\Delta y$  in time  $\Delta t$  with flux density  $J$  as calculated in Eq. (8). We then distribute this number of particles with momentum according the distribution obtained in Eq. (9).

As calculation of the above as explicitly shown would be cumbersome at every grid point and every time step of the simulation, (8) and (9) are approximated by removing the Fermi distributions within the integrals and adding an additional rejection

step at the end to account for Pauli exclusion. This method both allows for more statistical variation in the flux density and speeds the numerical calculations.

## **DEVICE SIMULATION**

In this section we will discuss the simulation of short-channel graphene MOSFETs. The basics of SCMC simulation being well known, we will not describe the details of the SCMC simulation apart from its limitations and the device geometry, but will primarily focus on the physical mechanisms which limit the operation of the devices. Specifically, we will investigate the effects of scattering, Klein tunneling, and remote impurities.

### **Device Geometry**

The device geometry used in these simulations is a top- and back-gated MOSFET with a single graphene ribbon with a channel length of 80 nm and source and drain region lengths of 10 nm each. The top and bottom oxide gates are respectively 4 nm and 10 nm thick of SiO<sub>2</sub>. The channel width was modeled as 10 nm. However, we have ignored any gap opening due to quantization which is predicted to occur for perfect armchair nanoribbon of specific widths, but would nevertheless be limited at this width. Similarly, there is no treatment of edge roughness which has been predicted to degrade transport including any otherwise increased on/off current ratio due to such gap opening and to produce substantial device-to-device variability [30]. In addition, any effect from interface roughness with the oxide is not taken into account. Therefore, to a reasonable degree, these particular simulations can be thought of as 2D and the device as infinitely wide.

However, even here, a 3D treatment remains necessary to model impurity effects. Through comparison with free-standing graphene and the mobility temperature dependence, charged impurities in the oxide layers of fabricated graphene FETs have been shown to severely degrade the mobility [16,18,29]. These scattering effects may be reasonably modeled through the scattering relation (4) for mobility calculations. However, this approach, e.g., does not capture other effects arising from the presence of charged impurities including carrier puddling. Positively (negatively) ionized impurities in the oxide layers near the graphene interface form divets in the potential within the graphene around these impurities, trapping electrons (holes) near equilibrium at low carrier densities to form charge carrier puddles [29]. These puddles form a residual charge density which, in turn, shifts the voltage of the conductivity minimum locally. Therefore, in device simulations, we place point charges randomly throughout the oxide region while consistent with a given impurity density. The oxides were initially populated with fixed singly positively charged impurities of density  $N_{\text{imp}} = 5 \times 10^{11}/\text{cm}^2$  commensurate with current experimental values [30].

### **Band-to-Band Tunneling and Lack of Saturation**

As a result of the zero band gap located at the K points of the graphene bandstructure, even a small field may induce an electron to tunnel between valence/bottom and conduction/top bands, with a unity transmission probability (for normal incidence to barrier) right at the Dirac point. The effect will manifest itself in a graphene FET under sufficient applied source drain field as a non-saturating drain current. This pinch-off in the channel would normally cause the device to saturate and the current voltage relation to flatten out, as in a regular MOSFET. However, as it takes

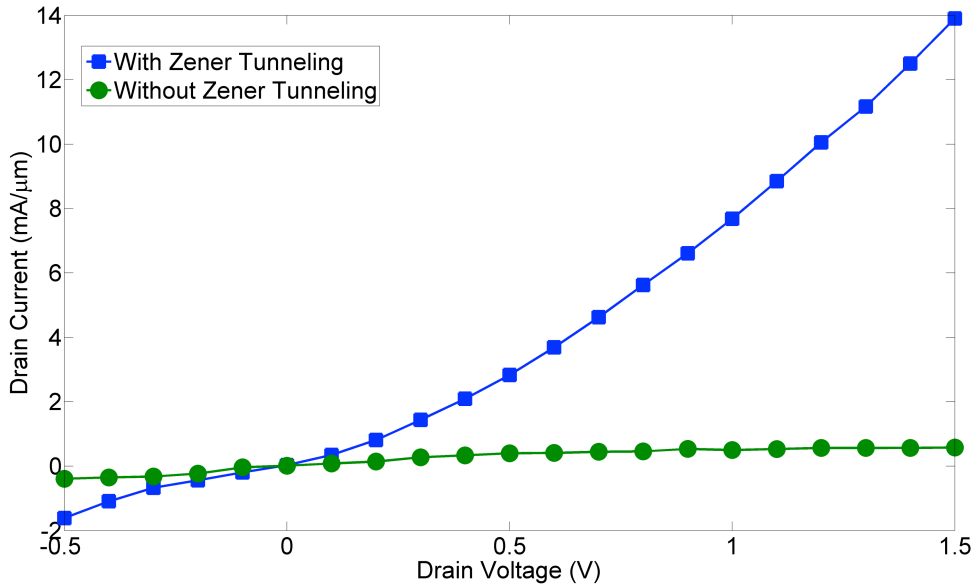


Figure 15. Comparison of currents from devices with and without the Klein tunneling. As seen, the effect of Klein tunneling on the current is very strong and causes the device to have difficulty saturating even at very high drain biases. Without the tunneling, the device acts like a conventional MOSFET. The top gate bias was set to 100 mV and the bottom gate was grounded.

a field to deplete the carriers, this same field causes carriers to tunnel into the depletion region, preventing saturation.

Simulating a graphene MOSFET with the Klein tunneling turned off produces a substantial saturated drain current with increasing drain voltage, as shown in Figure 15. However, with the tunneling turned back on, the current fails to saturate and even increases somewhat super-linearly as both the energy separation between the source and drain Fermi levels and the tunneling probability at any given energy increase with increasing channel field.

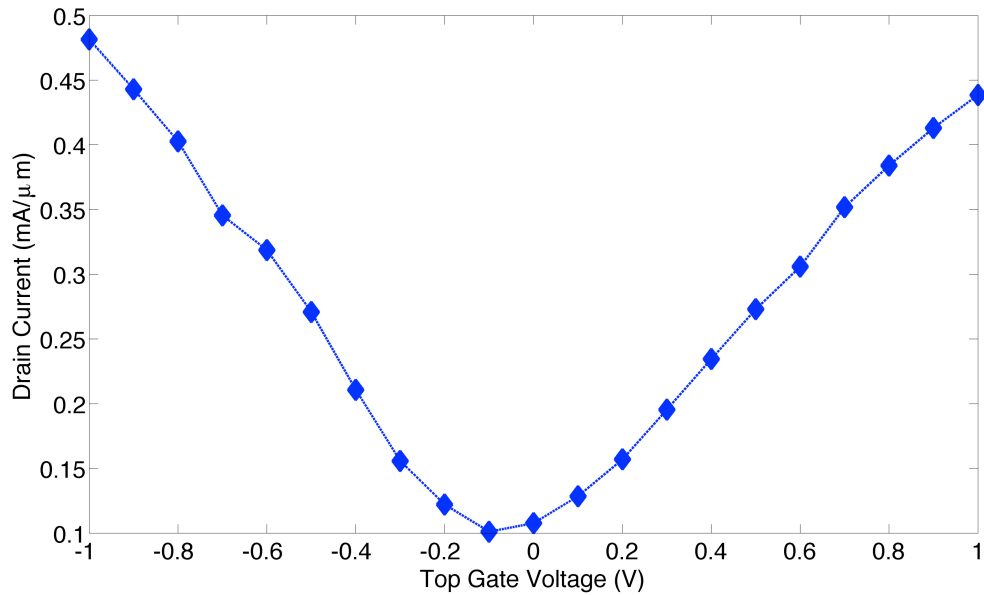


Figure 16. Drain current from device with oxide impurity concentration of  $5 \times 10^{11}/\text{cm}^2$  at fixed drain voltage of  $-50\text{mV}$ . Plot shows expected qualitative behavior as the Fermi level passes through the Dirac point, broadening both by temperature and perhaps charge puddling.

### Transport and Remote Impurities

The carrier mean free path in extrinsic graphene is long but becomes considerably shorter with phonons and impurities present in the adjacent oxide layer, with both potentially having a significant effect on bulk transport as per Figure 14, although remote phonon scattering is substantially reduced here with the elimination of  $\text{HfO}_2$ . Figure 16 shows drain-current vs. gate voltage characteristics for a fixed  $-50\text{ mV}$  drain voltage. As a result of the zero band-gap and symmetric bandstructures, we see significant current and ambipolar transport behavior with no true off state, with some asymmetry due to the drain bias. To help isolate the contributions to transport, Figure 17 shows the drain current as a function of the top gate voltage applied for three different systems: one with

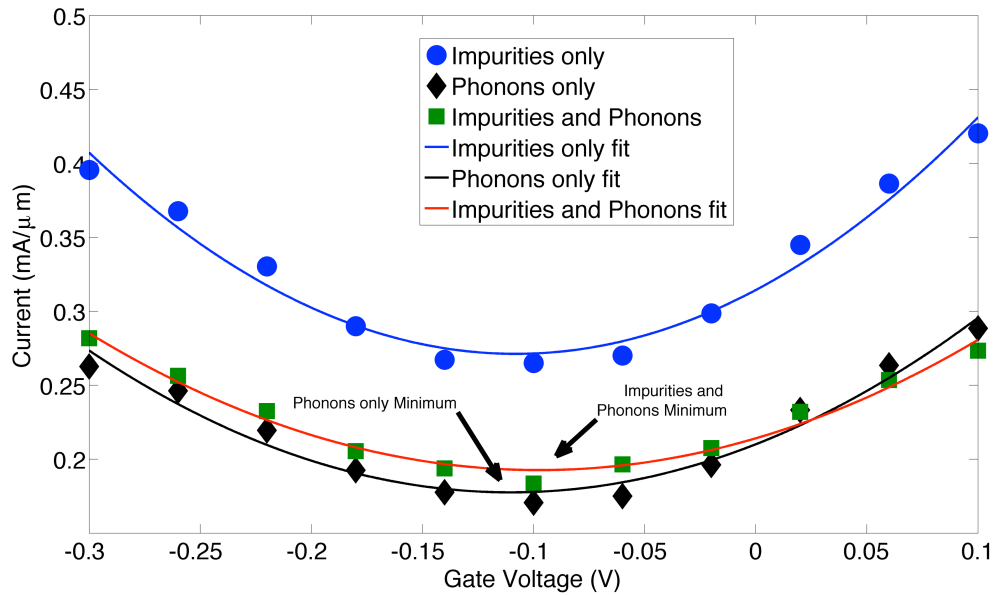


Figure 17. Comparison of currents for fixed drain bias with phonon scattering and impurities (squares), phonon scattering only (diamonds) and impurities only (circles). There is clearly an increase in the current with phonon scattering turned off, but less change with impurities removed from the oxide layers. However, using a parabolic fit to the minimum of the curves shows a small shift in the position of the minimum current and a slight broadening of the I-V characteristic as a result of the impurity-altered electrostatics.

phonon scattering and impurities, one with phonon scattering only, and one with impurities only. We also increased the drain voltage somewhat to  $-100$  mV and the back gate was grounded. As seen in Figure 17, when phonon scattering is turned off the current increases substantially, while when impurities are removed, the effect is more subtle, suggesting that phonon scattering is the dominant process here. To try to better exhibit the effects of remote charged substantially increased the impurity concentration from its initial  $5 \times 10^{11}/\text{cm}^2$  value to  $2.3 \times 10^{12}/\text{cm}^2$ , to obtain the results of Figure 18. Compared with the "impurities only" results in Figure 17 reproduced in Figure 18 for

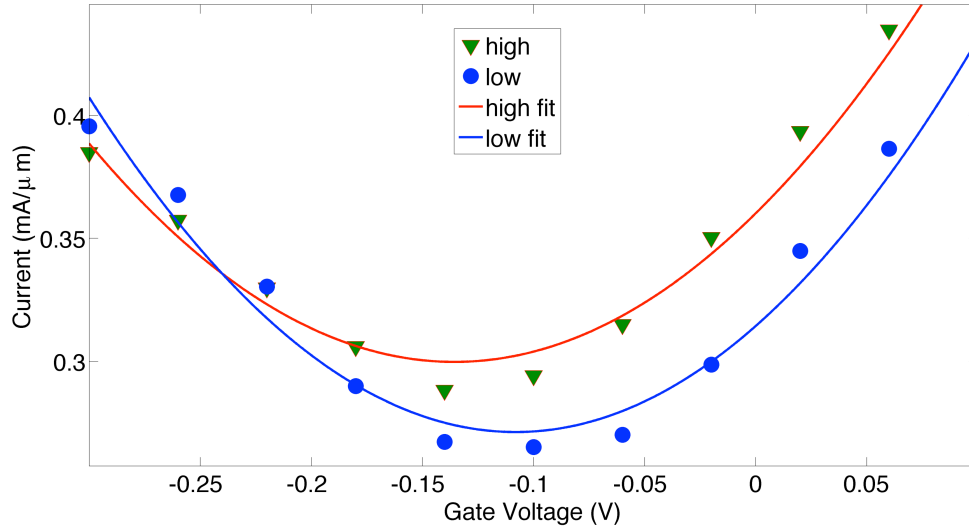


Figure. 18: Comparison of currents for fixed drain bias with high and low impurity concentrations in the oxide layers above and below the graphene layer. There is a clear shift in the current minimum voltage and broadening as a result of impurity-adjusted electrostatics. In addition, there is an increase in the current minimum as a result of impurity-induced fluctuations in the potential profile in the channel and associated charge puddling.

comparison, there is an increase in the minimum current and a broadening of the current-gate-voltage relation, in addition to the shift of the center of the distribution to lower gate voltages as expected for the positively charged impurities.

If the effect of discrete impurities were treated as a scattering term within a random phase approximation, the increase in impurities would be expected to decrease current flow. Therefore, the broadening and increase in the current flow appears to be a result of the discrete-impurity-induced fluctuations in potential profile and associated charge puddling, as shown in Figures 19. In 19(a) we show the 1D time averaged carrier

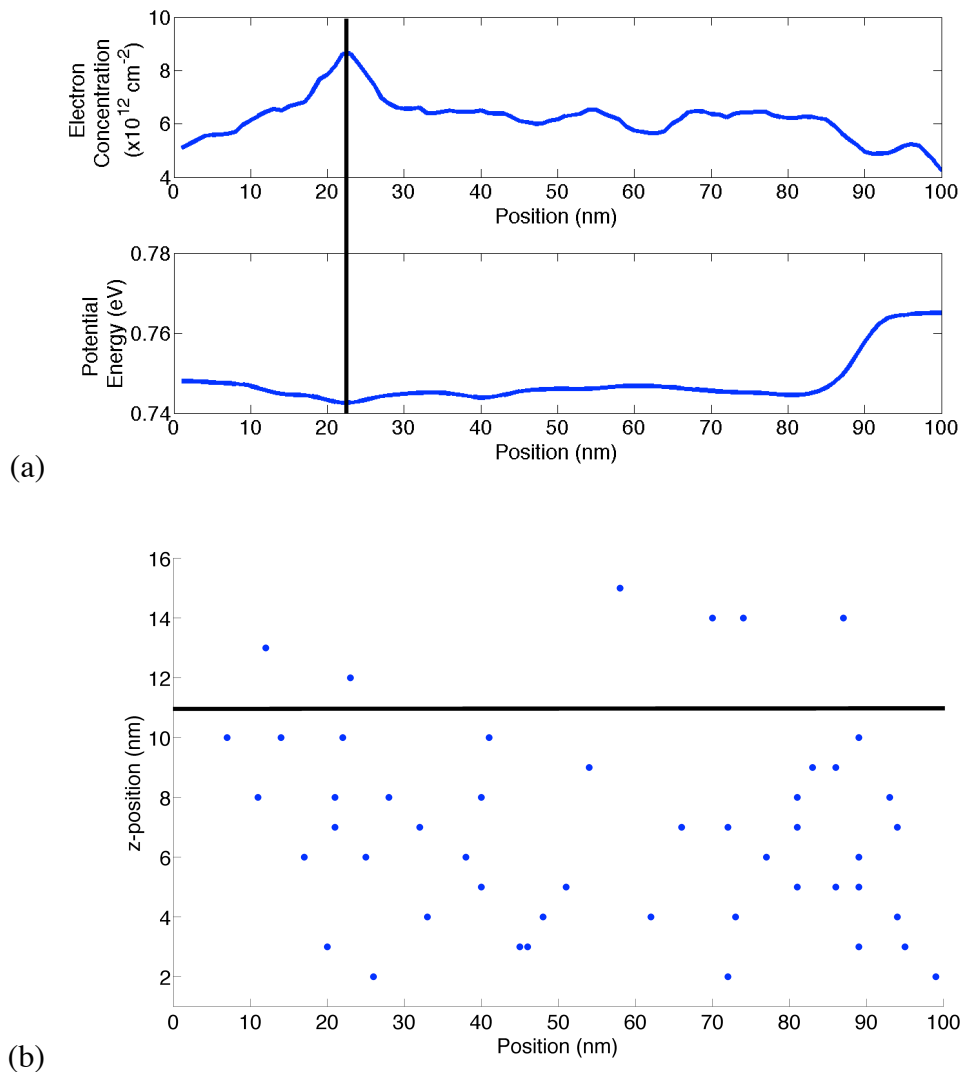


Figure 19: (a) Time averaged 1D plots of the electron concentration on top and the potential profile on bottom. There is a clear peak in the concentration above a trough in the potential where impurities are placed. The dark vertical line show the alignment of electron concentration peak and that the peak and potential trough. (b) Fixed impurity placement within the oxides along the channel. The dark horizontal line indicates the graphene layer. The dots scattered on either side are the fixed charged impurities in the oxide layers. In the same region around the peak in concentration in (a) there are several impurities within a nanometer of the graphene layer. Note that the impurity locations vary in three dimensions, while only two are shown here.

concentration along the length of the device and below it the 1D time averaged potential profile resulting from the discrete impurity profile shown in 19(b). One large peak in the electron concentration above a trough in the potential profile is near several impurities close to the graphene layer is highlighted for illustration. This effect on drain current can be explained in two qualitative ways. First, within a drift-diffusion analysis, the charge puddling forms a residual local charge densities which, in turn, shifts the local voltage of the conductivity minimum as noted in Section III-a, smearing out the overall current minimum with respect to gate voltage and, perhaps, providing percolation paths to aid current flow. And with interband tunneling rates that, while large, still vary exponentially with the field, the potential fluctuations provide increased opportunities for interband tunneling and, thus, increased current flow again. In the end, through the inclusion of discrete charge impurities, the simulated effects of charged impurities seen here, mirror those found in experimental mobility measurements.

## CONCLUSION

We have presented a 3D SCMC simulator for a graphene MOSFET. We calibrated our material simulation by matching experimentally obtained values for the bulk mobility and velocity saturation with good agreement. We included a full range of phonon scattering mechanisms, intrinsic and extrinsic, and remote impurity charges. We also modeled Klein tunneling and, in device simulations, treated impurities as localized Coulomb centers within the self-consistent potential function rather than via a scattering rate approximation. The necessity of these latter two treatments has been demonstrated via simulations of 80 nm channel length graphene MOSFETs.

## **Chapter 4. A Path-Sum Monte Carlo Approach for Many-Electron Systems Within a Tight-Binding Basis**

### **INTRODUCTION**

In this work we introduce a Path-Sum Monte Carlo method (PSMC) for calculating many-electron exchange-correlation effects within a tight-binding formalism. The approach represents a tight-binding variation on Path Integral Monte Carlo analysis [36,37]. To maintain computation tractability in the presence of the sign change in the wavefunction under exchange for Fermions, the approach employs a fixed node (FN) approximation, actually two variations on a FN approximation, to obtain upper and lower bounds with respect to the total energy of the many electron systems.

Our ultimate goal is to allow analysis of complex many electron systems beyond the limits of mean-field theory in which, for example, superfluidity has been predicted in adjacent n-type and p-type graphene layers separated by a thin dielectric via exciton condensation, much as in III-V quantum well systems [31] but at much higher temperatures, potentially above room temperature [33]. In principle, not only do exciton pairs form, but quantum coherence is established between the layers which maximizes the interlayer exchange interaction. The condensate may then allow enhanced interlayer tunneling currents up to some critical current [31,33, 44]. This system is now being considered for, e.g., ultra low-power switching applications [32], and variants of Hartree-Fock mean-field theory have been used to in part estimate the phase diagram for the critical temperature above which the condensate is destroyed [31,33-35]. However, Hartree-Fock mean-field theory employs an effective if non-local quasi-single-particle pseudo-potential approximation to the Coulomb interactions among the electrons

including exchange effects. Use of mean-field theory can overestimate the critical temperature for condensate formation, while neglecting the self-consistent dynamic screening or treating it via non-self-consistent and/or static screening approximation can lead to substantial overestimations or underestimations of the critical temperature, respectively [33]. In contrast, PIMC and this PSMC variant allow the Coulomb interactions among the electrons to be treated including both exchange and correlation effects and self-consistent screening absent this quasi-single-particle approximation.

The goal of this work, however, is only to introduce our PSMC approach and test it via application to a simple trial atomic orbital system for which, unlike for complex systems such as the two-layer graphene system above, exact results can be obtained for comparison. Specifically, we consider a system of either four or six spinless (a limitation of the model, not the method) electrons confined to two parallel six single-orbital-atom rings (12 atoms and orbitals total). In the following we will describe the essential elements of the FN-PSMC algorithm (Section II), describe and characterize the exact behavior of our model 4 or 6 electron, 12 atom system (Section III), and then compare results from our FN-PSMC method to the exact results (Section IV).

## **PATH SUM MONTE CARLO**

### **General formulation**

To confirm that a condensate is being formed in such a two-layer system, real or trial, first our PSMC method must be able to establish that excitons are being created between layers. Such pairing can be shown by observing increased correlation between the electron and hole locations on opposite layers and the associated change in average

energy as the layers are moved closer together for some fixed temperature. As the layers are moved closer together and excitons are formed, there should be an observed drop in energy below what would otherwise be expected. However, in practice here as with other studies [33-35], we do not simulate holes in the system directly, but rather simulate the entire collection of electrons and, e.g., look for anti-correlation between the locations of electrons on opposite layers. Secondly, enhanced quantum coherence between the layers must be identifiable via the PSMC method to confirm condensate formation. As the condensate is formed, we can track the increase in the expectation value of the interlayer hopping matrix elements as interlayer phase coherence is established [31,33-35].

As noted in the introduction, the PSMC approach represents a tight-binding variation on Path Integral Monte Carlo analysis [36,37]. The PSMC method deviates from the Path Integral Monte Carlo method in two ways: 1) we discretize our space into single particle states as opposed to a continuous space, and 2) we start the analysis with a discrete Fock-space basis as opposed to a continuous real or momentum space basis.

The partition function for a system with Hamiltonian  $\hat{H}$  at inverse normalized temperature  $\beta = 1/k_B T$  may be written with any convenient basis set  $\alpha$  which spans  $\hat{H}$  as:

$$Z_\beta = \sum_\alpha \langle \alpha | \rho_\beta | \alpha \rangle = \sum_\alpha \langle \alpha | \exp(-\hat{H}\beta) | \alpha \rangle$$

This partition function may be written as a sum-over-histories, or paths, of discrete states by expanding the density operator into a product of  $M$  shorter (imaginary) time density operators and identity relations.

$$\begin{aligned}
Z_\beta &= \sum_{\alpha_0} \langle \alpha_0 | \exp\left(-\hat{H} \frac{\beta}{M}\right) \prod_{i=1}^{M-1} \sum_{\alpha_i} \left[ |\alpha_i\rangle \langle \alpha_i| \exp\left(-\hat{H} \frac{\beta}{M}\right) \right] | \alpha_0 \rangle \\
&= \sum_{\{\alpha_i\}} \langle \alpha_0 | \hat{\rho}_{\Delta\beta} | \alpha_{M-1} \rangle \prod_{i=1}^{M-1} \langle \alpha_i | \hat{\rho}_{\Delta\beta} | \alpha_{i-1} \rangle \\
&\equiv Z_\beta \sum_{\{\alpha_i\}} \left[ P(\{\alpha_i\}, M)_\beta = \frac{1}{Z_\beta} \langle \alpha_0 | \hat{\rho}_{\Delta\beta} | \alpha_{M-1} \rangle \prod_{i=1}^{M-1} \langle \alpha_i | \hat{\rho}_{\Delta\beta} | \alpha_{i-1} \rangle \right]
\end{aligned}$$

This representation simulates the particles as hopping between connected nodes of a graph where the nodes are discrete electronic states (like atomic orbitals in a tight-binding model or Gaussian waves, or plane waves etc.).  $P$  is the path generator routine discussed further below.

To make some measurement on a system, we write down the average value for the observable  $\hat{O}$  as:

$$\langle \hat{O} \rangle = \frac{1}{Z_\beta} \sum_{\alpha} \langle \alpha | \hat{O} \hat{\rho}_\beta | \alpha \rangle = \frac{1}{Z_\beta} \sum_{\alpha, \alpha'} \langle \alpha | \hat{O} | \alpha' \rangle \langle \alpha' | \hat{\rho}_\beta | \alpha \rangle$$

In this case, the particles are moving through the graph from one point to another and then returning to its initial position via an observable. The average value is then a sum over all such paths normalized by the partition function. For a numerical method, however, such a mechanism is rather inefficient as the routine would sample many paths that would not contribute to the average. In order to remove this difficulty, the above average may be written as a sum over paths, or cycles, which loop back on themselves as in the calculation of the partition function.

$$\begin{aligned}
\langle \hat{O} \rangle &= \frac{1}{Z_\beta} \sum_{\alpha_0 \alpha'} O_{\alpha_0 \alpha'} \langle \alpha' | \hat{\rho}_{\Delta\beta} \prod_{i=1}^{M-1} [\langle \alpha_i | \langle \alpha_i | \hat{\rho}_{\Delta\beta} ] \alpha_0 \rangle \\
&= \sum_{\{\alpha_i\}} \frac{\sum_{\alpha'} O_{\alpha_0 \alpha'} \langle \alpha' | \hat{\rho}_{\Delta\beta} | \alpha_{M-1} \rangle \langle \alpha_0 | \hat{\rho}_{\Delta\beta} | \alpha_{M-1} \rangle \prod_{i=1}^{M-1} [\langle \alpha_i | \hat{\rho}_{\Delta\beta} | \alpha_{i-1} \rangle]}{Z_\beta \langle \alpha_0 | \hat{\rho}_{\Delta\beta} | \alpha_{M-1} \rangle} \\
&= \sum_{\{\alpha_i\}} \frac{\sum_{\alpha'} O_{\alpha_0 \alpha'} \hat{\rho}_{\alpha' \alpha_{M-1}}^{\Delta\beta}}{\hat{\rho}_{\alpha_0 \alpha_{M-1}}^{\Delta\beta}} P(\{\alpha_i\}, M)_\beta
\end{aligned}$$

The last expression can easily be fitted within a Monte Carlo routine with an existing path generator P.

The path generator P is responsible for choosing the histories (paths) of connected states (beads) in accordance with the Hamiltonian of the system. The system from which the paths are chosen is best represented by a weighted graph G with a set of "nodes"  $\{\alpha\}$  and "edges"  $\{Q_{\alpha,\gamma}\}$ . The nodes correspond to a convenient basis for the system, and the edges are equal to the expected value of the density operator between the two connected states.

$$\rho_{\alpha,\alpha'} = \langle \alpha | \hat{\rho}_{\Delta\beta} | \alpha' \rangle \equiv \delta_{\alpha,\alpha'} - \langle \alpha | \hat{H} | \alpha' \rangle \Delta\beta$$

If we consider two states  $\alpha$  and  $\gamma$  which are elements of our basis space, we can construct a set of N intermediate states  $\xi_{i=1,2,\dots,N}$  which are connected to both  $\alpha$  and  $\gamma$  with edge weights  $Q_{\alpha,\xi_i}$  and  $Q_{\gamma,\xi_i}$  respectively. We can then constructing a probability  $p_i = w_i / \sum w_i$  representing the chance of each intermediate state being visited in between states  $\alpha$  and  $\gamma$ . It is convenient to choose our weights  $w_i$  to be equal to the product of the two edge weights connecting the intermediate state to the two fixed states. We can then choose the intermediate state  $\xi_i$  with probability  $p_i$ . This way, in our Monte Carlo

algorithm, the transition probability between paths is unity and saves a rejection step in the algorithm. As in general our paths will have more than three beads, we can move multiple beads at one time by moving either the even or the odd beads and fixing the odd or even beads respectively.

If we consider a system of many particles, we may extend the above algorithm by keeping track of all the particles and summing over the many distinct paths and sign permutations of the paths. However, this would require an enormous amount of memory and processor time for any realistic system. On the other hand, so long as the basis spans  $\hat{H}$ , we may use any basis we like for our system. As a result, it would be more helpful to consider the collection of particles in a single many-particle state. The Fock space provides a convenient set of many-particle states that both relieves the algorithm of remembering which particles are in which states and of summing over the permutations of the paths. In this way, it is sufficient to know the population, one or zero for electrons (and an integer for bosons), of each single particle state in the system for each bead in our path.

However, it would be inconvenient to try and remember all of the different configurations [38] and the different transition weights between the Fock states. To relax this requirement we enforce a nearest-neighbor condition where only a single particle is moved at a time. This assumption is accurate in the limit of small time slices, requiring many beads along each path, but it allows us to find neighboring Fock states and the transition weights in run time.

To calculate the transition weight  $Q_{\alpha,\gamma}$  (from now on, we will use Greek indices to label many particle states and Roman indices for single particle states) we must in general calculate the determinant for electrons (or permanent for bosons) between the two states. However, because we are restricting our system to have only single particle moves, we

can ignore the requirement of calculating a determinant which requires  $N^3$  operations. This is again valid when the imaginary time slices are small. We are, in effect, keeping only the first order terms in the expansion in  $\delta\beta$ . As the sign of the determinant for Fermi statistics can be positive or negative, it is determined by counting the number of occupied states between the  $i^{\text{th}}$  and  $j^{\text{th}}$  states involved in the hopping [39].

We note that the above algorithm is similar in construction to a Lattice Regularized Diffusion Monte Carlo or Green Function Monte Carlo [40,41]. The primary difference between these latter methods and the this PSMC algorithm is that we are not relaxing just to the ground state, but rather we are exploring all paths in the graph of configuration states for our system and obtaining statistics for temperatures greater than zero.

### **Fixed node approximation(s)**

As a system becomes larger, the number of many-body states increases exponentially. As a result, a Monte Carlo analysis is advantageous, allowing for the system to scale up without having to sample all possible paths through the Fock space. At this point, it would be conceptually possible to apply the PSMC algorithm as described above, accounting for the signs of the sampled paths. However, for larger systems, this is not feasible as a result of the well-known Fermion sign problem that plagues many-Fermion quantum Monte Carlo algorithms. The anti-symmetry of the many-Fermion wavefunction under exchange leads to negative path amplitudes. As the ratio of positive to negative amplitude paths gets smaller, the number of samples needed to obtain accurate statistics increases. Unfortunately, this ratio approaches unity rather quickly as the number of particles increases and the temperature decreases. And in PIMC

calculations, ignoring the sign change simply corresponds transforming the Fermion problem into a bosonic problem. A more thorough discussion of this problem can be found in the literature [37,42].

To avoid this problem in continuous space, it is common to apply a fixed node approximation whereby a nodal surface is calculated for some related exactly solvable if approximate system, and no particle movement is allowed which crosses this surface [37,42]. In this way, points which are furthest away from the nodal surfaces have higher probability of being occupied, much as one would expect for a single particle bounded by a hard wall.

However, placing such a nodal surface on a lattice is not as clear, because the points are discretely placed and a metric of the space upon which to map a nodal surface is not always well defined. Instead, for a tight-binding scheme, the off-diagonal hopping energies between Fock states which would otherwise contribute a negative sign to the density matrix, are added to the diagonal elements while setting the negative off-diagonal element to zero [41]. This reduces the occupation probability of that state and, as a result, the paths avoid this state from which a nodal crossing could occur. Applying this approach to the quantum Monte Carlo algorithm produces an overestimate of the ground state energy of the system [41].

However, as the purpose of the approximation is to mimic the energy increase as a result of Pauli exclusion, much of this energy can be taken into account simply by not allowing the fermions to occupy the same state. By simply ignoring the sign change and allowing all other transitions to occur but with no sign change, we reduce the energy change associated with anti-symmetry. And, thus, this approach produces an underestimate of the ground-state energy of the system. Still, because we are not allowing same site occupation, the system is not bosonic as it would be for PIMC with this

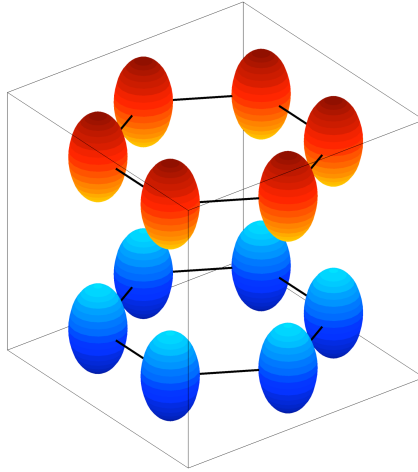


Figure 20: The trial system used for this study is comprised of two 6 atom single orbital rings layered with direct stacking of the atoms on opposite rings. The differing colors are used to enhance which is the top and which is bottom layer.

approach (because with a continuous space no two sampled particle positions would ever be the same), but rather something between the two limits.

For notational convenience, henceforth we will refer to these two variations of the FN approximation as Fixed Node Ceiling (FNC) and Fixed Node Floor (FNF). Together, the two FN approaches allow one to establish upper and lower bounds on exchange-correlation effects in a many-electron system.

### **TRIAL SYSTEM AND EXACT BEHAVIOR**

Our trial system is comprised of two 6 atom single-orbital rings layered with direct stacking of the atoms on opposite rings, with an interlayer atomic separation  $d$  and intralayer atomic separation of  $2.68 a_b = 1.42 \text{ \AA}$ . For our simulation, we used an intralayer bare hopping parameter  $\tau$  of 0.1 Hartree (Ha) = 2.7 eV between nearest

neighbor atoms on the same ring, and a small bare interlayer hopping potential  $\tau_z$  of 0.001 Ha between nearest neighbor sites on opposite layers. (We also allow for an interlayer potential difference of  $\Delta$  such as due to an externally applied electric field, but we do not use in calculations of this manuscript. The relative permittivity was set to 3.9 (that of SiO<sub>2</sub>) for specificity. To somewhat mimic the bilayer graphene system where the interlayer carrier separation is kept small compared to the intralayer carrier separation, in this trial system the interlayer atomic separation  $d$  is kept small compared to the intralayer atomic separation even though  $\tau$  is assumed large compared to  $\tau_z$ .

In applying our algorithm to the trial system of two atomic rings described in the introduction, we first begin by defining the Hamiltonian for the system as a sum of interlayer and intralayer contributions, where layers are defined in this case by plus (+) or minus (-) signs corresponding to the upper layer or lower layer, respectively,

$$\hat{H} = \hat{H}_{++} + \hat{H}_{--} + \hat{H}_{+-} + \hat{H}_{-+}$$

The intralayer contributions take the form,

$$\hat{H}_{\pm\pm} = \left( \pm \frac{\Delta}{2} + \varepsilon \right) \sum_i \hat{n}_{i,\pm} - \tau \sum_{\{i,j\}} \hat{a}_{i,\pm}^\dagger \hat{a}_{j,\pm} + \frac{1}{2} \cdot \frac{1}{4\pi\varepsilon_0} \sum_{i \neq j} \frac{1}{|\mathbf{R}_i - \mathbf{R}_j|} \hat{n}_{i,\pm} \hat{n}_{j,\pm}$$

and the interlayer contributions, the form,

$$\hat{H}_{\pm m} = -\tau_z \sum_{\{i,j\}} \hat{a}_{i,\pm}^\dagger \hat{a}_{j,m} + \frac{1}{2} \cdot \frac{1}{4\pi\varepsilon_0} \sum_{i,j} \frac{1}{|\mathbf{R}_i - \mathbf{R}_j + d|} \hat{n}_{i,\pm} \hat{n}_{j,m}$$

defined through a tight-binding picture with nearest neighbor contributions, where the typical raising and lowering operators  $\hat{a}^\dagger$  and  $\hat{a}$  are used and the atomic center positions are notated by vectors  $\mathbf{R}_i$ , and the state population operator is denoted by  $n$ . The first term in the intra-layer contribution is the potential energy, the second term and the first term in the interlayer contribution corresponds to the kinetic energy and the last term corresponds to an approximate electron-electron Coulomb interaction. Absent from this trial Hamiltonian is the allowance of a spin degree of freedom and, as a result, any anti-ferromagnetic coupling and Hubbard interactions between the electrons. However, the PSMC algorithm is not dependent on these approximations. These terms were left out here because the addition of a spin contribution would greatly increase the number of Fock states making the system impractical to solve exactly.

By following the construction of the Path-Sum algorithm as outlined above (but not yet performing Monte Carlo calculations) we can build a exact simulator to measure the average energy, density-density correlation function, and interlayer energy matrix element using the following observables:

$$\begin{aligned}\langle \hat{H} \rangle_\beta &= \frac{1}{Z_\beta} \sum_{\{\alpha_i\}} \langle \alpha_0 | \hat{H} | \alpha_M \rangle \prod_{i=1}^M \langle \alpha_i | \hat{\rho}_{\Delta\beta} | \alpha_{i-1} \rangle \\ \langle \hat{n}_j \hat{n}_k \rangle_\beta &= \frac{1}{Z_\beta} \sum_{\{\alpha_i\}} \langle \alpha_0 | \hat{n}_j \hat{n}_k | \alpha_M \rangle \prod_{i=1}^M \langle \alpha_i | \hat{\rho}_{\Delta\beta} | \alpha_{i-1} \rangle \\ \langle \hat{H}_{inter} \rangle &= \frac{1}{Z_\beta} \sum_{\{\alpha_i\}} \langle \alpha_0 | \sum_i \hat{a}_{i,\pm}^\dagger \hat{a}_{i,m} | \alpha_M \rangle \prod_{i=1}^M \langle \alpha_i | \hat{\rho}_{\Delta\beta} | \alpha_{i-1} \rangle\end{aligned}$$

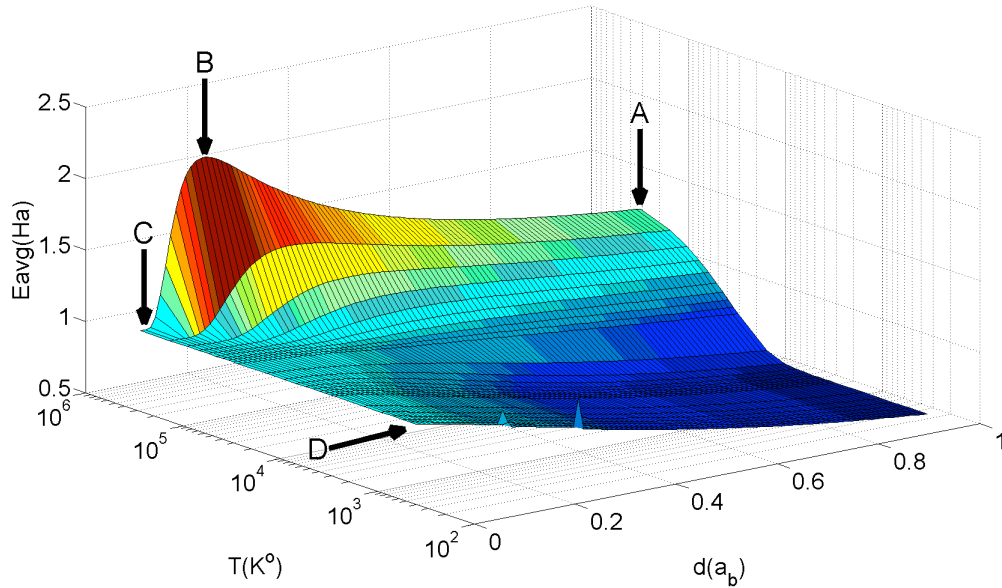


Figure 21: Expected total energy for two 6 (carbon) atom rings separated by distance  $d$  at a temperature,  $T$ . The drop in energy at high temperatures from large to small interlayer separation corresponds to the formation of excitons. At lower temperatures the excitons are formed at even great separation distances, though not necessarily correlated.

Because the system is so small, only 924 possible many-body states, it is computationally reasonable to diagonalize the many-body Hamiltonian and calculate the observables exactly for various temperatures and interlayer separations, as per the total energy calculation of Figure 21. For a fixed high temperature, as the layers are moved closer together from Point A to Point B, there is an increase in average energy as a result of strengthening inter-layer Coulomb interactions between electrons. (If we add in a fixed  $+e/2$  charge per atom to maintain charge neutrality, the total energy increase disappears as the layers are brought closer together, but this only amounts to a  $d$ -dependent, but otherwise fixed, potential shift.) However, moving from Point B to Point C, excitons form reducing the energy of the system. Moving from Point C to Point D, the

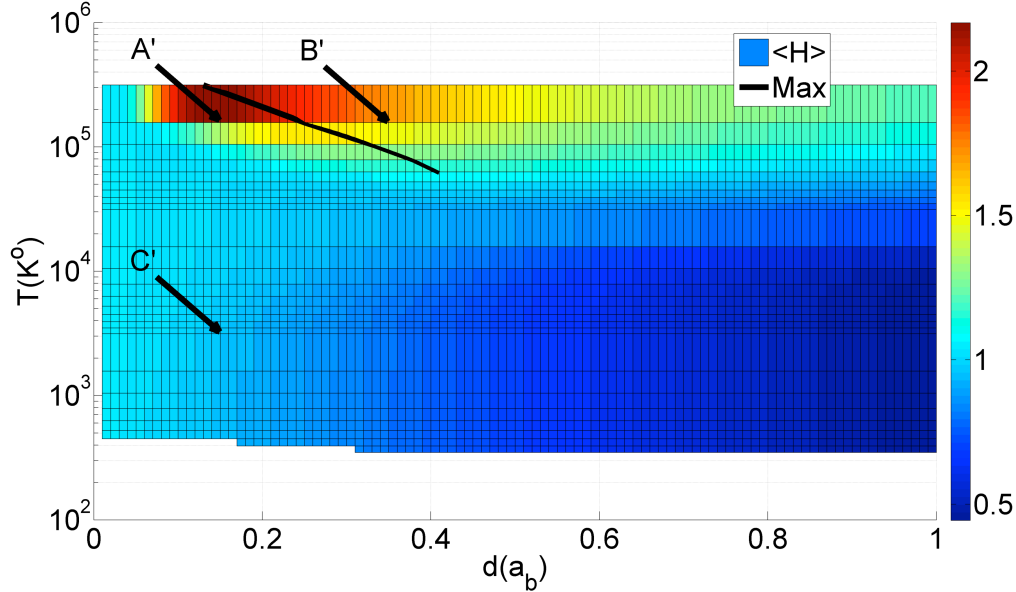


Figure 22: Top-down view of the total energy of system. The black solid line maps the maximum of the average energy noting a transition where excitons begin to form. Noted in the plot are points A', B' and C' noting the positions where the density-density correlation function was measured.

Coulomb interaction energy remains fixed for the well formed excitons, but the energy of the system as a whole is reduced as the system relaxes toward the ground state at low temperatures. Moving diagonally from point D to A, the excitons fall back apart.

This interpretation is supported by observing the change in the density-density correlation function at various critical points on the average energy surface plot. Figure 21 shows density-density correlation functions both within a single layer and between the layers at the points labeled A', B' and C' in Figure 22. Point A' and Point B' are to the left and right, respectively, of the black solid line in Figure 22 which maps the maximum of the energy and, thus, the approximate boundary beyond which excitons begin to form to the left and below. At point B' the electrons and holes (electron vacancies) on opposite layers are relatively uncorrelated to one another, as exhibited by the probability of finding

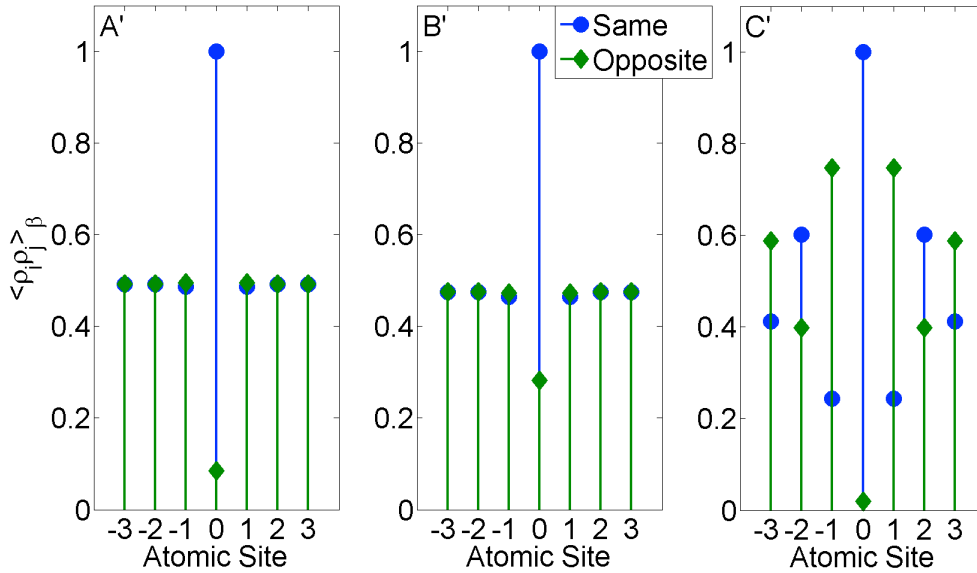


Figure 23: Density-density correlation function of electrons in same and opposite layers of the bilayer system. At high temperature large separation Point B' (middle) there is little correlation in electron positions among the sites within the same layer and limited correlation between layers. But as the separation between layers is decreased to Point A' (left), the (anti-) correlation between electron position between layers increases substantially, indicating the formation of an exciton. At point C' with the same interlayer separation as in A' but lower temperature, still stronger interlayer correlation and now strong intralayer correlation is observed.

the site below an electron on the top layer filled on the bottom layer. However, at Point A', Coulomb repulsion largely evacuates the point below the occupied electron site in the top layer producing an electron-hole pair. At Point C' at lower temperature but same layer separation as A', the electrons and holes in opposite layers are even more strongly correlated, and a substantial correlation in electron and hole positions (anti-correlation of electron positions) between nearest neighbor sites has also been induced.

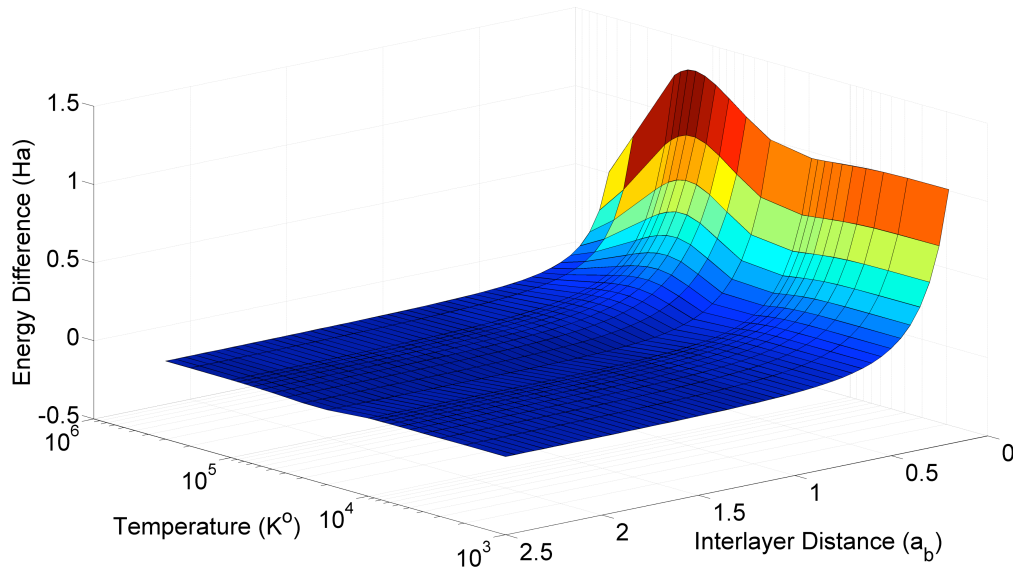


Figure 24: Magnitude of the energy difference between the semi-isolated system and the exact system at a range of interlayer distances and temperatures. The sharp increase in difference between the expected energies is a representation of the effect of interlayer exchange-correlation energies within the system.

The effect that the, specifically, interlayer exchange-correlation has on the system through interlayer Coulomb interactions can be measured by comparing the exact results to those obtained by assuming no interlayer exchange-correlation. For the latter, we start with the expected energy of the system without any interlayer Coulomb interactions, which gives us the expected energy of the two semi-isolated systems with only the addition of only the small bare tunneling parameter. We then add the average interlayer Coulomb interactions that would otherwise arise if there were no correlation among the electron positions between layers. In the end, we obtain the difference shown in Figure 24 indicating the (negative of the) exchange-correlation energy that comes with exciton formation.

The exchange portion of the interlayer exchange-correlation interaction requires interlayer coherence [39]. As a measure of the interlayer coherence, we calculate the expectation value  $\left\langle \tau_z \sum_i \hat{a}_{i,\pm}^\dagger \hat{a}_{i,m} \right\rangle_\beta$  for the hopping energy matrix element between the layers. Figure 25 shows the calculated difference between the expected hopping matrix elements energies between layers for systems with and without interlayer Coulomb interactions with a fixed small bare tunneling term, although we note that the latter are quite small on the energy scale shown. We see that at large distances there is little evidence of increased interlayer coherence relative to that due to the bare interlayer coupling alone. However, optimally within an intermediate temperature range except at very small separations, as the interlayer distance is reduced the wave functions of the two layers are increasingly locked in relative phase with one another. On the other hand, outside of this region of strong interlayer correlation, we can conclude that the interlayer exchange-correlation effects are actually primarily just correlation effects.

The shape of the results in Figure 25 are qualitatively as to be expected for half-filling of the two-ring system. To understand these results consider the equilibrium mean-field Fock exchange interaction obtained from the quasi-single particle states  $\varphi_{i,\mathbf{k}}$ :

$$V_F(\mathbf{R}_+, \mathbf{R}_-) = \frac{-e^2}{4\pi\epsilon_0\epsilon_r \sqrt{|\mathbf{R}_+ - \mathbf{R}_-|^2 + d^2}} \sum_{i,\mathbf{k}} n_{i,\mathbf{k}} \varphi_{i,\mathbf{k}}(\mathbf{R}_+) \varphi_{i,\mathbf{k}}^*(\mathbf{R}_-).$$

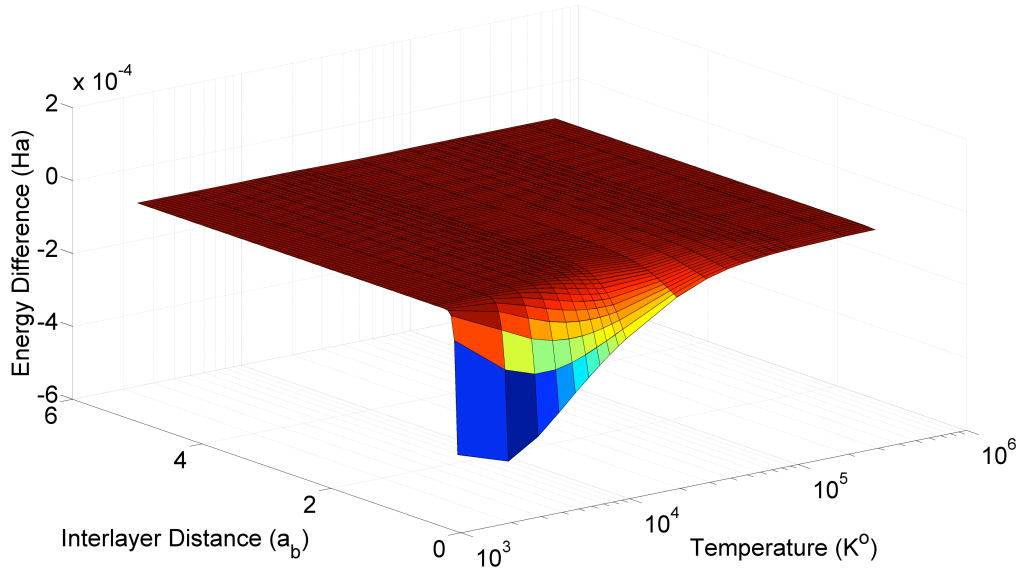


Figure 25: Average interlayer hopping energy matrix element difference between systems with and without interlayer Coulomb interactions. At higher temperatures or large distances, the interlayer coherence of the wavefunctions is reduced and interlayer Coulomb interactions have little effect on the interlayer hopping potential matrix elements. However, at optimally intermediate temperatures and small interlayer distance, there is a substantial growth in the interlayer hopping potential matrix element. These results provides a measure of the coherence between the layers and evidence for a condensate in this trial system.

where  $n_{i,k}$  are the occupancy factors. Excluding the Coulomb interactions and without interlayer coupling, there are six single-particle energy states in each layer with energies  $(-0.2 \text{ Ha})\cos(l\pi/3)$ ,  $l = -2, -1, 0, 1, 2, 3$ . As (negative) coupling  $-\tau_z$  is added between the two layers, the 6 pairs quasi-particle states will couple forming a lower energy symmetric and higher energy anti-symmetric state separated in energy by  $2\tau_z$ . These energies, of course, are then self-consistently altered via the Hartree-Fock potential. At very high energies all quasi-particle states are equally occupied and the contributions from the symmetric and asymmetric states cancel as expected. On the other hand, for all but very

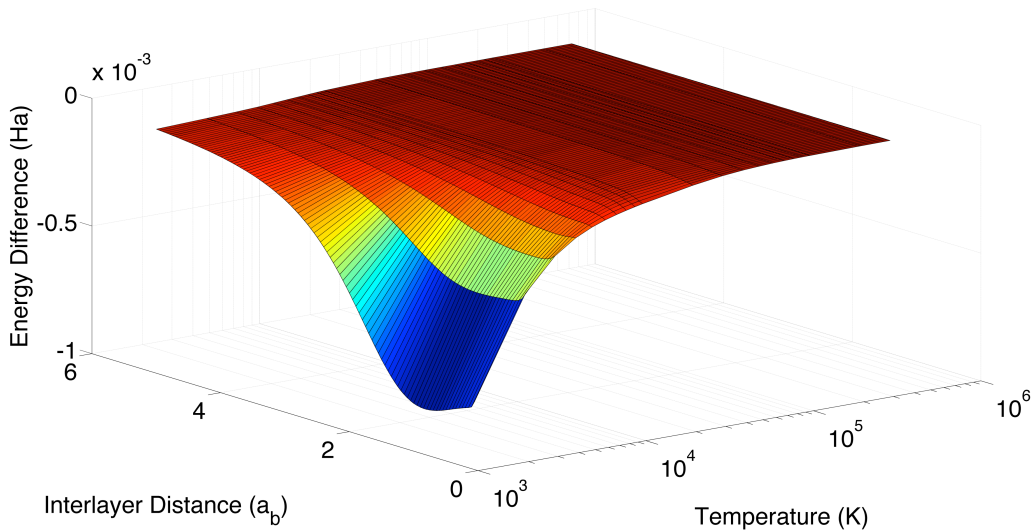


Figure 26: Average hopping energy matrix element between top and bottom layers for the system with 4 electrons. With 4 electrons populating the two rings, the Fermi energy is set between the symmetric and anti-symmetric states that result from interlayer coupling of otherwise degenerate states. This produces an overall enhanced exchange interaction by comparison to the results of Figure 6, and one peaking at zero temperature.

strong energy splitting due to the self-consistent interlayer coupling, as the temperature approaches zero, both the symmetric and antisymmetric states will be filled up through the  $l=1$  state pairs, with the Fermi level located between the  $l=1$  and  $l=2$  state pairs, and again the Fock exchange term will vanish. Therefore, only at intermediate temperatures or when the (self-consistent) interlayer splitting is larger than the nominal intra-layer state separation between the  $l=1$  and  $l=2$  states, will the lower energy symmetric states have higher occupancy and, thus, will there be a nonzero interlayer coherence and exchange interaction, consistent with the results of Figure 25 for the true many-body calculation.

By the same logic, however, a stronger overall exchange interaction would be expected if we consider only four electrons. E.g., in the absence of interlayer coupling, at

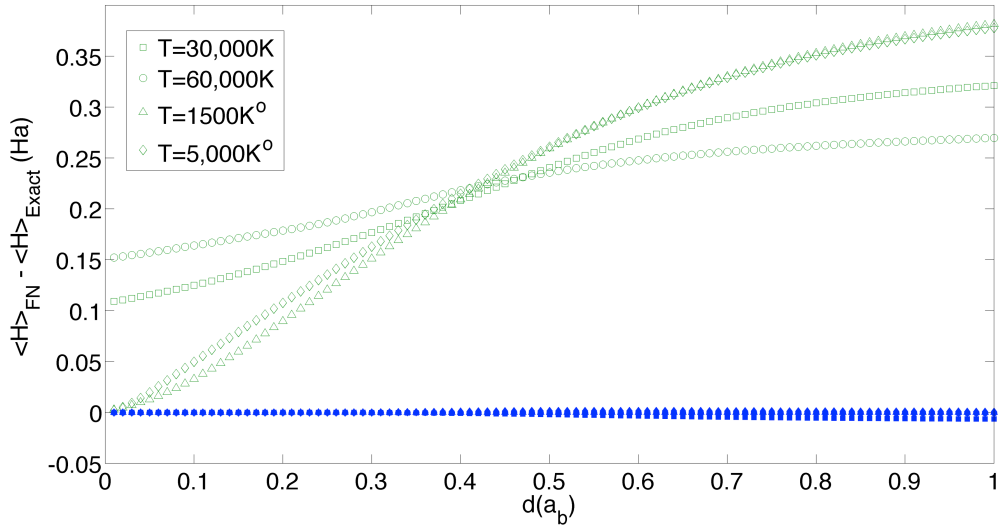


Figure 27: Error in average energy for both fixed node approximations at various temperatures. Open symbols represent the ceiling fixed node and the filled symbols the floor fixed node. The type of shape represents the temperature. The floor fixed node shows an energy minimum, whereas the ceiling represents a maximum to the average energy of the system.

0K temperature, the  $l=1$  states will be half-filled with the Fermi level lying at the energy of these states. When the layers are coupled, only the lowest energy symmetric  $l=1$  states will be filled with the Fermi level falling between the symmetric and anti-symmetric states, producing a non-zero expected coherence and associated exchange interaction between the layers at 0K in contrast to the results for the 6 electron half-filled system. The expected overall enhanced interlayer correlation is confirmed by the calculated exact results for this latter four electron system in Figure 26. By comparison to the results of Figure 25, the peak correlation is over 2 times greater, and the correlation remains strong over a much larger parameter space.

We wish to emphasize that the more limited interlayer correlation of Figure 25 is an artifact of the large intra-layer state splitting resulting from considering small rings.

For larger rings where the interlayer splitting exceeds the intra-layer splitting, a strong OK exchange interaction should be recovered, and even optimized, for the half-filled condition.

We note that it is also possible to extend the otherwise exact calculations solutions for this system to include the two fixed node approximations, FNC and FNF, to illustrate the bounding of the exact solution. Figure 27 shows the exact expected energy along with expected energy obtained from the exact evaluation of the FNC and FNF approximations. As required, the FNC result is equal or greater than the exact result, while FNF results is less than or equal to exact result. On the scale of energies considered—at these atomic separations, the Coulomb energy between two electrons in nearest neighbor atoms on the same layer and on adjacent layers at a separation  $d$  are  $\sim 0.1$  Ha and  $\sim 0.25/d$  Ha, respectively—the error in either case is relatively small. In these simulations, the FNF approach is clearly relatively much more accurate than the FNC approach. However, that is no guarantee of similar results for other systems or enumerations of the single particle states [43].

#### **COMPARISON OF EXACT AND FN-PSMC RESULTS**

It is impractical to consider the entire parameter space addressed above with the FN-PSMC approach. Rather, for the latter we consider points which represent limiting conditions from the parameter space above. Figure 28 shows FN-PIMC results for the density-density correlation functions for point A' in Figure 22, along with the exact solutions for comparison. Good accuracy is obtained with either the FNC-PSMC or FNF-PSMC approach, where again the FNF approach provides somewhat the more accurate of the

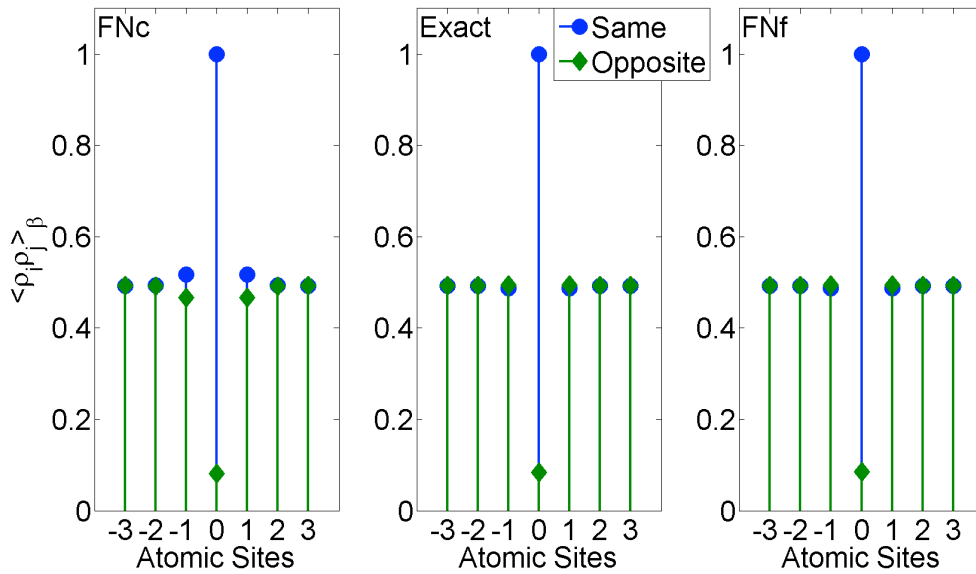


Figure 28: Density density correlation functions for point A' in the interlayer distance-temperature phase space comparing the PSMC implementations of the two FN approximations, FNC and FNF with the exact calculation. Both fixed node approximations provide reasonable accuracy for estimating the correlation between the layers.

two. Table 2 exhibits the average energy values for two points in the parameter space with 6 and 4 electrons, corresponding to Points (4,186K,  $0.1a_b$ ) and (101,286K,  $1.0a_b$ ) in Figure 21. The results exhibit both good accuracy of the bounding FN approximations, and the effectiveness of the FN-PSMC method of being able to reproduce these upper and lower energy limits. To show that the phase transitions in the interlayer coherence shown in Figures 25 and 26 may be obtained from the PSMC approach, in Table 4 we provide expected hopping energy differences as described above for two critical points for both the 6 and 4 electron systems. Considered in whole, this agreement suggests that the FN-PSMC approach can be used to accurately track phase transitions in many-body systems due to exchange-correlation effects.

Table 3: Exact and FN-PSMC calculation of the average energy of the system, with the exact evaluations of the FN approximations shown for reference in parentheses.

Electron Population	Temperature (K)	Interlayer separation d (ab)	Exact solution (Ha)	FNC-PSMC (FNC exact eval.) (Ha)	FNF-PSMC (FNF, exact eval.) (Ha)
4	4,186	0.1	$4.314 \times 10^{-2}$	$8.121 \times 10^{-2}$ ( $7.306 \times 10^{-2}$ )	$4.725 \times 10^{-2}$ ( $3.580 \times 10^{-2}$ )
4	101,283	1.0	0.3056	0.4304 (0.4306)	0.3053 (0.3055)
6	4,186	0.1	0.9995	1.0398 (1.0375)	1.011 (0.9987)
6	101,283	1.0	1.040	1.292 (1.293)	1.039 (1.040)

Table 4: Exact and FN-PSMC calculation of expected interlayer matrix elements, with the exact evaluations of the FN approximations shown for reference in parentheses.

Electron Population	Temperature (K)	Interlayer separation d (ab)	Exact solution (Ha)	FNC-PSMC (FNC exact eval.) (Ha)	FNF-PSMC (FNF, exact eval.) (Ha)
4	4,186	0.1	$-1.82 \times 10^{-4}$	$-2.94 \times 10^{-5}$ ( $-2.97 \times 10^{-5}$ )	$-5.42 \times 10^{-4}$ ( $-5.68 \times 10^{-4}$ )
4	101,283	4.0	$-8.60 \times 10^{-6}$	$-4.34 \times 10^{-6}$ ( $-4.34 \times 10^{-6}$ )	$-9.12 \times 10^{-6}$ ( $-9.13 \times 10^{-6}$ )
6	4,186	0.1	$-2.13 \times 10^{-4}$	$-6.68 \times 10^{-5}$ ( $-5.70 \times 10^{-5}$ )	$-9.06 \times 10^{-4}$ ( $-7.15 \times 10^{-4}$ )
6	101,283	4.0	$-9.58 \times 10^{-6}$	$-4.99 \times 10^{-6}$ ( $-4.97 \times 10^{-6}$ )	$-10.3 \times 10^{-6}$ ( $-10.3 \times 10^{-6}$ )

## CONCLUSION

We have presented a path-sum Monte Carlo method, a tight-binding approach to Path Integral Monte Carlo, as an alternative to mean-field theory for analyzing exchange-correlation effects in many-electrons systems. To test the algorithm we applied it to a small trial system of either four or six electrons confined to two parallel six single-orbital-atom rings (12 atoms and orbitals total) for which exact results are available for comparison. We observed the phase transition for exciton formation with interlayer separation and temperature, showing good agreement between the Monte Carlo and exact calculations. Moreover, although the Monte Carlo algorithm employs a fixed node approximation to avoid the Fermion sign problem and, therefore, is inexact, we considered two different limits to the fixed node approximation which provide upper and lower bounds on the total energy. While a simple system was considered here to allow the comparison with exact results, the FN-PSMC algorithm should extend the reach of computational analysis to much larger many-electrons systems such as, e.g., paired graphene layers for which room-temperature superfluidity has been predicted elsewhere.

## Chapter 5. Conclusion

### COMMENTS

The demand for smaller and faster switches has necessitated improved understanding and modeling capabilities at the nanoscale limit. In addition, the coming potential paradigm shift in the transistor technology has increased the demand for reliable software to design and predict the operation of the next generation of solid-state devices. In this dissertation, I have presented semiclassical Monte Carlo and quantum path sum Monte Carlo methods which will fulfill those needs.

In Chapter 2, I described my development and implementation of a SCMC algorithm to compare a set of III-V materials with Si in a short channel tri-gate nanowire transistor. Silicon has been the material of choice for CMOS technology for several decades, while the III-V materials have been ‘stuck in the future.’ With the continuing progression of Moore’s law, the channel length of the MOSFET has become ever shorter. I showed that at channel lengths of approximately 10 nm, scattering within the channel is not important for III-Vs, making the mobility advantage of the III-V materials less important. However, because the III-V’s retain their advantage in terms of the effective mass of the electron over Si and scattering remains significant in Si, they exhibit higher currents as a result of higher drift velocities in the channel, despite a reduction in carrier density from quantum confinement. I also showed that for such restricted geometries, as demonstrated in the models used here, further corrections to scattering due to quantum confinement and tunneling must be included.

My application of the SCMC algorithm to graphene FETs (GFETs) was presented in Chapter 3. Graphene shows potential to be a very important material for future devices

as a result of its ultra-high mobility. However, as a result of its bandstructure and strong Zener tunneling, including unity probability for Klein tunneling (for normal incidence) in the zero bandgap limit, a FET made from a single layer of graphene does not turn off well. To take advantage of the material's unique electrical properties and design a workable device, an accurate model must be produced that captures these attributes of graphene. The SCMC algorithm was calibrated to experimentally obtained velocity field curves, and then applied to the GFET with the addition of Zener tunneling and stochastic placement of remote charged impurities in the oxide layers. The simulator was able to accurately capture the attributes (both positive and negative) of the device under these constraints.

After exploring the Semiclassical limit in Chapters 2 and 3, the Path Sum Monte Carlo algorithm was presented in Chapter 4. The material graphene has another unique physical property when layered but separated by some dielectric; that is, under an applied interlayer potential, it may form a quantum mechanical condensate of excitons. To understand the formation of the condensate, a quantum many-body treatment must be used. Specifically, to further the understanding of the effects of exchange-correlation on such systems, I designed and implemented a tight-binding path-sum Monte Carlo derivative of the path-integral Monte Carlo formalism. To demonstrate the effectiveness of the method I applied it to two layered 6-atom rings. Using this model, I demonstrate that using a fixed-node algorithm, it is possible to place both lower and upper bounds on the phase diagram for creating a condensate in the system. We give evidence for coherent condensate formation by examining the expected value for the interlayer hopping matrix element, showing good accuracy for a phase transition using this fixed-node approximated Path Sum Monte Carlo algorithm.

In summary, with the progression of Moore's law and associated shrinking of devices and the reliance on new material and device physics, new simulators must be designed which can capture a wide range of physics. To that end, I have developed and demonstrate new SCMC and the PSMC algorithms for use in their respective regimes; the ensemble SCMC in the quantum-corrected semiclassical regime with novel materials and the PSMC in the many-body quantum regime. I have shown that they can be used effectively and efficiently in modeling the next generation of devices.

## **FUTURE RESEARCH**

Although the two methods can be used effectively to model the semiclassical and quantum limits, there are several points of further research that can be performed to improve upon the methods. Here I discuss the two methods separately with suggestions for improvement.

### **SCMC Improvements**

In Chapter 2, the SCMC was applied to nanometer scale MOSFETs. A major component of the study was the effects of quantum confinement on the carrier concentration in the channel of the device. It was found that there was little effect on the carrier concentration as the device was primarily controlled by the gate bias. However, a major assumption made was the absence of tunneling either through the gate or longitudinally along the channel. To account for the gate tunneling, an injection current can be included by calculating the transmission current across the gate along the surface of the gate region at each time-step. To account for the longitudinal tunneling through the channel, a better quantum correction needs to be included which would provide,

along with better accuracy in short channel devices, the possibility for devices with a more quantum flavor,

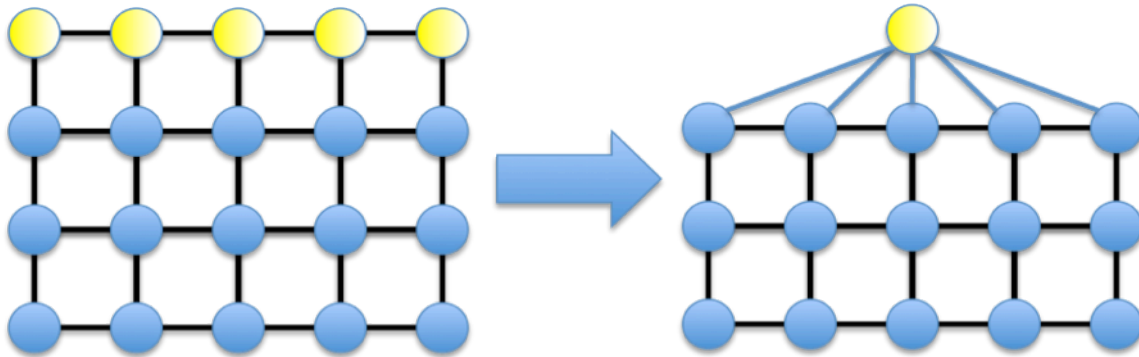


Figure 29: In the Poisson solver, the contact is copied onto many grid points which are connected to grid points in the device as in the left. However, as the potential on these points is constant and never changes, the contact may be condensed into a single node, as on the right, from which the relevant points may be connected.

like a tunneling field effect device. Corrections for quantum-confinement enhanced scattering rates should also be possible. In regards to the graphene devices discussed in Chapter 3, the next step in research for the FETs is to add a second graphene layer with or without a dielectric between them to investigate the performance of bilayer FETs and tunnel FETs, respectively. To do this, a separate member of the material class must be constructed to account for both the bandstructure differences from a single layer of graphene and also the possibility for tunneling between the layers.

In general, improvements to the Poisson solver can be made to make it both more efficient and more generally applicable. As it stands, the method uses only a fixed grid with fixed spacing, which limits the size and accuracy for the devices considered. By inserting a variable grid spacing mesh, fewer grid-points could be used which greatly

reduces the time for a solution. In addition, many of the potential grid points can be condensed into a single node from which the other grid points may be referenced; this scheme is illustrated in Figure 29.

For very high-frequency applications or optoelectronic devices, the Semiclassical Monte Carlo algorithm would need to be linked with an efficient Finite Difference Time Domain electro-magnetics solver. There are many commercial and free applications that can be linked to the SCMC algorithm for a multi-physics application and would provide a new research vector and broaden the applicability of the algorithm.

A major subject of research is how to treat the contacts of the devices and injection. In the current algorithm, a thin layer normal to the contact in the semiconductor region is required to be charge neutral. So, to inject charge into a contact, a positive, or negative charge in the case of hole injection, must be close enough to the contact to cause a charge imbalance. For very large source and drain regions with high doping densities, this is not a problem, however, in the case of sparsely placed dopants or small contact regions, the contacts are starved of carriers and the device is then source/drain resistance limited. As a result, a better treatment of the contacts is needed.

### **PSMC Improvements**

In Chapter 4 I presented the Path Sum Monte Carlo (PSMC) algorithm in application to a small exactly solvable system of 12 atoms arranged in two layered 6 atom rings as in Figure 20. Given that effectiveness of the algorithm in determining the phase transition in such a small structure, the next extension to the work is to try a much larger physical system with, in addition, a spin degree of freedom. For a 20x20 nm square flake of bilayer graphene with a spin degree of freedom, there are 61,288 single

particle states. This system at half-filling is much too large to perform the calculation either exactly or on a single core processor using the PSMC algorithm. As a result, it is necessary for the PSMC algorithm applied to such a system to be parallelized and distributed over several cores.

There are also several instances within the algorithm itself that have opportunity for improvement. For instance, in choosing the new states associated with the beads in the path, the intersection between the sets of states connected to the forward and backward states is found. A state from this set is randomly chosen to be the new state for the moving bead. For very large systems with many nearest neighbors, this algorithm is rather inefficient. Instead, it would be advantageous to find a covering probability density from which to choose the next state, sacrificing the unity acceptance probability, but gaining in speed.

The simulation time required per iteration for this algorithm scales linearly with the number of single particle states, particles, and time slices. However, it is unknown how the algorithm will scale in terms of number of iterations needed for convergence with changes in any of these quantities. Before considering large systems, considering first a smaller system followed by a series of progressively larger systems to understand the effects of scaling on convergence is advisable.

The algorithm described in Chapter 4 is constructed using the canonical partition function and is pictured as a system of a fixed number of particles connected weakly to a heat bath, as in Figure 30. If we allow, instead, for there to be an exchange of particles between the bath and the system as in Figure 31, the statistics are then described well by the grand canonical partition function, and a Path Sum can be constructed from this picture. This construction can then be used as a starting block for transport simulations.

For instance, a quantum point contact might be constructed from the illustration given in Figure 32.

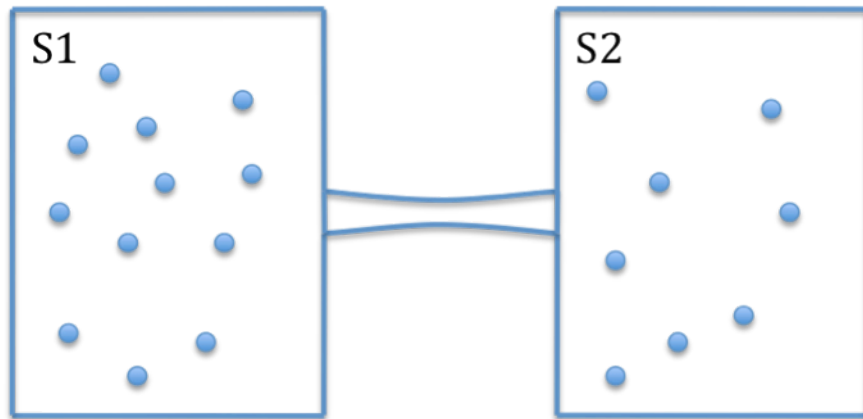


Figure 30: The canonical partition function used in the construction of the Path Sum in Chapter 4, can be pictured as a system S1 weakly coupled to a heat bath S2 with a constant number of particles in the system.

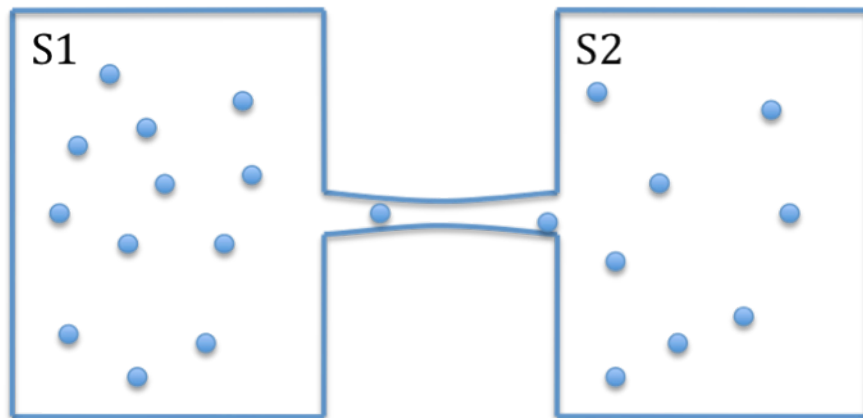


Figure 31: The grand canonical partition function can be pictured as a system S1 weakly coupled to a heat bath S2 and allowing particle exchange between the reservoirs.

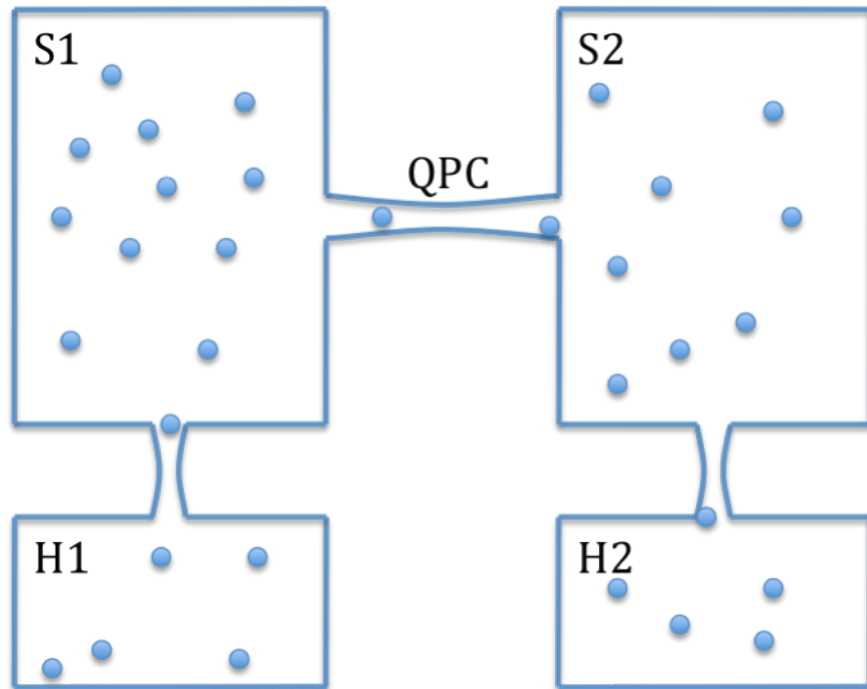


Figure 32: For a Quantum Point Contact QPC, two contact regions S1 and S2 are weakly connected to each other and also to two heat bath reservoirs H1 and H2 with different chemical potentials. In this way, transport measurements may be performed.

## Appendices

### APPENDIX A: FIXED NODE PATH SUM MONTE CARLO ALGORITHM

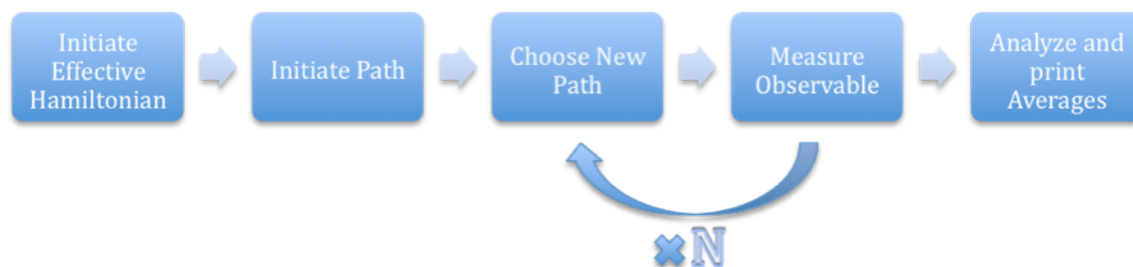


Figure 33: General flow of PSMC algorithm. The “Choose New Path” and “Measure Observable” steps are repeated ‘N’ times or until convergence of observable is reached.

#### Program Flow

The PSMC algorithm consists of 5 blocks that are run sequentially as illustrated in Figure 33. After initiating the Effective Hamiltonian and Path for the system, a new path is chosen and an observable, such as the average energy, is measured. The sequence of choosing a new path and measuring the observable for the new path is repeated N times or until convergence is reached for the observable. Finally, the observable averages are analyzed and printed for the user.

In Chapter 4, the mathematical background to the FN-PSMC method was given with a brief description of the computational implementation. This section is devoted to the construction and usage of the method with attention to the construction of the effective Hamiltonian, choosing new paths, and measuring an average observable quantity.

## **Initiating the Effective Hamiltonian and the Density Matrix**

The purpose of this step is to allow the algorithm to obtain the probability for hopping between different states of the system to choose new paths. This problem is at its basis, a problem of defining the Hamiltonian of the system and adjusting it by an identity matrix. When initiating the effective Hamiltonian for the system being modeled by the PSMC, the basis used for the system must be defined. In general, the specific basis does not matter but must span the Hamiltonian for the system and be orthonormal. After the basis is defined, the hopping energies between neighboring states must be evaluated for the Hamiltonian. The hopping energies are then stored in an adjacency matrix and the elements are accessed in run time.

Often the adjacency of the states follows a few simple rules as is the case in a lattice of sites. For instance, for a ring of  $N$  states enumerated from 0 to  $N-1$  with nearest neighbor hopping, the nearest neighbors of site 'i' are evaluated by  $(i+1+N)\%N$  and  $(i-1+N)\%N$ , where '%' is the modulus operator in C++. Such rules are very helpful in finding and evaluating the hopping energies for the nearest neighbors of a particular state in the basis for very large systems when the adjacency matrix is constrained by memory. Often the rules can be placed in a function that can be accessed at any time in the algorithm.

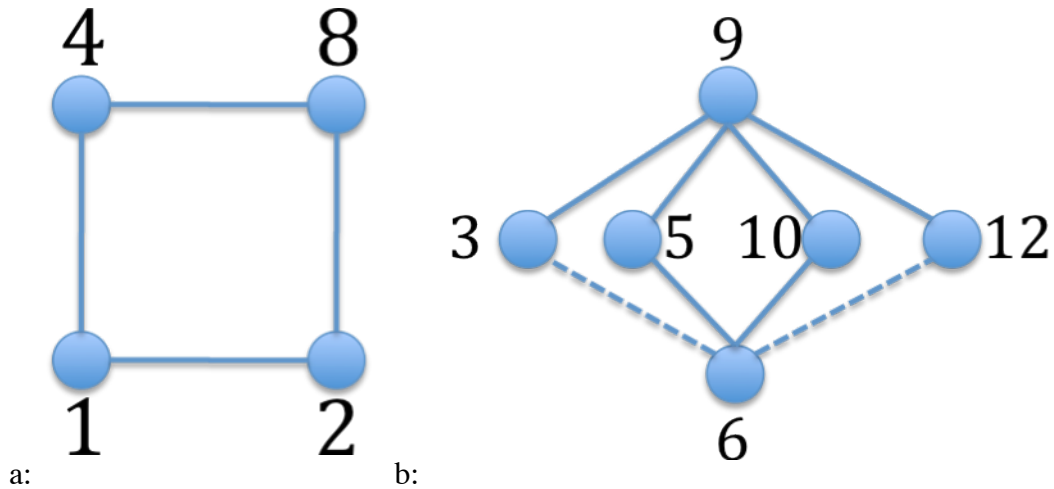


Figure 34: Graphs for populating a 4-site model with a: 1 electron and b: 2 electrons. The nodes on the graphs are indexed by the integer value of the binary translation of the Fock state. i.e.  $1=0001$ ,  $2=0010$ ,  $3=0011$ ,  $4=0100$ ,  $5=0101$ , etc. The solid edges represent the hopping elements with negative energies, while the dashed lines represent positive energy hops as a result of exchange.

In the case of the single particle Hamiltonian, the hopping energies are typically defined as negative numbers. However, in the case of the many-particle Hamiltonian, the hopping energies between different Fock space elements are positive or negative numbers as a result of exchange between the fermions of the system. This is the crux of the Fermion sign problem and is avoided by utilizing a fixed node approximated effective Hamiltonian as described in Chapter 4. To implement the approximation in the effective Hamiltonian it is necessary to find all neighboring state transitions from some initial state where a sign flip occurs and then adjust the elements of the Hamiltonian according to the approximation defined in Chapter 4.

The example used in Appendix C is a 4-site ring with up and down spins and 2 electrons populating the up spin states and 2 in the bottom. Here we will focus on a

single spin system to illustrate how to initiate the Hamiltonian. We have chosen for the system a four-site model with nearest neighbor hopping  $\tau$  whose graph is illustrated in Figure 34a. Filling the four sites with two electrons expands the available Fock states from 4 to 6 and the resultant graph for the 6 two-electron states is shown in Figure 34b. The exact Hamiltonian is a 6-by-6 matrix with positive and negative elements.

$$\hat{H} = \begin{bmatrix} 0 & 0 & \tau & -\tau & 0 & 0 \\ 0 & 0 & -\tau & -\tau & 0 & 0 \\ \tau & -\tau & 0 & 0 & -\tau & \tau \\ -\tau & -\tau & 0 & 0 & -\tau & -\tau \\ 0 & 0 & -\tau & -\tau & 0 & 0 \\ 0 & 0 & \tau & -\tau & 0 & 0 \end{bmatrix}$$

To construct the effective floor fixed node Hamiltonian  $\hat{H}_{FNF}$ , we simply take the negative absolute value of the exact Hamiltonian to ensure that all hopping energies are negative. For the ceiling fixed node Hamiltonian  $\hat{H}_{FNC}$ , the diagonal element of a state is the sum of all positive hopping energies from that state, while the specific sign flip hopping elements are set to zero. In the context of the graph for the ceiling fixed node, the edges which have a sign flip associated with the transition between states are cut and the remaining segments are wrapped onto the individual connected states. This construction is illustrated in Figure 35. Finally, the effective Hamiltonians for the two fixed node limits are:

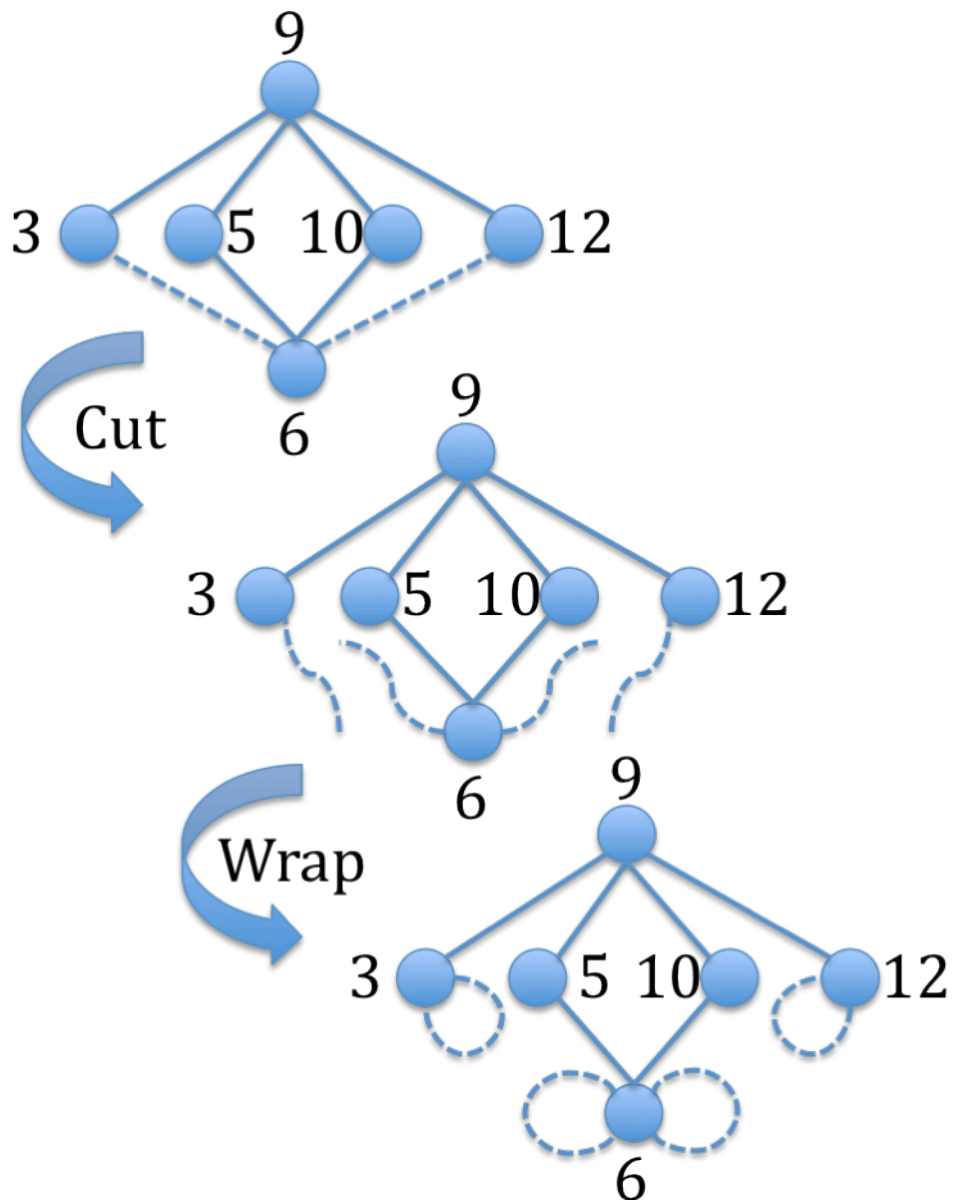


Figure 35: Operations on the graphs for representing the 2-particle Hamiltonian for a 4-site square model. Starting from the exact graph at the top, the dashed lines, representing sign flips in the transition between Fock states, are cut as in the second graph down. Finally, the dangling edges are wrapped onto the connected sites representing diagonal elements in effective Hamiltonian.

$$\hat{H}_{FNF} = \begin{bmatrix} 0 & 0 & -\tau & -\tau & 0 & 0 \\ 0 & 0 & -\tau & -\tau & 0 & 0 \\ -\tau & -\tau & 0 & 0 & -\tau & -\tau \\ -\tau & -\tau & 0 & 0 & -\tau & -\tau \\ 0 & 0 & -\tau & -\tau & 0 & 0 \\ 0 & 0 & -\tau & -\tau & 0 & 0 \end{bmatrix} \quad \hat{H}_{FNC} = \begin{bmatrix} \tau & 0 & 0 & -\tau & 0 & 0 \\ 0 & 0 & -\tau & -\tau & 0 & 0 \\ 0 & -\tau & 2\tau & 0 & -\tau & 0 \\ -\tau & -\tau & 0 & 0 & -\tau & -\tau \\ 0 & 0 & -\tau & -\tau & 0 & 0 \\ 0 & 0 & 0 & -\tau & 0 & \tau \end{bmatrix}$$

A generalization to the two limits of the fixed node approximation can be made that is similar to that suggested by Sorrella and Capriotti for GFMC. I introduce a weight parameter  $\gamma$  between 0 and 1 to calculate a weighted average effective Hamiltonian  $\hat{H}_{FN\gamma}$ .

$$\hat{H}_{FN\gamma} = \gamma \hat{H}_{FNF} + (1 - \gamma) \hat{H}_{FNC}$$

This approximation was not implemented in the example given in Chapter 4, but is included in the script printed in Appendix C.

Finally, the density matrix  $\rho_{\Delta\beta}$  for a single transition is produced from the first order Taylor expansion of the propagator for the system over imaginary time  $\Delta\beta$ .

$$\rho_{\Delta\beta} = \hat{I} - \hat{H}_{FN} \Delta\beta = \mathbf{I} - \Delta\beta \begin{bmatrix} (1-\gamma)\tau & 0 & -\gamma\tau & -\tau & 0 & 0 \\ 0 & 0 & -\tau & -\tau & 0 & 0 \\ -\gamma\tau & -\tau & 2(1-\gamma)\tau & 0 & -\tau & -\gamma\tau \\ -\tau & -\tau & 0 & 0 & -\tau & -\tau \\ 0 & 0 & -\tau & -\tau & 0 & 0 \\ 0 & 0 & -\gamma\tau & -\tau & 0 & (1-\gamma)\tau \end{bmatrix}$$

From this matrix, the elements are used as edge weights in a graph from which the paths for the system are chosen.

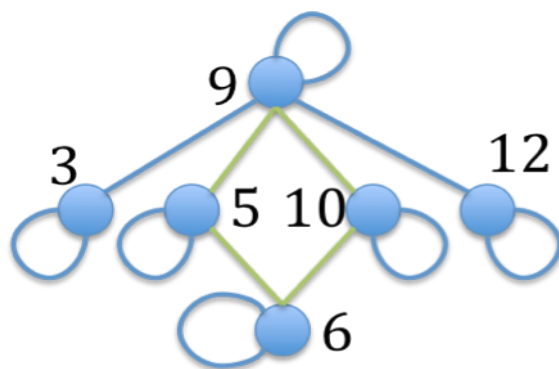


Figure 36: Graph of the FNC density matrix for a 2-electron system on a 4-site ring with a path of 4 steps shown in green.

### Initiating and Choosing a New Path

I define a path as a cycle of  $M$  steps belonging to the graph representing the density matrix of the system investigated like that in Figure 34b and Figure 35. On the graph, I produce a cycle by starting at some node of the graph and moving, via an edge, to another node, or the same node if an edge connects a node to itself and then repeating for  $M$  steps with the requirement that the last node in the sequence is the same as the first. In the case of the graph shown in Figure 36 representing the density matrix for the example system, a path of 4 steps is shown in green connecting one of the nodes to its self through 3 intermediate nodes.

In the algorithm, a path is a vector of elements that I call beads that identify the state or node of the graph that is occupied along the path. To initiate the path for the algorithm, a valid path must be selected from the graph. By far the simplest path with which to initiate the system is one which never leaves the first node in the path. In terms of the Monte Carlo algorithm and the resulting averages, this is a particularly bad choice as these paths at low temperatures are improbable and will be over-weighted in the resulting average. As a result, it is advantageous to allow the algorithm to ‘warm up’ first

by choosing new paths randomly for a period of time before beginning the averaging. The final path chosen is then the path with which the algorithm is initiated.

To choose a new path it is necessary produce a random path generator (RPG) that selects paths according to the path sum. The RPG takes an initial path as a seed and then outputs a new path randomly generated, just as a random number generator does. The rules for the RPG can be devised to exactly reproduce the probability distribution of all paths dictated by the path sum. These rules are as follows and illustrated in Figure 37:

1. Find a single bead, called the moving bead, in the given path. The state assigned to this bead will be changed and will offer a new path.
2. Identify the states assigned to the beads one step ahead (to-state) and one step behind (from-state) the moving bead. Call these the reference states.
3. Find the set of states, the mid-states, which may be reached from both the reference states in a single step.
4. Assign to each of the mid-states a weight equal to the product of the edge weights between the mid-state and the reference states.
5. Select randomly according to the weights a mid-state from the set and assign it to the moving bead. This along with the other beads in the path is your new path.

Applying this method one bead at a time for a path consisting of many beads will cause the algorithm to move very slowly through the space of possible paths. As a result, it is more advantageous to move multiple beads in the path at the same time, this both increases the speed at which the algorithm moves through the path space and reduces the correlation between paths. To do this I fix every other bead in the path and loop through the remaining beads with the algorithm detailed above, randomly choosing to fix the even or odd beads within path each time the RPG is called.

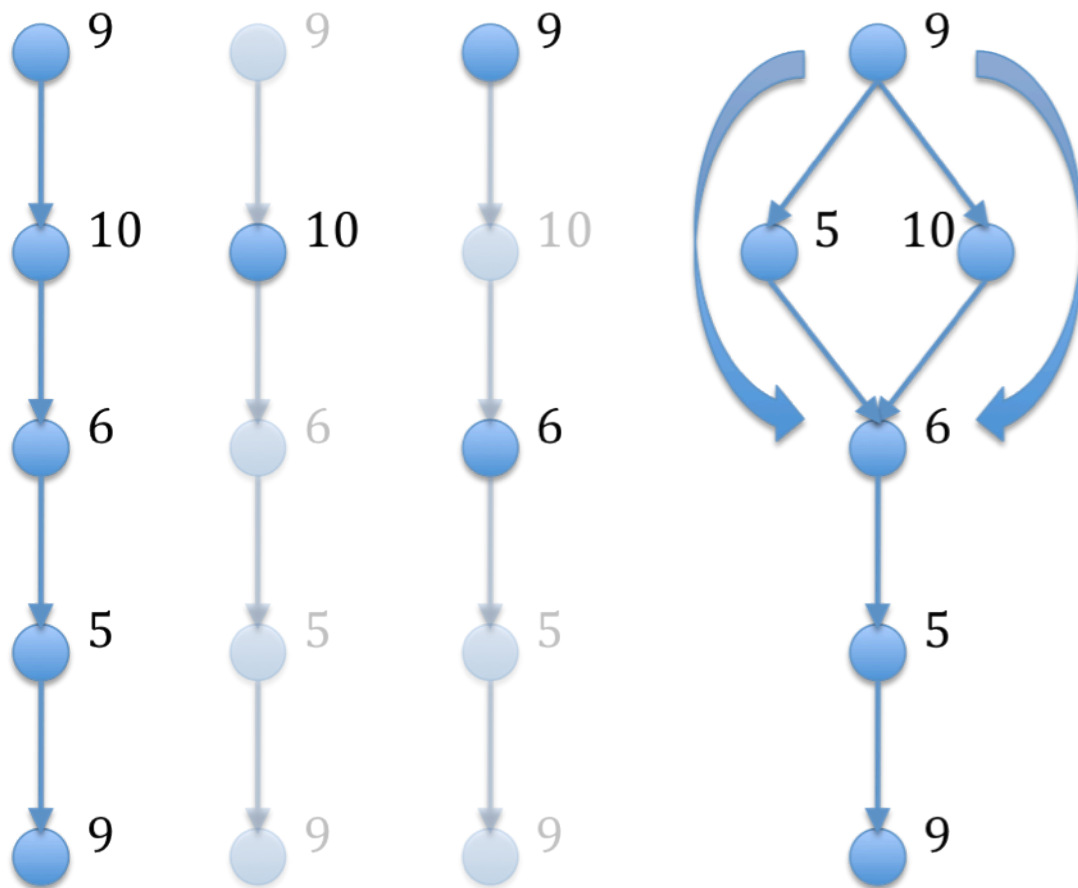


Figure 37: The RPG rules for selecting a new path. From left to right: The input for the RPG is a path. Select a bead that will be the moving bead. Identify the reference beads. Find the mid-states and assign weights, here illustrated by the thickness of the large arrows, with which to randomly choose the new path.

## Measure Observable

The ability to select paths from a Path Sum is only important if something can be measured from the distribution of paths. So, there must be some mechanism to take an observable quantity, like energy, and apply it to the system. In this section, I will discuss how to construct an observable in the framework of the Path Sum using the average energy as an example. This analysis can be extended to many other observables. Following the analysis in Chapter 4, the average energy observable is written as a weighted average of the paths in the system.

$$\langle \hat{H}_{FN\gamma} \rangle = \sum_{\{\alpha_i\}} \frac{\sum_{\alpha'} \langle \alpha_0 | \hat{H}_{FN\gamma} | \alpha' \rangle \langle \alpha' | \rho_{\Delta\beta} | \alpha_{M-1} \rangle}{\langle \alpha_0 | \rho_{\Delta\beta} | \alpha_{M-1} \rangle} P(\{\alpha_i\}, M)_\beta$$

P represents the probability associated with the path  $\{\alpha_i\}$  generated by the RPG. The ratio in front of the probability is the energy weight associated with the path that is calculated from the observable in the algorithm. To obtain this weight, like the RPG, a set of steps are followed that are listed below and illustrated in Figure 38.

1. For the given path identify the states associated with two consecutive beads; these are the reference states  $\alpha_{M-1}$  and  $\alpha_0$ .
2. The edge weight in the density matrix graph between the reference states is the normalization weight Pnorm.
3. Identify the states that may be reached from  $\alpha_{M-1}$  in a single step in the density matrix graph and from  $\alpha_0$  in a single step in the graph associated with the observable. These are the midstates  $\alpha'$ .
4. Sum over the product of edge weights between the reference states and the midstates in the two respective graphs. Normalize this value by Pnorm. This value is the observable weight.

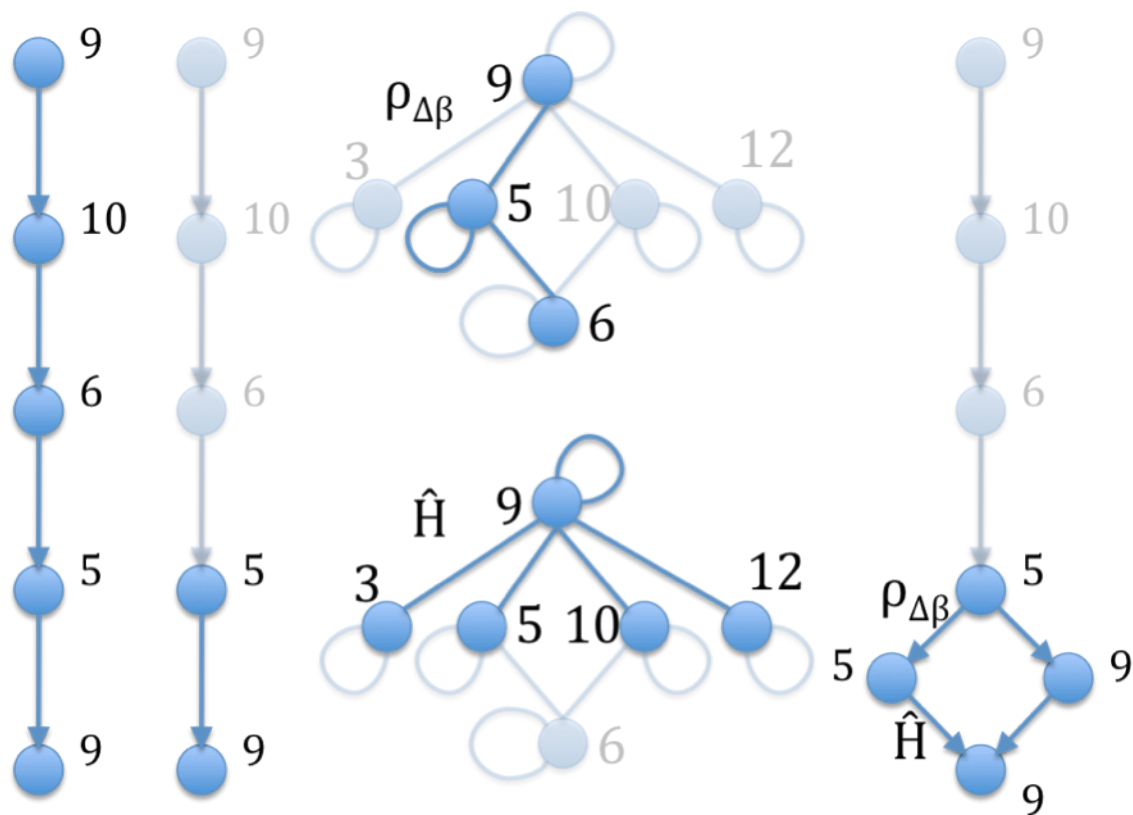


Figure 38: Steps for constructing observable weight from given path. From left to right, given the Path identify two consecutive states. For the two reference states identify the states which can be reached from the two reference states in a single step for the two graphs. Then sum over the two weights and normalize by  $P^{\text{norm}}$ .

As the path is a cycle in the graph, the path can contribute as many observable weights as there are beads in the path. This adds to the efficiency of the algorithm and is a big advantage when using the ring polymers in Path Integral analysis. To implement this, I simply loop through the groups of two consecutive beads in the path.

## APPENDIX B: SAMPLE PATH SUM MONTE CARLO MATLAB SCRIPT I

The following MATLAB script is an example of the Path Sum Monte Carlo method described in Chapter 4 and Appendix B. The algorithm is applied to a 4 atomic site ring with 2 spin states per spin and Hubbard interaction to measure the average energy for a specific temperature. There are 2 electrons in the up and down spin states. A generalized fixed node method is used that is similar to that used in the lattice Green Function Monte Carlo method with the major difference being that one extreme gives a maximum and the other a minimum to the ground state energy. All energies are measured in units of Hartrees ( $1 \text{ Hartree} = 2 * \text{Rydberg} = 27.2114 \text{ eV}$ ) and the temperature in inverse Hartrees.

This script provides understanding of 3 things:

1. How paths are chosen
2. How the effective Hamiltonian is constructed
3. How observables are calculated from a sample path

```
% Title: Square2ePSMC.m
```

```
% Author: John K. David
```

```
% July 21, 2011
```

```
% In this script I solve for the average energy for an explicitly  
% defined density matrix from a 2-body hamiltonian for a 4 site square  
% model with spin up and down sites and a Hubbard interaction
```

```
% /      2      3  
% /      O-----O  
% /      |      |  
% /      |      |  
% /      |      |  
% /      O-----O  
% /      0      1
```

```
%
```

```
% The above graph expands to the following many particle graph
```

```
%      ----- (0,3) -----  
%      /      /      \      \  
%      (0,1) (0,2) (1,3) (2,3)  
%      \*      \      /      */  
%      ----- (1,2) -----
```

```
%
```

```
% The stars represent the  $\langle a|H|b \rangle > 0$ 
```

```
% Where  $|\langle a|H|b \rangle| = t$  (single electron nearest neighbor hopping)
```

```
t = 0.01; %approximately 2.7 eV
```

```
g = 1; % gamma coefficient for generalized fixed node method.
```

```
% The 2-body Hamiltonian then looks like this:
```

```
H2b = [0 0 t -t 0 0  
       0 0 -t -t 0 0  
       t -t 0 0 -t t  
       -t -t 0 0 -t -t  
       0 0 -t -t 0 0  
       0 0 t -t 0 0];
```

```

Hs2b = [H2b,zeros(6),t*eye(6),-t*eye(6),zeros(6),zeros(6)
        zeros(6),H2b,-t*eye(6),-t*eye(6),zeros(6),zeros(6)
        t*eye(6),-t*eye(6),H2b,zeros(6),-t*eye(6),t*eye(6)
        -t*eye(6),-t*eye(6),zeros(6),H2b,-t*eye(6),-t*eye(6)
        zeros(6),zeros(6),-t*eye(6),-t*eye(6),H2b,zeros(6)
        zeros(6),zeros(6),t*eye(6),-t*eye(6),zeros(6),H2b];

% using the generalized fixed node (gamma = 0 produces the ceiling
% and gamma = 1 produces the floor) method similar in definition to
% Sandro Sorella and Luca Capriotti, Phys. Rev. B, 61 2599 (2000)
% we build the effective Hamiltonian

effHs2b = Hs2b;

for(jj=1:36)
    S = effHs2b(jj,jj);
    for(ii=1:36)
        if(effHs2b(ii,jj)>0.0)
            S = S+(1-g)*effHs2b(ii,jj);
            effHs2b(ii,jj)=-g*effHs2b(ii,jj);
        end
    end
    effHs2b(jj,jj)=S;
end

% Hubbard interaction
U = ones(6);
U = U + eye(6) - flipud(eye(6));
U = diag(reshape(U*t,[36,1]));

% then using the trotter expansion with an imaginary time B sliced Nslice
% times:

B = 1000; %approximately 300K

Nslice = 1000;

dB = B/Nslice; % about 300000K

% The effective density matrix or propagator of the system

```

```

Geff = diag(exp(-dB*diag(effHs2b+U))) - dB*effHs2b + dB*diag(diag(effHs2b));

% The path of Nslice beads

path = ones(Nslice,1)*randi(36);

% Having initiated the path we now iterate N times a path chooser constructed of
Nslice/2 single bead % moves

N = 1000000;

Eavg = 0;

Ndiag = 0;

for iter = 1:N
    bstart = randi(2);
    Etemp = 0;
    for beadmove = bstart:2:Nslice % loop through every other bead in the path
        tostate = path(mod((beadmove+Nslice),Nslice)+ 1); % future bead
        fromstate = path(mod((beadmove+Nslice-2),Nslice) + 1); % past bead

% probability vector for choosing the state for the present moving bead
        prob = (Geff(tostate,:)).*Geff(:,fromstate)/(Geff(tostate,:)*Geff(:,fromstate));
        tProb = 1;

        midstate = 1;

        pmove = prob(midstate)/tProb; % probability for choosing midstate for present
bead

        while(pmove<rand) % try the state
            tProb = tProb-prob(midstate) % if it does not work update normalized
probability
            midstate = midstate+1; % move to next state
            pmove = prob(midstate)/tProb; % updated probability for choosing midstate
        end

        path(beadmove) = midstate; % set state to the midstate
    end
end

```

```
Etemp = Etemp + effHs2b(tostate,:)*Geff(:,midstate)/Geff(tostate,midstate) +  
effHs2b(midstate,:)*Geff(:,fromstate)/Geff(midstate,fromstate); % update observable
```

```
end
```

```
Eavg = Eavg + Etemp/Nslice; % normalize by number of slices  
end
```

```
Eavg = Eavg/N; % normalize by number of iterations.
```

## APPENDIX C: SAMPLE PATH SUM MONTE CARLO MATLAB SCRIPT II

The following MATLAB script calculates the average energy for the two ring system described in Chapter 4 for a user defined number of electrons, Temperature, interlayer spacing, and Fixed Node Approximation parameter.

```
% Author: John K. David  
% July 28, 2011
```

```
clear all;
```

```
Nsites = 12; %number of sites
```

```
Nelec = 6; % number of electrons (half filled)
```

```
Del = .0; % bias between layers
```

```
epsr=3.9;
```

```
N = 2000000; % number of iterations
```

```
% temperature of simulation in inverse Hartrees 1000
```

```
% (1/Hartree) = approximately 300K
```

```
B = 75;
```

```
Nslice = 500;
```

```
t = -0.1; %hopping potential
```

```
tz = -0.001; % bare tunneling hopping
```

```
u = Del*[1,1,1,1,1,1,-1,-1,-1,-1,-1,-1]; % on site energy
```

```
ab = 1.42/0.529177; % inter atomic spacing numerator in Angstroms
```

```
al = 2.46/0.529177; % inter unit cell length numerator in Angstroms
```

```
d = .1; % spacing between layers in bohr radius = 0.529177 Angstroms
```

```
interactions = 1; % interactions? 1 = on 0 = off;
```

```
gamma = 1; % Fixed Node parameter 1 = FNF 0 = FNC;
```

```
% Coulomb interactions
```

```
% intralayer Coulomb interactions
```

```

C1 = [0,1/ab,1/ab,1/al,1/al,1/2/ab
      1/ab,0,1/al,1/ab,1/2/ab,1/al
      1/ab,1/al,0,1/2/ab,1/ab,1/al
      1/al,1/ab,1/2/ab,0,1/al,1/ab
      1/al,1/2/ab,1/ab,1/al,0,1/ab
      1/2/ab,1/al,1/al,1/ab,1/ab,0];

```

```

% interlayer Coulomb interactions

```

```

C2 = [1/d,1/sqrt(d*d+ab*ab),1/sqrt(d*d+ab*ab), ...
      1/sqrt(d*d+al*al),1/sqrt(d*d+al*al),1/sqrt(d*d+4*ab*ab)
      1/sqrt(d*d+ab*ab),1/d,1/sqrt(d*d+al*al), ...
      1/sqrt(d*d+ab*ab),1/sqrt(d*d+4*ab*ab),1/sqrt(d*d+al*al)
      1/sqrt(d*d+ab*ab),1/sqrt(d*d+al*al),1/d, ...
      1/sqrt(d*d+4*ab*ab),1/sqrt(d*d+ab*ab),1/sqrt(d*d+al*al)
      1/sqrt(d*d+al*al),1/sqrt(d*d+ab*ab),1/sqrt(d*d+4*ab*ab), ...
      1/d,1/sqrt(d*d+al*al),1/sqrt(d*d+ab*ab)
      1/sqrt(d*d+al*al),1/sqrt(d*d+4*ab*ab),1/sqrt(d*d+ab*ab), ...
      1/sqrt(d*d+al*al),1/d,1/sqrt(d*d+ab*ab)
      1/sqrt(d*d+4*ab*ab),1/sqrt(d*d+al*al),1/sqrt(d*d+al*al), ...
      1/sqrt(d*d+ab*ab),1/sqrt(d*d+ab*ab),1/d];

```

```

C = interactions*0.5*[1*C1,1*C2;1*C2,1*C1]/epsr;

```

```

%% Building the Hamiltonians %%

```

```

nSNm1 = nchoosek(Nsites,Nelec-1);
nSN = nchoosek(Nsites,Nelec);

```

```

% single particle hamiltonian

```

```

nn = zeros(6);
nn(1,2:3) = 1;
nn(2,4) = 1;
nn(3,5) = 1;
nn(4:5,6) = 1;
nn = nn+nn';

```

```

nn = [nn,zeros(6);zeros(6),nn];
nnz = [zeros(6),eye(6);eye(6),zeros(6)];

```

```

H = t*nn + tz*nnz;

```

```

% Build fock states

```

```

SNm1 = false(nSNm1,Nsites);

```

```

iSNm1 = zeros(nSNm1,1);
SN = false(nSN,Nsites);
iSN = zeros(nSN,1);

disp('initiating states...')
pause(.1);

llm1 = 0;
ll = 0;

for ii=0:2^12;
    bin = dec2bin(ii,12);
    bar = str2num(bin(:))';
    Ntrue = sum(bar);
    if(Ntrue==Nelec-1)
        llm1 = llm1+1;
        SNm1(llm1,:) = bar>0;
        iSNm1(llm1) = ii;
    elseif(Ntrue==Nelec)
        ll = ll+1;
        SN(ll,:) = bar>0;
        iSN(ll) = ii;
    end
end

SN = fliplr(SN);
SNm1 = fliplr(SNm1);

%build the exact Hamiltonian

disp('building Hamiltonians...')

for ii=1:Nsites
    adt = zeros(nSN,nSNm1);
    ff = find(~SNm1(:,ii));
    for kk=1:length(ff)
        jj = ff(kk);
        mm = iSNm1(jj) + 2^(ii-1);
        ll = find(iSN==mm);
        A = SNm1(jj,:);
        adt(ll,jj) = (-1)^sum(A(1:(ii-1)));
    end
    adhN{ii} = adt;
end

```

```

    ahN{ii} = adt';
end

U = diag(SN*C*SN');

clear iSNm1;
clear iSN;
clear SN;
clear SNm1;
clear adt;

HN = zeros(nSN,nSN);
for ii=1:Nsites
    for jj=1:Nsites
        HN = HN + H(ii,jj)*adhN{ii}*ahN{jj};
    end
end

clear adhN;
clear ahN;

% build Fixed Node Hamiltonians

HNFNd = diag(HN);
HNFNF = HN - diag(HNFNd);
HNFNF = -abs(HNFNF);
HNFNF = HNFNF+diag(HNFNd);

HNFNd = diag(HN);
HNFNC = HN - diag(HNFNd);
HNFNd = HNFNd + sum(HNFNC.*(HNFNC>0))';
HNFNC(HNFNC>0) = 0;
HNFNC = HNFNC+diag(HNFNd);

HNFN = HNFNC*(1-gamma) + HNFNF*gamma;

dB = B/Nslice; % imaginary time increment

% The effective density matrix or propagator of the system
Geff = diag(exp(-dB*(diag(HNFN)+U))) - dB*HNFN + dB*diag(diag(HNFN));

% The path of Nslice bead

```

```

path = ones(Nslice,1)*randi(nSN);

disp('warming up the Monte Carlo')

for iter = 1:10000
    bstart = randi(2);
    Etemp = 0;
    % loop through every other bead in the path
    for beadmove = bstart:2:Nslice
        tostate = path(mod((beadmove+Nslice),Nslice) + 1); % future bead
        fromstate = path(mod((beadmove+Nslice-2),Nslice) + 1); % past bead

        % probability vector for choosing the state for the present moving bead
        prob = (Geff(tostate,:)).*Geff(:,fromstate)/(Geff(tostate,:)*Geff(:,fromstate));

        tProb = 1;
        ff = find(prob);
        midstate = 1;
        pmove = prob(ff(midstate))/tProb;
        while(pmove<rand) % try the state
            tProb = tProb-prob(ff(midstate));
            midstate = midstate+1; % move to next state
            pmove = prob(ff(midstate))/tProb; % updated probability for choosing midstate
        end

        path(beadmove) = ff(midstate); % set state to the midstate
    end
end

% Having initiated the path we now iterate N times a path chooser constructed of
% Nslice/2 single bead moves

disp('Now doing the Calculations')

HNFN = HNFN+diag(U);

Eavg = 0;
Ndiag = 0;
for iter = 1:N
    bstart = randi(2);
    Etemp = 0;
    for beadmove = bstart:2:Nslice % loop through every other bead in the path

```

```

tostate = path(mod((beadmove+Nslice),Nslice) + 1); % future bead
fromstate = path(mod((beadmove+Nslice-2),Nslice) + 1); % past bead

% probability vector for choosing the state for the present moving bead
prob = (Geff(tostate,:)).*Geff(:,fromstate)/(Geff(tostate,:)*Geff(:,fromstate));
tProb = 1;
ff = find(prob);
midstate = 1;
pmove = prob(ff(midstate))/tProb;

while(pmove<rand) % try the state
    tProb = tProb-prob(ff(midstate));
    midstate = midstate+1; % move to next state
    pmove = prob(ff(midstate))/tProb; % updated probability for choosing midstate
end

path(beadmove) = ff(midstate); % set state to the midstate

% update observable
Etemp = Etemp + HNFN(tostate,:)*Geff(:,ff(midstate))/Geff(tostate,ff(midstate))...
    + HNFN(ff(midstate,:)*Geff(:,fromstate)/Geff(ff(midstate),fromstate);
end
Eavg = Eavg + Etemp/Nslice; % normalize by number of slices
end

Eavg = Eavg/N; % normalize by number of iterations.

```

## References

- [1] Anisur Rahman et. al., “Novel channel materials for ballistic nanoscale MOSFETs-bandstructure effects”, *IEDM Tech. Digest 2005* pp. 601-604
- [2] Kurtis D. Cantley et. al., “Performance Analysis of III-V Materials in a Double-Gate nano-MOSFET”, *IEDM 2007* pp. 113-116
- [3] Ningyu Shi et. al., “On Strain and scattering in deeply-scaled n-channel MOSFETs: A quantum-corrected semiclassical Monte Carlo analysis”, *IEDM 2008* p. 1-4
- [4] S. Datta et. al., “85nm Gate Length Enhancement and Depletion mode InSb Quantum Well Transistors for Ultra High Speed and Very Low Power Digital Logic Applications” *IEDM, 2005*, pp. 763-766
- [5] [www.ITRS.net](http://www.ITRS.net)
- [6] C. Jacoboni, P. Lugli, *The Monte Carlo Method for Semiconductor Device Simulation*, Wien, Austria; Springer-Verlag, 1989
- [7] Omer OZBAS et. al., “Monte Carlo Simulation of Electron Transport in InSb”, *Turk J. Phys.*, 2002 vol. 26 pp. 283-287
- [8] Massimo V. Fischetti, “Monte Carlo Simulation of Transport in Technologically Significant Semiconductors of the Diamond and Zinc-Blende Structures—Part I: Homogeneous Transport”, *IEEE Trans. Elec. Dev. Vol. 38 (3) March 1991* pp. 634-649
- [9] Ramey, S. “The Effective Potential in Simulation of SOI MOSFETs”, Doctoral Dissertation, Arizona State University, Tempe, Arizona, USA
- [10] B. Winstead, and U. Ravaioli, “A Quantum Correction Based on Schrödinger Equation Applied to Monte Carlo Device Simulation”, *IEEE Trans. on Electron Devices*, Volume 50, Issue 2, Page(s): 440 – 446, February, 2003
- [11] X. F. Fan, X. Wang, B. Winstead, L. F. Register, U. Ravaioli, and S. K. Banerjee, "MC simulation of strained-Si MOSFET with full-band structure and quantum correction," *IEEE Transactions on Electron Devices*, vol. 51, pp. 962-970, Jun 2004.
- [12] K. S. Novoselov, A. K. Geim, S. V. Morozov, D. Jiang, Y. Zhang, S. V. Dubonos, I. V. Grigorieva, and A. A. Firsov, “Electric field effect in atomically thin carbon films,” *Science*, vol. 306, no. 5696, pp. 666–669, Oct. 22, 2004.
- [13] K. I. Bolotin, K. J. Sikes, Z. Jiang, M. Klima, G. Fudenberg, J. Hone, P. Kim, and H. L. Stormer, “Ultrahigh electron mobility in suspended graphene,” *Solid State Commun.*, vol. 146, no. 9-10, pp. 351-355, Jun. 2008

- [14] S. K. Banerjee, L. F. Register, E. Tutuc, D. Basu, S. Kim, D. Reddy, and A. H. MacDonald, "Graphene for CMOS and beyond CMOS applications," *Proc. IEEE*, vol. 98, No. 12, pp. 2032-2046, Dec. 2010
- [15] P. Neugebauer, M. Orlita, C. Faugeras, A.-L. Barra, and M. Potemski, "How Perfect Can Graphene Be?," *Phys. Rev. Lett.*, vol. 103, 136403, 2009
- [16] J. -H. Chen, C. Jang, S. Adam, M. S. Fuhrer, E. D. Williams, and M. Ishigami, "Charged-impurity scattering in graphene," *Nature Phys.*, Vol 4., pp. 377-381
- [17] M. C. Lemme, T. J. Echtermeyer, M. Baus, and H. Kurz, "A graphene field-effect device," *IEEE Electron Device Lett.*, vol. 28, no. 4, pp. 282-284, Apr. 2007.
- [18] I. Meric, M. Y. Han, A. F. Young, B. Ozyilmaz, P. Kim, and K. L. Shepard, "Current saturation in zero-bandgap, top-gated graphene field-effect transistors," *Nature Nanotechnol.*, vol. 3, pp. 654-659, Nov. 2008.
- [19] E. H. Hwang and S. Das. Sarma, "Acoustic phonon scattering limited carrier mobility in two-dimensional extrinsic graphene," *Phys. Rev. B.*, vol .77, 115449, 2008
- [20] N. Harada, M. Ohfuti, and Y. Awano, "Performance Estimation of Graphene Field-Effect Transistors Using Semiclassical Monte Carlo Simulation," *Appl. Phys. Exp.*, 1, 024002, 2008
- [21] N. Harado, Y. Awano, S. Sato, and N. Yokoyama, "Monte Carlo simulation of electron transport in a graphene diode with a linear energy band dispersion," *J. Appl. Phys.*, **109**, 104509, 2011
- [22] A. Akturk and N. Goldsman, "Electron transport and full-band electron-phonon interactions in graphene," *J. Appl. Phys.*, **103**, 053702, 2008
- [23] K. M. Borysenko, J. T. Mullen, E. A. Barry, S. Paul, Y. G. Semenov, J. M. Zavada, M. Buongiorno Nardelli, and K. W. Kim, "First-principles analysis of electron-phonon interactions in graphene," *Phys. Rev. B.*, **81**, 121412, 2010
- [24] D. Jena, T. Fang, Q. Zhang, H. Zing, "Zener tunneling in semiconducting nanotube and graphene nanoribbon *p-n* junction," *Appl. Phys. Ltrs.* **93**, 112106, 2008
- [25] C. Jacoboni and L. Reggiani, "The Monte Carlo method for the solution of charge transport in semiconductors with applications to covalent materials," *Rev. Mod. Phys.*, vol. 55, No. 3, July 1983
- [26] M. V. Fischetti, "Monte Carlo Simulation of Transport in Technologically Significant Semiconductors of the Diamond and Zinc-Blende Structures—Part I: Homogeneous Transport," *IEEE Trans. Electron Devices.*, vol. 38, no. 3, pp. 634-649, March 1991

- [27] M. V. Fischetti and S. E. Laux, "Monte Carlo Simulation of Transport in Technologically Significant Semiconductors of the Diamond and Zinc-Blende Structures—Part II: Submicrometer MOSFET's," *IEEE Trans. Electron Devices.*, vol. 38, no. 3, pp. 650-660, March 1991
- [28] M. V. Fischetti and S. E. Laux, "Monte Carlo analysis of electron transport in small semiconductor devices including band-structure and space-charge effects," *Phys. Rev. B.*, vol. 38, no. 14, pp. 9721-9745, Nov. 1988
- [29] S. Adam, E. H. Hwang, V. M. Galitski, S. Das Sarma, "A self-consistent theory for graphene transport," *PNAS*, vol. 104, no 47, pp 18392-18397, Nov. 2007
- [30] S. Kim, J. Nah, I. Jo, D. Shahrjerdi, L. Colombo, Z. Yao, E. Tutuc, S. K. Banerjee, "Realization of a high mobility dual-gated graphene field-effect transistor with  $\text{Al}_2\text{O}_3$  dielectric," *Appl. Phys. Lett.*, **94**, 062107
- [31] Eisenstein, J. P., MacDonald, A.H.: Bose-Einstein condensation of excitons in bilayer electron systems. *Nat.* 432, 691-694 (2004)
- [32] Banerjee, S.K., Register, L.F., Tutuc, E., Reddy, D., MacDonald, A.H.: Bilayer PseudoSpin Field-Effect Transistor (BiSFET): A Proposed New Logic Device. *IEEE Electron Device Lett.* 30, 158-160 (2009)
- [33] Min, H., Bistritzer, R., Su, J-J., MacDonald, A.H.: Room-temperature superfluidity in graphene bilayers. *Phys. Rev. B* 78, 121401 (2008)
- [34] Basu, D., Register, L.F., Reddy, D., MacDonald, A.H., Banerjee, S.K.: Tight-binding study of electron-hole pair condensation in graphene bilayers: Gate control and system-parameter dependence. *Phys. Rev. B* 82, 075409 (2010)
- [35] Basu, D., Register, L.F., MacDonald, A.H., Banerjee, S.K., Effect of interlayer bare tunneling on electron-hole coherence in graphene bilayers, *Phys. Rev. B*, accepted for publication.
- [36] Feynman, R.P.: Space-Time Approach to Non-Relativistic Quantum Mechanics. *Rev. Mod. Phys.* 20, 367-387 (1948)
- [37] Ceperley, D.M., Path Integrals in the Theory of Condensed Helium, *Rev. Mod. Phys.* 67, 279-355 (1995)
- [38] The total number of configurations for a system containing  $N$  single particle states and  $Z$  fermions is equivalent to the number of combinations of  $Z$  occupied states chosen from the set of  $N$  single particle states. This is written as  ${}_N C_Z = N!/(Z!(N-Z)!)$ . For a system at half-filling, this number grows exponentially with  $N$ .
- [39] A description of the mechanism of second quantization and the Fock space can be obtained from most textbooks on condensed matter field theory. One is: Atland, A., Simons, B.: *Condensed Matter Field Theory*. Cambridge, U.K. (2006)

- [40] Casula, M., Filippi, C., Sorella, S.: Diffusion Monte Carlo Method with Lattice Regularization. *Phys. Rev. Lett.* 95, 100201 (2005)
- [41] ten Haaf, D.F.B., van Bemmelen, H.J.M., van Leeuwen, J.M.J., van Saarloos, W., Ceperley, D.M.: Proof for an upper bound in fixed-node Monte Carlo for lattice fermions. *Phys. Rev. B.* 51 13039
- [42] Ceperley, D.M., Alder, B.J., Ground State of the Electron Gas by a Stochastic Method *Phys. Rev. Lett.* 45 566 (1980)
- [43] By reordering the states it is possible that the resulting Hamiltonian in the FNC case may give a more accurate result, however, this would not be the case for the FNF as reordering of the states would only shift the rows and columns of the matrix and not change the absolute values of any of the elements.
- [44] Su, J and MacDonald, A. H., How to make a bilayer exciton condensate flow. *Nature Phys.*, 4, pp. 799-802 (2008)
- [45] David, J., Register, L.F., and Banerjee, S.K. 3D Monte Carlo study of short channel tri-gate nanowire MOSFETs, *Solid-State Electronics*, 61, pp. 7-12
- [46] David, J., Register, L.F., and Banerjee, S.K. Semi-Classical Monte Carlo analysis of Graphene FETs, submitted to *IEEE Transactions on Electron Devices*
- [47] David, J., Register, L.F., and Banerjee, S.K. A Path Sum Monte Carlo Approach for Many-Electron Systems within a Tight-Binding Basis, accepted for publication *J. Comp. Elec.*

## **Vita**

John K. David was born on Dec. 29<sup>th</sup>, 1982 in Mount Kisco, New York to his parents Robert M. and Carol A. David. After graduating from the American School of Paris in St. Cloud, France, he attended Northwestern University where he obtained his B.S. in Electrical Engineering. While at Northwestern he worked in the Center for Quantum Devices as an undergraduate research assistant under Prof. Manijeh Razeghi, where he was a co-author on 8 publications concerning the growth and measurement of Quantum Cascade Lasers and was awarded a Motorola Undergraduate Research Grant. After acquiring his B.S. he married Julianne M. Kuck and stayed at Northwestern University to obtain his Master of Science in Electrical Engineering advised jointly by Prof. Lincoln Lauhan and Prof. Houman Mohseni. After completing his M.S. in 2006, he entered The Graduate School at The University of Texas at Austin in the same year to study Electrical Engineering under the supervision of Prof. Sanjay K. Banerjee and Prof. Leonard F. Register. He is a recipient of the Microelectronics and Computer Development Fellowship and the Robert Noyce Memorial Fellowship.

Permanent email: [john.david@utexas.edu](mailto:john.david@utexas.edu)

This dissertation was typed by John K. David.